A SILICON STRIP MICROVERTEX DETECTOR FOR STUDYING QCD JETS ASSOCIATED WITH DIRECT PHOTONS

Mani, Sudhindra

B.S. Delhi University, India, 1980

M.S. University of Pittsburgh, 1982

Submitted to the Graduate Faculty of
Arts and Sciences in partial fullfillment
of the requirements for the degree of
Doctor of Philosophy

University of Pittsburgh
1986

Dedicated to the fond memory of Bhaskar Rai.

Abstract

This thesis is about the design and construction of a charged particle tracking telescope made up of silicon microstrip detectors (SMD's). The device itself is a component of the E706 spectrometer being constructed for use at Tevatron II, the new proton accelerator at Fermilab. This detector is designed to study the production of direct photons and the associated hadron physics. We will present a comprehensive discussion of this effort.

A description of the physics goals in chapter I defines the physics requirements and motivates the use of SMD's. Chapter II introduces us to the construction and instrumentation of this class of detectors. In order to have a working set of SMD's, especially in the environment of the Tevatron II, one needs a large and carefully constructed system of electronics. This is detailed in chapters III and IV. As we will see, theoretical predictions in this area of physics depend on Monte Carlo techniques which have become quite sophisticated over the years. In chapter V the adaptation of existing software to our needs is described. Finally in chapter VI, we look at the future and discuss some additional physics goals that can be pursued using the same detector.

Acknowledgments

I would like to thank Paul Shepard, my thesis adviser, for the continued support and guidance throughout my thesis project. I appreciate the personal interest he took in teaching me experimental skills. The good humor and wisdom that Gene Engels imparted to me was instrumental in clearing up my dilemmas on countless occasions. I greatly value the atmosphere of friendship and confidence that Paul and Gene created around me. They are largely responsible for my professional development.

Alpana, my wife, has been very patient and understanding with me. I have learnt a lot from her about every thing that is orthogonal to Physics. I am thankful for her companionship.

I would also like to thank Tony Duncan and Julia Thompson for the patience that they displayed in answering my questions. Tony made High Energy theory understandable to me in the most intuitive fashion. Julia was responsible for introducing me to the world of large–scale computing. I am grateful to Bill McNamee for helping me out with his sixth sense for electronics. I would like to acknowledge the efforts of Don Plants, Ron Tosh and Darryl Orris towards the construction of the detector planes. I received a helping hand from a lot of under–graduate students who worked with us at one time or another. At the risk of missing someone out, I would like to name them all -- Rick, Larry, Tim, Chris, John, Cynthia, Bert and Jaya.

I am indebted to my parents for the very cause for my existence. I hope that this brings them satisfaction.

I have received inner guidance from J. Krishnamurthy, the Grateful Dead, Jim Morrison and Lord Shiva. May peace be with them.

October 1, 1986.

TABLE OF CONTENTS

CHAPTER I.
DIRECT PHOTONS AND QCD JETS

A. A QUALITATIVE LOOK AT QCD

Quantum Chromodynamics (QCD) is by now a well established theory of sub-nucleonic Physics. Here we will present the salient features in a qualitative fashion. * QCD describes the interaction of constituent fermions, called quarks, through gauge bosons, called gluons. Quarks and gluons together form all hadrons. QCD was formulated in the early 1970's following some breakthroughs in our understanding of renormalizable local gauge theories. Quantum Electrodynamics (QED), which is the local gauge theory of electromagnetic interactions, had been around for nearly two decades at that time. The existence of quarks had been postulated in order to understand the spectrum of elementary particles and resonances which was steadily growing. The quarks were said to come in three different types, or flavors, called up, down, and strange. Different products of the representations of the flavor symmetry group $SU(3)_F$ could account for all the known hadrons[3]. A new quantum number 'color' for the quarks had been suggested in order to facilitate the anti-symmetrization of the hadron wave-functions. Nothing was known about the dynamics of the quarks though and they were even regarded by some as mathematical objects. QCD incorporates them as the basic building blocks and through gluon interactions attempts to include the dynamics required to reproduce the strong nuclear force.

The field theory of QCD is analogous to QED which describes the interaction between charged fermions and gauge photons. The analogy stops here. Unlike QED's charge quantum number, QCD's color (hence chromo-) quantum number has three degrees of freedom — these have been traditionally called red, blue, and green. The

---

* For a formal introduction to QCD see reference [1] and R. Peccei's article in reference [2].

color symmetry group $SU(3)_c$, which describes the transformations among colored quarks, has eight gluons as its generators and they carry combinations of color and anti-color of different kinds. For example, a red quark transforms into a green quark by emitting a gluon which carries red and anti-green colors. Since the gluons themselves carry net color, they can emit and absorb other gluons. This is in contrast to QED where the photon is uncharged and does not couple directly with other photons. The inclusion of three degrees of freedom was successfully formulated in the form of a non-Abelian gauge theory, unlike QED which is Abelian. A major break through in this regard was the proof for the renormalizibility of a non-Abelian gauge theory. The three vertices allowed in QCD are shown in Figure I-1. The factors that enter at each vertex depend on the structure constants of SU(3).

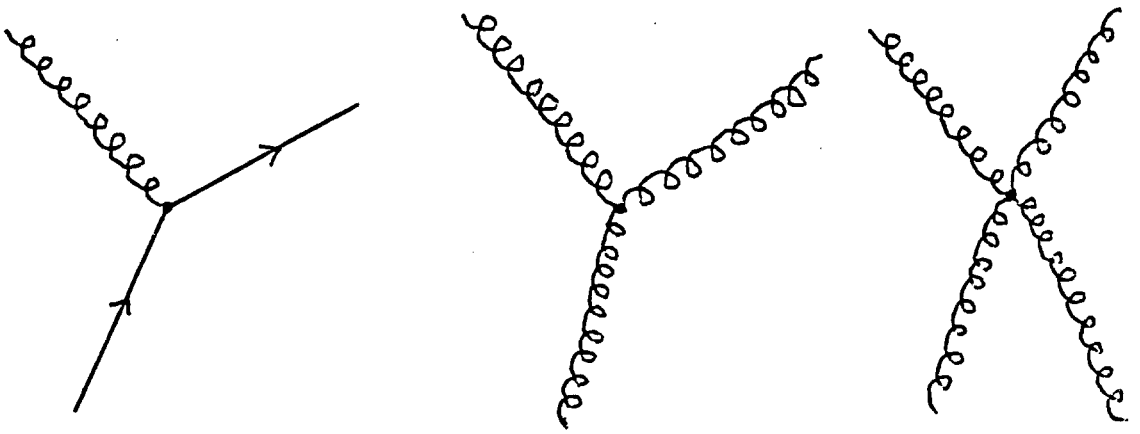

Figure I-1:

Another major difference between QED and QCD lies in the fact that stable charged particles and photons are observable at all length scales and hence lend themselves to the measurement of their charge, mass, etc. Quarks and gluons, on the other hand, remain confined within hadrons. The discovery of the idea of asymptotic freedom[4,5] — that the strength of the coupling decreases with increasing momentum transfers (Q^2) — was a necessary ingredient in the success of QCD. This idea can be understood if we picture a quark attempting to escape from, say, a proton. With increasing distance it will be able to exchange gluons with decreasing virtual masses

according to the uncertainty principle. The smaller the momentum transfer the larger the coupling strength gets and hence the quark stays confined within the proton. Another important advantage of this behavior of the coupling strength is that at sufficiently high Q^2 the dimesionless coupling α_s gets smaller than unity and hence QCD graphs can be treated perturbatively. This allows for calculation of some quantities that can be measured in the high energy regime of present-day accelerators. This is discussed in more detail in section I.B.

Three major observations provide one with overwhelming evidence for the existence of quarks. First, a look at the spectrum of known mesons shows certain patterns in their quantum numbers, namely mass, charge, spin, and parity, and these can be predicted by constructing mesons out of a pair of quark and anti-quark. The quark and anti-quark can have the same or different flavors but they always carry opposite colors. A similar pattern is seen among baryons which are constructed out of three quarks carrying different colors. In either method of construction the resulting hadron is a color singlet. The list of experimentally accessible flavors has gone up to five with the inclusion of charm and bottom and larger flavor symmetry groups and their representations are required for making up the known spectrum. See reference[6] for an example of constructing multiplets of mesons and baryons. An overall pattern has emerged that groups quarks and leptons into 'families' or 'generations'. There is evidence for a total of three families. Another quark, called top, is required to complete the third family. Experimental evidence in hadron spectroscopy is still pouring in and adding to the firm belief in the existence of quarks.

Second, the class of experiments called deep-inelastic scattering, in which a lepton undergoes a high energy scattering with a nucleon, shows evidence for the presence of pointlike objects within the nucleon[7, 8]. This certainly rules out the possibility that the quarks and their flavor quantum numbers are an abstract mathematical idea. Last, the more recent observations of jets (roughly, a collection of hadrons within a cone) in collisions of high energy hadrons are a confirmation of the prediction that quarks and gluons coming out of such scatterings will fragment into jets. In other words, existence of jets can be explained only by recognizing quarks as their source. Jets were first seen in electron-positron collisions and were identified as quark jets. These were events in

which two jets appeared in directions opposite to each other. This gave evidence for the existence of quarks but none for QCD. Later some events were seen to have three jets and the third jet was interpreted as coming from a gluon that was radiated by a quark. This provided the first evidence for the existence of gluons. The exotic glueball, a bound state of only gluons, still eludes experimenters and theorists alike.

The evidence for existence of color is more indirect in that it is inferred from measurements of cross-sections and decay rates that can be calculated with and without counting the colors. Below we will cite the two most famous examples. Experiments have measured the production cross-section, by a virtual photon in e^+-e^- collisions, of hadrons normalized to $\mu^+-\mu^-$ production. A meson being a quark and anti-quark pair can be made in three different color combinations while the muons are colorless. This relative cross-section when calculated from QED only involves a summation over the charge-squared of the accessible quark flavors. The answer disagrees from the experimental results by a factor of approximately 3. This difference can be accounted for by the existence of three colors which should have been included in the summation. Another example is the calculated decay rate of $\pi^0 \longrightarrow 2\gamma$. The QED calculation involves a summation over all possible quark loops. Not counting the three color possibilities again leads to an error by a factor of roughly 3 from the measured value. * Although this qualitative picture gives us confidence in the foundations of QCD, the tests for the dynamics are much more complicated as we will see in the next section.

B. PARTON MODEL AND JETS

Perturbative QCD allows one to calculate differential cross-sections for the scattering of partons (a collective name for quarks and gluons). Experiments, on the other hand, can be done only by scattering hadrons. In order to calculate cross-sections for hadron scattering, the QCD cross-sections have to be convoluted with probability functions for the occurrence of the initial state partons and final state hadrons. Figure I-2 shows an example of how the hadron scattering is pictured in the

---

* For a detailed discussion of evidence for color see reference [9].

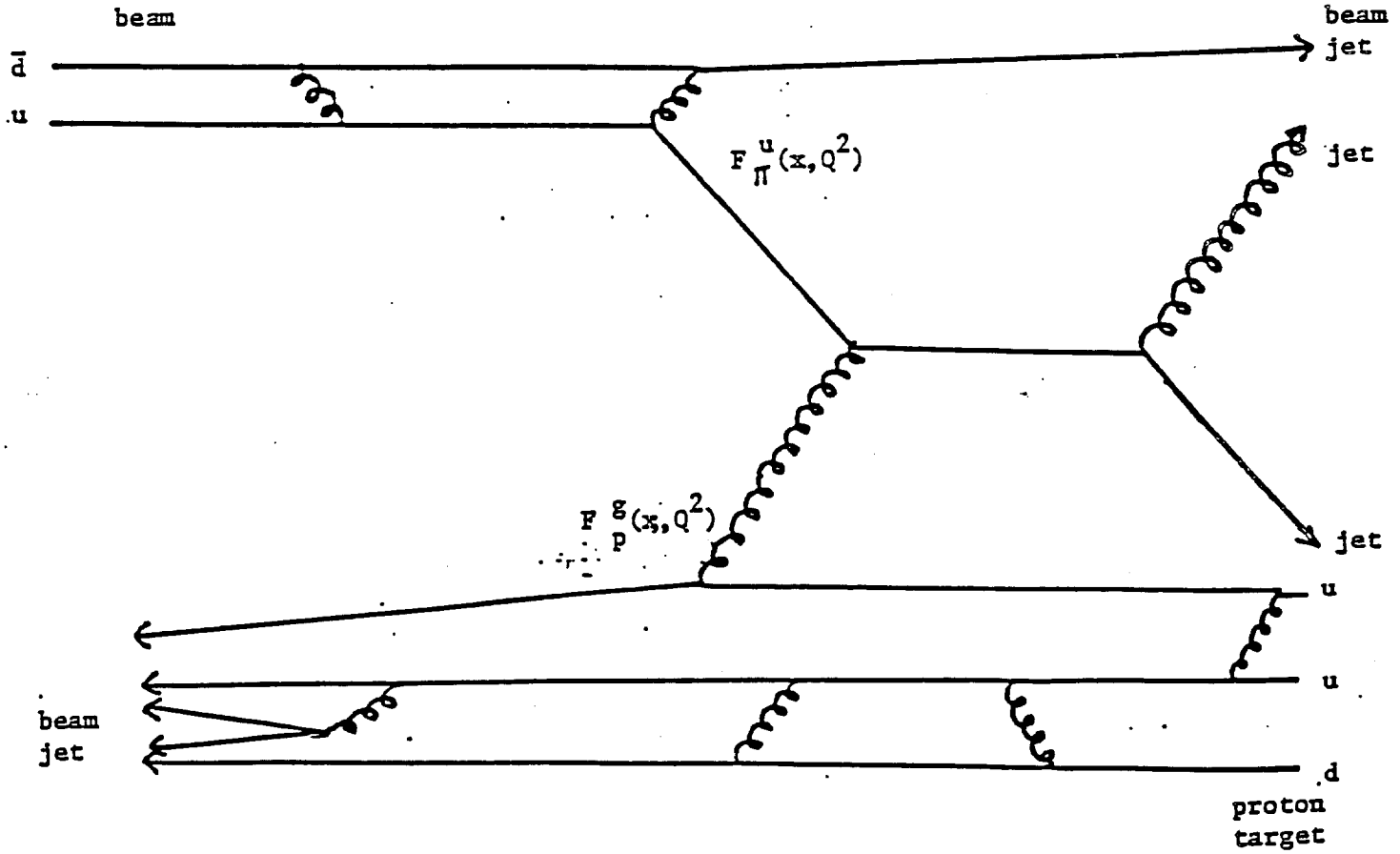

$$E_{jet}\frac{d\sigma}{d^3P_{jet}}(\pi^+p \to jet+\ldots) = \int \frac{dx_1}{x_1}\frac{dx_2}{x_2} F_{\pi}^{u}(x_1,Q^2) F_{p}^{g}(x_2,Q^2) E_{jet}\frac{d\hat{\sigma}}{d^3P_{jet}}$$

+ other possible diagrams

Figure I-2: An example of the parton model showing the inelastic scattering of a pion off a proton target resulting in two jets. The cross-section is computed using the QCD cross-section for the hard scattering of the partons and the structure functions in the initial state. To obtain the inclusive cross-section all possible QCD diagrams and the required structure functions have to be considered.

parton model. The particular process is the scattering of a pion beam particle from a proton target such that two jets are seen in the final state.One QCD subprocess that can give this final state is a quark scattering off a gluon. The cross-section given in the figure can be broken down into distinct pieces. The functions that estimate the probability of finding a particular parton within a particular hadron such that the parton carries with it a fraction x of the momentum of the hadron are called structure functions. Hence, the integrand has the QCD cross-section for the parton level process multiplied by the structure functions of interest $F^{g}_{p}(x,Q^2)$ and $F^{u}_{\pi}(x,Q^2)$. The structure functions for the valence (up and down) quarks in the nucleons have been measured extensively in deep-inelastic scattering experiments. The results show scaling violation, that is the structure functions depend on Q^2, which is due to the contribution from quark and anti-quark pairs appearing out of the vacuum. This also leads to measurements of anti-quark structure functions. The gluon structure functions for the pion are not very well known, although some experiments[10] have measured them for the nucleons.

The process chosen in Figure I-2 can be made more specific if we demand, for example, that one of the jets in the final state contain, say, a K^+ meson. The functions which describe the probability of a particular parton emerging as particular hadrons are called fragmentation functions. Figure I-3 shows a model for understanding this phenomenon and the cross-section for the specific process of our example. All such modes for the fragmentation to proceed have to be considered in order to get a number analogous to a branching ratio ($g->K^+$+....). These are essentially not calculable since the fragmentation involves soft (low Q^2) QCD processes. Some forms for these functions have been suggested that are partially successful in describing some of the features of jets seen in e^+-e^- collisions[11, 12]. The models keep improving with experimental feed-back but they are far from arriving at analytical understanding. There are suggestions that due to the presence of the color field of the spectator quarks the fragmentation functions in hadronic collisions have to be quite different. We will return to this question in chapter VI when we discuss the fragmentation of gluons into heavy quark pairs. As mentioned earlier, the detailed knowledge of fragmentation functions is not essential for calculating inclusive cross-sections. Hence, to the lowest order a measurement of two-jet differential cross-section for hadronic

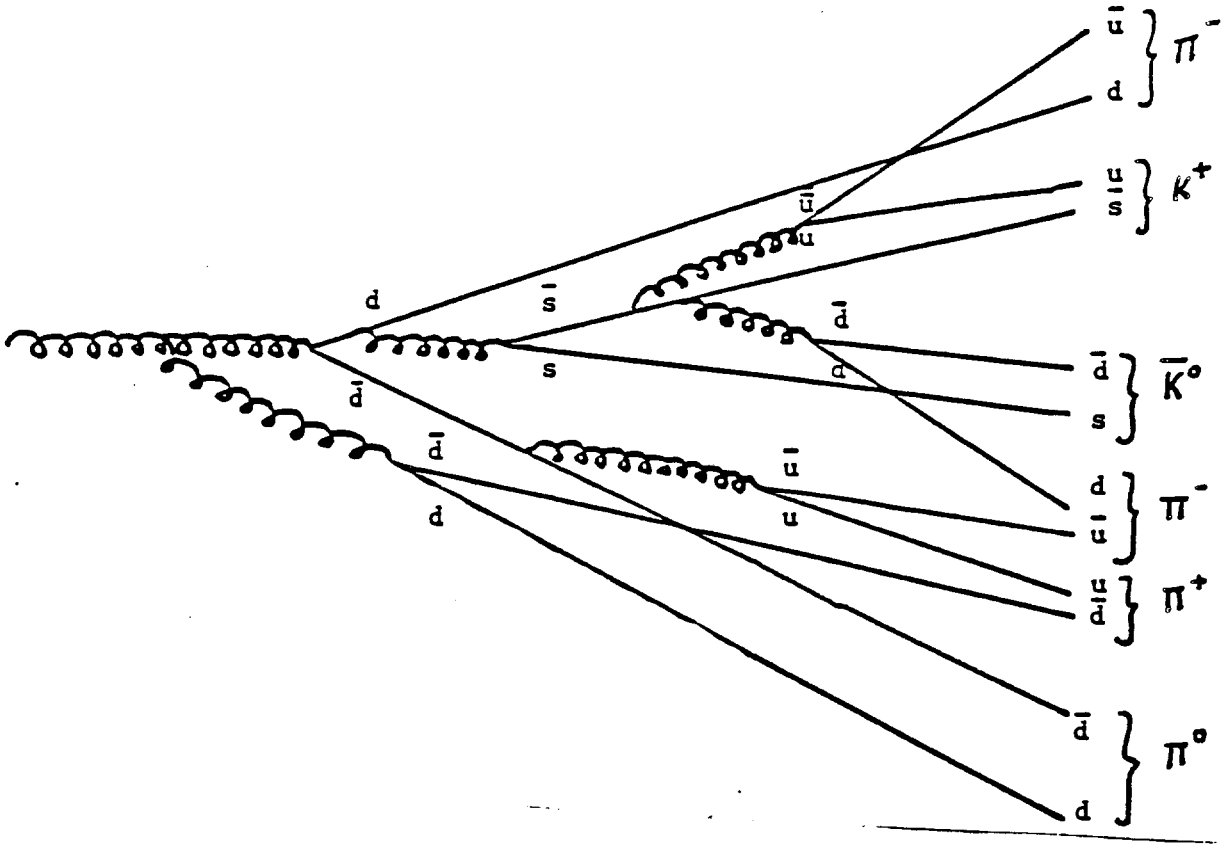

Figure I-3: A schematic representation of gluon fragmentation. All the intermediate gluons can have very low Q^2 thus making this process incalculable in perturbation theory.

collisions is an obvious test of QCD. Direct photons, as will be suggested below, provide a simpler and rather unique test of QCD.

C. DIRECT PHOTONS

Due to the fact that quarks can couple to both photons and gluons, for any QCD diagram that has a final state gluon coming from a virtual quark a similar diagram can be drawn in which the gluon is replaced by a photon. These are the prompt, or direct, photons.* This is shown in Figure I-4 for the only two possible second order QCD diagrams. They are called Compton and annihilation diagrams after the similar diagrams in electron-photon scattering. In either mode of production the final state contains a jet on the away-side. Unlike the gluon, the final state photon can be

---

*For a review of Direct Photon Physics, see reference [12].

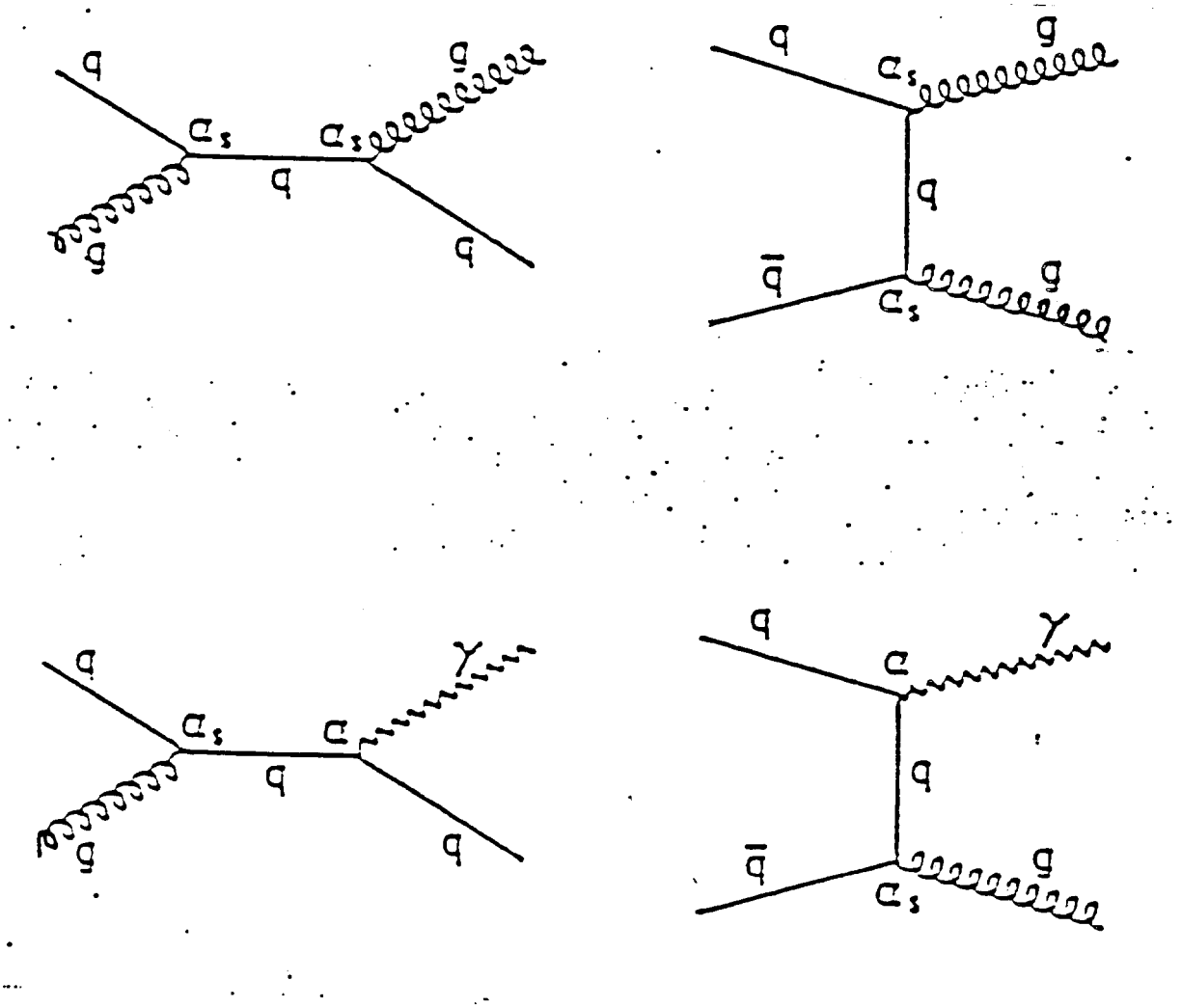

Figure I-4: Second order QCD diagrams and their analogues with a direct photon in the final state. These are of order $\alpha_{em}\,\alpha_s$.

measured directly and with it one gains access to information about the hard scattering of the constituents. Moreover, the final state in the direct photon process as compared to the two-jet process is relatively simpler to deal with experimentally. The cross-sections for this process are reduced by a factor α/α_s as compared to the two-jet process but the overall cross-section is reduced by a larger factor because there are many more QCD diagrams that contribute to the two-jet cross-section. Diagrams of order $\alpha_{em}\alpha_s^2$ can also contribute to direct photon production. Figure I-5 shows one such process. These are called quark bremstrahlung diagrams in analogy with QED. Again, since there are many more such diagrams their overall contribution to direct photon production can be substantial. They will be characterized by having a jet on the same side as well as a jet on the away-side. A calculation of all the graphs of second order has been done by Aurenche et al[13].

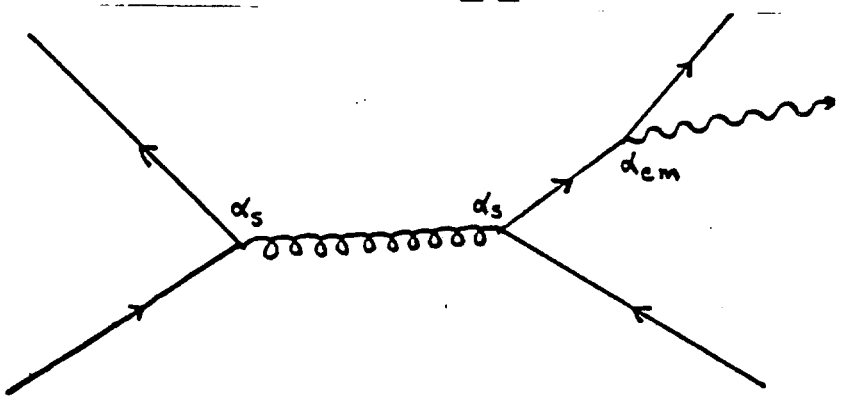

Figure I-5: Quark bremstrahlung resulting in direct photon production.

Another factor that provides merit for the direct photon process is an ability to infer the QCD diagram which resulted in its production. This can be achieved by measuring the direct photon yields from different hadronic beams. For example, a comparison of the yields from π^+ and π^- beams will enable one to extract the annihilation diagram as the difference in the two yields once they have been properly normalized. This is possible because of the difference in the anti-quark content of these mesons— a π^+ meson is made up of an up and an anti-down quark and a π^- is its charge-conjugate. Now, an up-quark has a charge of +2/3 the electron charge versus a down-quark which has -1/3 and hence has a higher electromagnetic coupling strength which makes the cross-section larger. Thus, the scattering of a π^- beam off

of a nucleon target will have a larger contribution from the annihilation diagram. This enables one to measure the contributions of the two diagrams in statistical terms but it does not allow the extraction of the annihilation diagram on an event to event basis. It may be possible that at p_T > 10 GeV/c the annihilation diagram dominates. These events will provide a sample rich with gluon jets that can be used to study gluon fragmentation. On the other hand, the yield from a π^+ beam will almost entirely be from the Compton diagram and will allow one to study the gluon structure function of the pion. The same argument applies for a proton beam. Thus direct photons make a very useful probe of sub-nucleonic phenomenon and along with the study of the associated jets enable the measurement of important parton model parameters.

From an experimental point of view, the major background to direct photons is from the decay of π^0 mesons into two photons. Figure I-6 shows these backgrounds processes pictorially. A symmetric decay may result in the merging of the two photons into one in the detector if the separation between the photons is less than its resolution. This case is shown in figure I-6(a). Also, the two photons may be asymmetric either in direction or in energy as shown in figures I-6(b) and (c) respectively. In the former case the two photons may miss the acceptance of the detector and its partner will appear to be a direct photon. In the latter case, the higher energy photon will be seen as a direct photon if the lower energy photon is absorbed in some intervening material or if its energy is below the threshold for detector response. Similar backgrounds exist due to decays from η and η' mesons although at much lower production rates. Due to the nature of the backgrounds discussed above, a detector for direct photons needs to have (a) a high resolution, (b) a maximum possible acceptance and (c) a large dynamic range, in order to detect photon pairs.

Given the background due to π^0 mesons, various experiments have measured the yield of direct photons versus transverse momentum (p_T) as compared to that of π^0's. Figure I-7 shows the results from Experiment E629 at Fermilab Experiment R806 at CERN. The broad band at the bottom is an estimate of the ratio as would be seen in the absence of any direct photons, or in other words, an estimate of the fraction of photon pairs that would be seen as single photons due the to reasons discussed above.

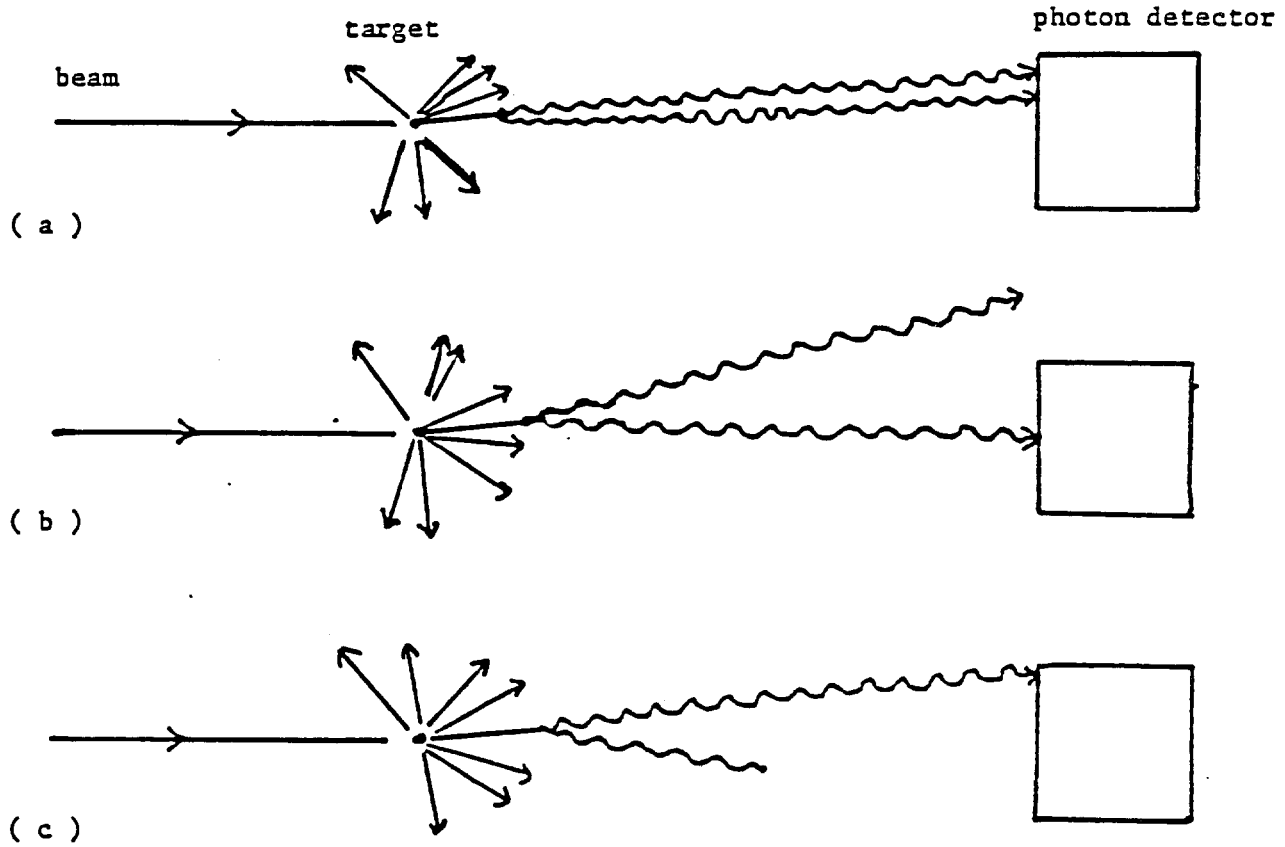

Figure I-6: A pictorial representation of background mechanisms due to π^0 decays into two photons. (a) The two photons merge into one shower in the detector. (b) One photon misses the detector. (c) A low energy photon is absorbed or converts before reaching the detector.

The experimental points give the ratio of the single photons actually measured to fully reconstructed π^0's. As can be seen, at high values of p_T, there is an excess of single photon yield. This difference is ascribed to direct photon production and after background subtraction we can see an enhancement of the relative production. Fermilab Experiment E706 aims at making full use of this enhancement by looking for direct photons at high values of p_T. It will also have a distinct advantage due to its capability of running with various beams as discussed above. In the next section, we describe the E706 spectrometer.

D. FERMILAB EXPERIMENT E706

The E706 spectrometer was designed primarily to study direct photons and the associated QCD jets in the range of $p_T > 5$ GeV/c. In order to obtain high statistics in the data it lays a particular emphasis on high acceptance, rate, and resolution. Figure I-8 shows the E706 spectrometer which will be housed in the Meson West area of Fermilab. This area has available to it a beam of secondary protons and mesons from a production target. Both positive and negative beams with a momentum of 800 GeV/c are expected. The main element of the spectrometer is a large liquid argon calorimeter (LAC) which is divided into two sections. The front half is a sandwich of lead and liquid argon with high resolution read-out planes designed to detect showers induced by photon and electrons. This is necessary for detecting single direct photons and also for the two photons from π^0 decays. The back half is a sandwich of steel and liquid argon optimized for detecting showers induced by hadronic particles. In either case, one gets a measurement of the particle energy and also, due to the high spatial resolution, of the direction of the momentum vector. A detailed description of the LAC is given in appendix A. The LAC has a hole of 40 cm in diameter along the beam direction to avoid the beam particles that do not interact. This hole is covered by a conventional calorimeter made of iron and scintillating plastic sandwich and situated immediately downstream of the LAC.

The detectors upstream of the LAC make up a magnetic spectrometer for studying the charged components of the jet and the beam fragments. The functions that it has to carry out are listed below:

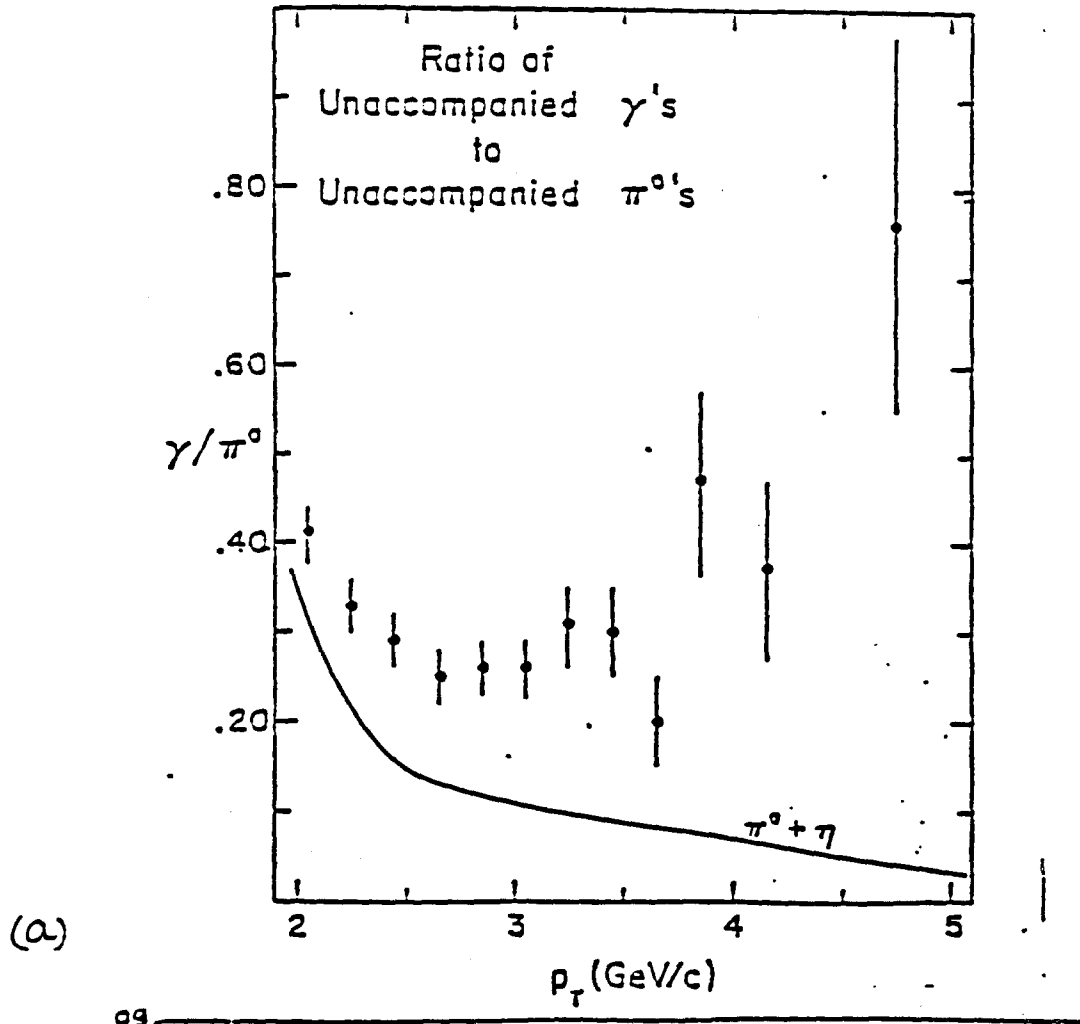

(a)

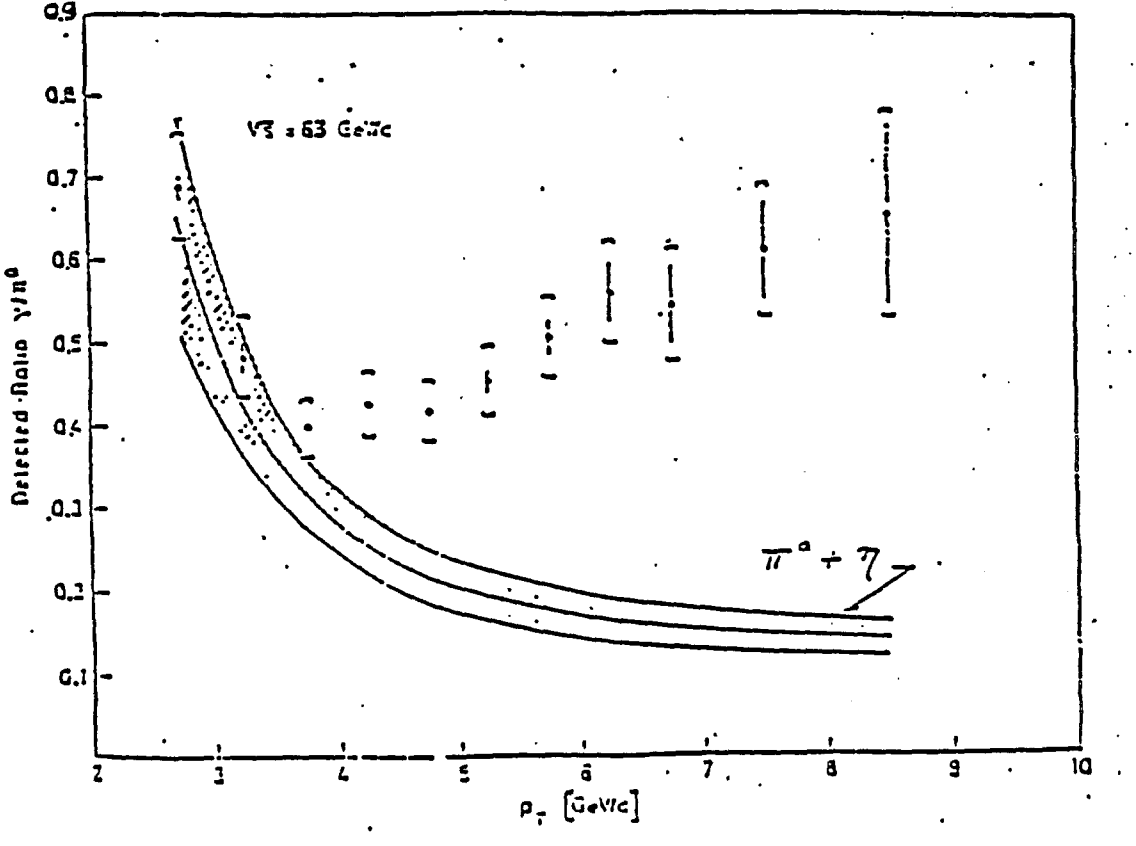

(b)

Figure I-7: γ/π^0 ratio as measured by E629(a) and R806(b)

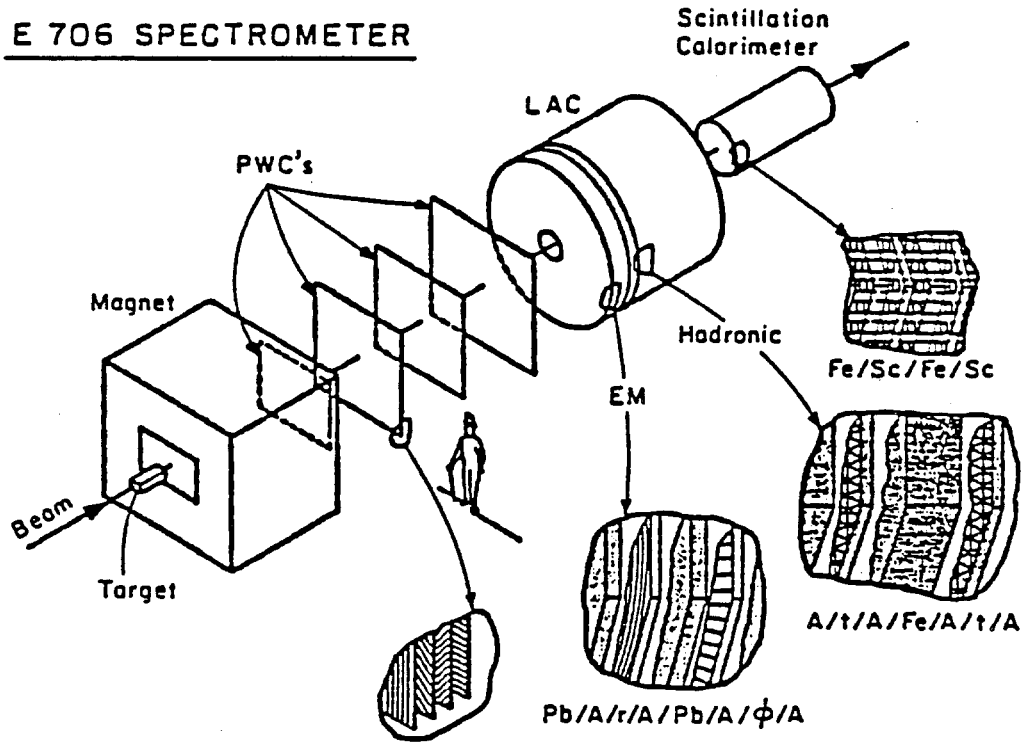

Figure I-8: The major components of the E706 spectrometer. The cut-outs detail the construction of each component.

1. Establish the coordinates of the primary interaction vertex.

2. Locate any secondary vertices that may be present due to secondary interactions and/or the decay of short lived states.

3. Measure the momenta of the charged particles.

An interaction vertex can be reconstructed by tracking the charged particles emerging from the target and extrapolating the tracks to intersect with the initial track left by the beam particle. This motivates the use of a tracking telescope that encloses the target. The first two functions together imply that the ability to separate the primary and the secondary vertices depends on the precision in locating them along the beam direction. This in turn depends on the angular resolution of the tracking device. A bending magnet placed behind the telescope and followed by another set of charged particle tracking detectors can accomplish the third function. In order to have a large acceptance for the magnetic spectrometer we need a large gap between the magnet poles. At the same time, to keep the magnet poles from shadowing the LAC (that is, to preserve the large acceptance of the LAC), the magnet should be placed as close to the target as possible. This argues that the tracking device in front of the magnet should be compact along the beam direction. Given this compactness we can see that, for achieving comparable angular resolution in both the upstream and the downstream detectors, we need high spatial resolution in the transverse direction for the upstream detector. The downstream detectors are made up of four stations of Proportional Wire Counters (PWC's). Each station consists of four planes of PWC's with sensing wires in four views as shown in Figure I-8. The wires are spaced at 2.5 mm and the separation between the stations is 1.1 m. SMD's can be made with detector elements spaced at 50 μm and along with their capability to run at high rates prove to be an ideal choice for the detector upstream of the magnet. In the next chapter we will describe the front-end of the E706 spectrometer and discuss these questions more quantitatively. At this point, however, we digress briefly to introduce SMD's.

CHAPTER II.
SILICON MICROSTRIP DETECTORS

A. PIN DIODES

PIN diodes have been used as charged particle detectors in Nuclear physics for about two decades. Figure II-1(a) shows the schematic of one such device in operation. It is made from a very pure crystal of silicon (impurity levels of approx 10^{12} cm^{-3}) which has been highly doped (approx 10^{19} cm^{-3}) with p-type impurities on one side and n-type on the other to depths of approx 1 μm. The bulk silicon (or the I region) is a few hundred μm in thickness and is usually n-type. As shown in Figure II-1(b), this results in a sharp diode junction at one interface and a small barrier on the other. On biasing the diode in the reverse direction, the free carriers are swept out and an electric field is set up. Figures II-1(c) and (d) show the space charge distribution and the electric field. The depletion layer at the junction expands into the I region to a depth given by, $d = 5.3 \times 10^{-5} (\rho V)^{1/2}$, where ρ is the resistivity in Ω-cm and V the applied voltage. Sufficient voltage is applied to deplete the entire I region. For a resistivity of 5000 Ω-cm and a thickness of 300 μm the voltage required is about 70 V resulting in an electric field strength of 2.3×10^{5} V/m which is well below the breakdown level (approx 10^{7} V/m).

A charged particle passing through the detector will create electron-hole (e-h) pairs by ionizing the medium, as shown in the band diagram of Figure II-1(e). The e-h pairs are swept out by the electric field creating a small current signal which can be amplified. For a minimum ionizing particle (m.i.p.) the energy loss is 280 eV/μm. Even though the band gap of silicon is 1.1 eV, on the average it takes 3.6 eV to create an e-h pair, the rest appearing as kinetic energy or lost to phonons. For a 300 μm device the signal on the p-side is approx 24,000 holes. The collection time for the charge depends on the the strength of the electric field (E) and the mobility of the free

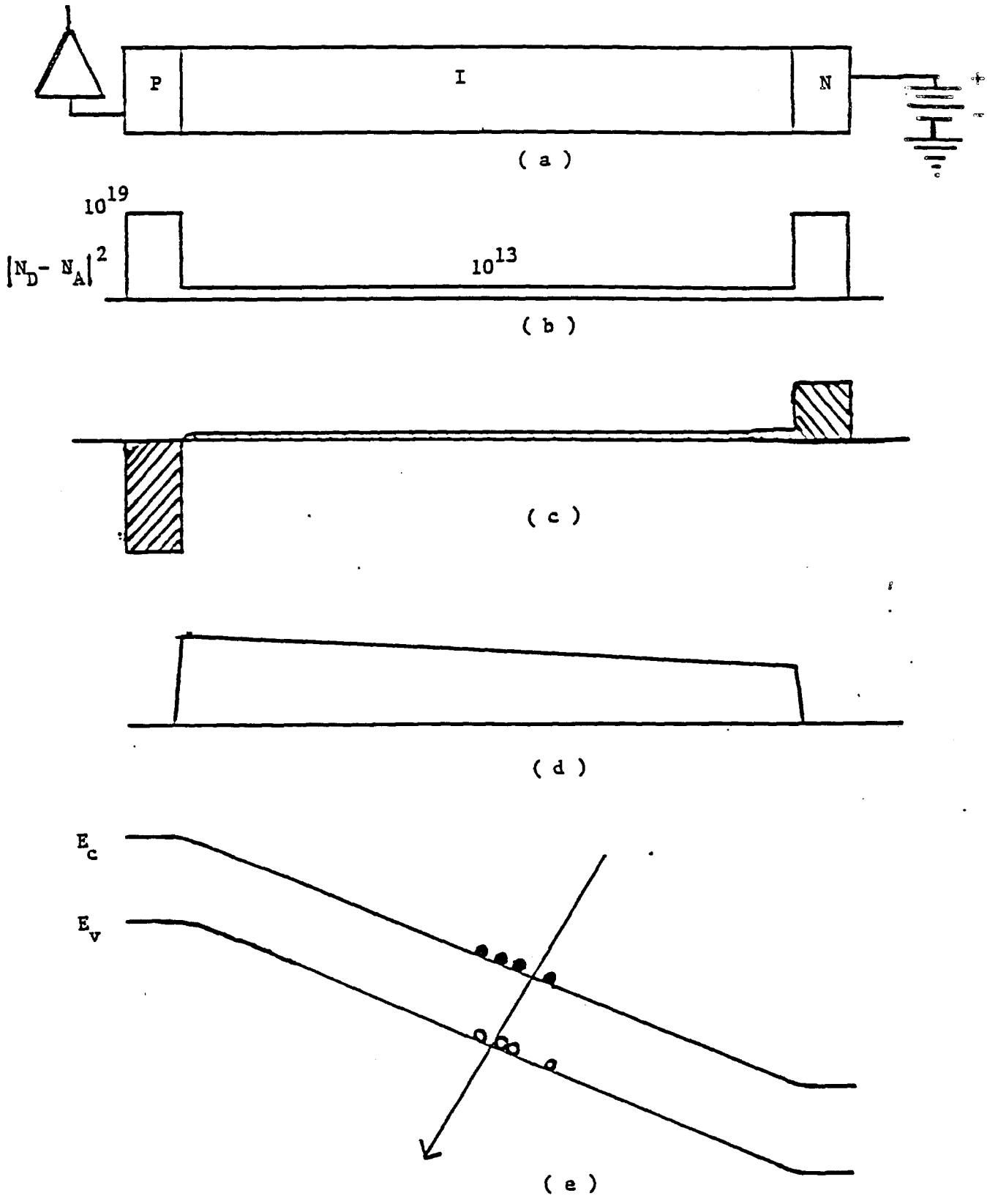

Figure II-1: PIN diode as a particle detector. (a) The PIN structure and detector circuit. (b) The dopant levels. (c) Space charge density under reverse bias. (d) Electric field strength. (e) Band diagram showing the creation of electron-hole pairs.

carriers (μ) which for a p-side readout are holes. The velocity of the holes is given by, $v_h = \mu_h E$ and the collection time is $t_c = d/v_h$. For d = 300 μm, E = 2.3 X 10^5 V m^{-1} and μ_h = 480 cm^2 V^{-1} s^{-1}, the collection time is 26 X 10^{-9}s, thus making the PIN diode a fast device.

In 1980 J. Kemmer[15] adopted the planar process, used and developed by the silicon industry for the manufacture of integrated circuits, to segment one of the electrodes into an array of independent diodes as shown in Figure II-2. This converted the PIN diode to a silicon microstrip detector, a powerful new tool.

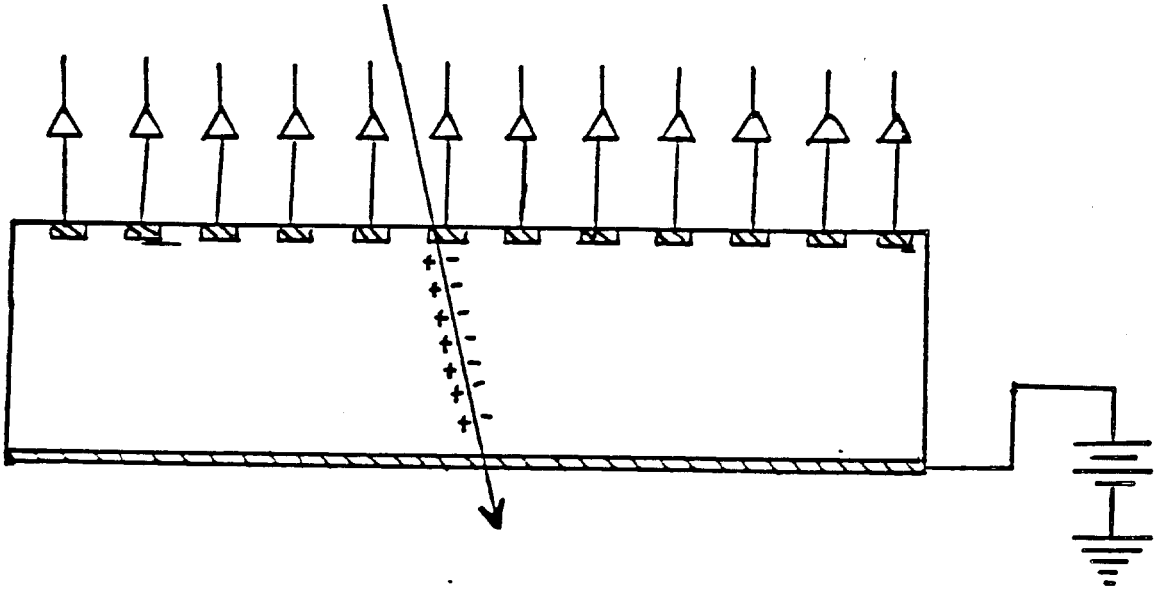

Figure II-2: The microstrip version of a PIN diode.

The structure can be better understood by looking at Figure II-3 which shows the face-view of an SMD with a total of 600 diodes. The diode strips are 50 μm apart and cover an area of 3X3 cm^2. The blow-up of one of the corners shows rectangular pads on every other strip in a staggered fashion. The remaining strips have a similar pattern on the other side. Under reverse bias the p-n-p structure of two adjacent strips ensures a high impedance between them and hence maintains them as independent detectors. The lower limit on the useful pitch for SMD's comes from considerations of the energy loss characteristics. There is no advantage in making the pitch any smaller than the expected shift in the centroid of the ionization charge. It has been estimated that the probability, for a shift outside a cylinder with a diameter of 5 μm, is only 10 % for a

300 μm thick detector[16]. This puts a natural lower limit on the pitch for improving the resolution. In section II.B we will discuss the energy loss in more detail. In reality, the limiting factor comes from the techniques needed to intstrument an SMD. Detectors with 20 μm pitch have been successfully made and used[17].

The steps involved in the planar process are shown in Figure II-4. A wafer is sliced from an ingot of high purity silicon and baked in an oxidizing atmosphere at about 1100°C so that it is covered with a thin layer of silicon dioxide. Windows are etched in the oxide using photolithographic techniques and dopant ions are introduced on either side preferably by ion implantation. This is followed by annealing and another stage of oxidation. Similar steps are taken to etch a pattern of windows and deposit aluminum on top of the diodes. After some more annealing the SMD is ready. The aluminunization allows one to ultrasonically bond a very thin aluminum wire to the pads at the end of the diode elements on one end and a printed circuit board on the other. In section III.C we discuss this and other techniques that are employed in a scheme to mount an SMD and couple it with amplifiers.

It should be mentioned here that the simple description of the planar process given above may deceive one into disregarding the complexities of the art. Very few industrial houses and labs have the facilities and the technical expertise to successfully carry it out. If the oxide treatment is done without utmost care certain defects and impurity states creep in and render a wafer unusable by causing high leakage currents to flow. As we will see in the next section, our device requires the use of SMD's of surface areas of 3X3 cm^2 as well as 5X5 cm^2. In each case the strip pitch is 50 μm implying 600 and 1000 strips each respectively. Hughes Corp.[18] was successful in manufacturing the former based on a design provided by us. The latter kind were obtained commercially from Micron Semiconductors[19]. In the next section we discuss the design and the performance characteristics of the SMD telescope.

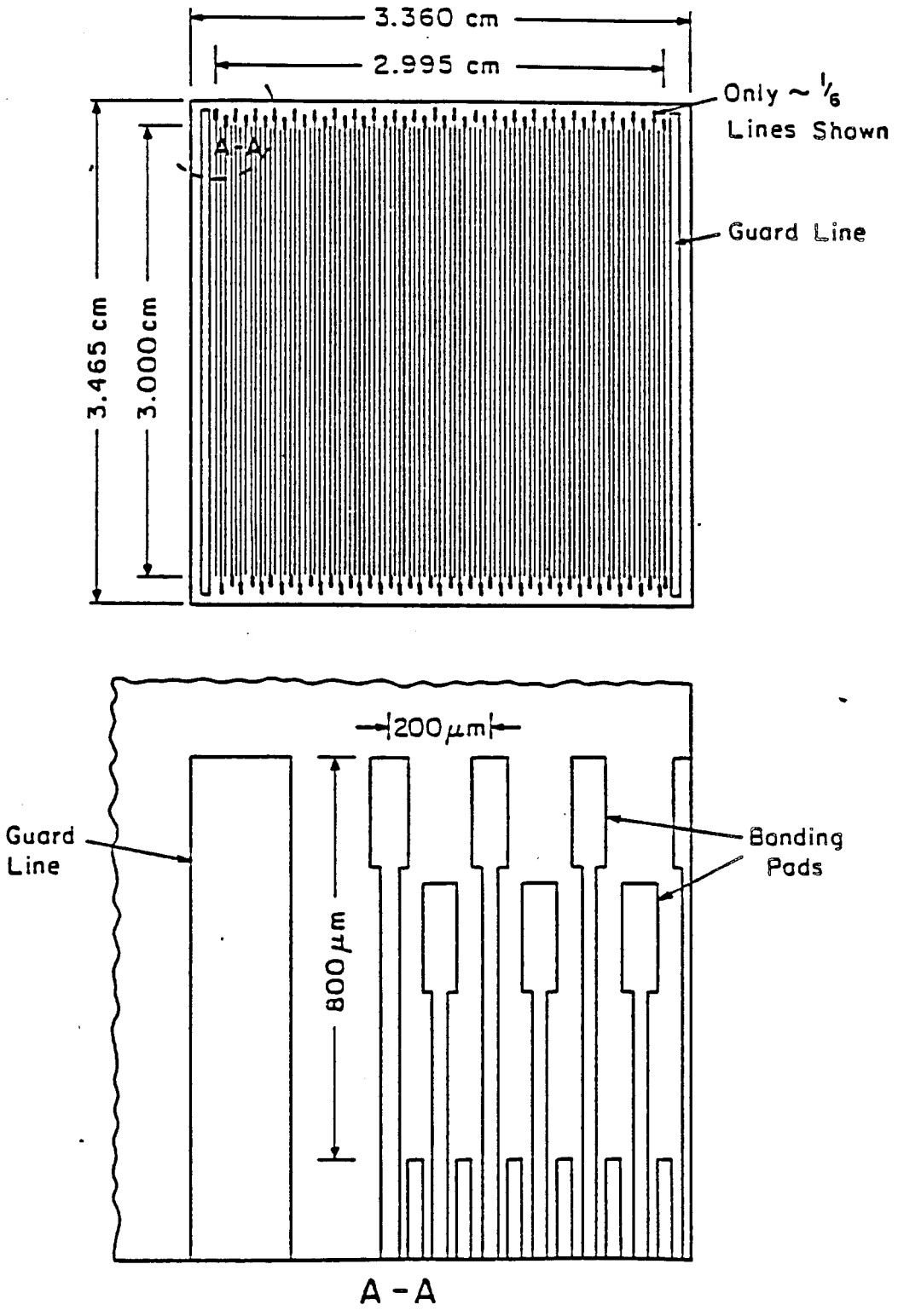

Figure II-3: Face-view of an SMD showing the pattern of PIN diode elements. The blow-up shows the pads used for ultrasonic bonding.

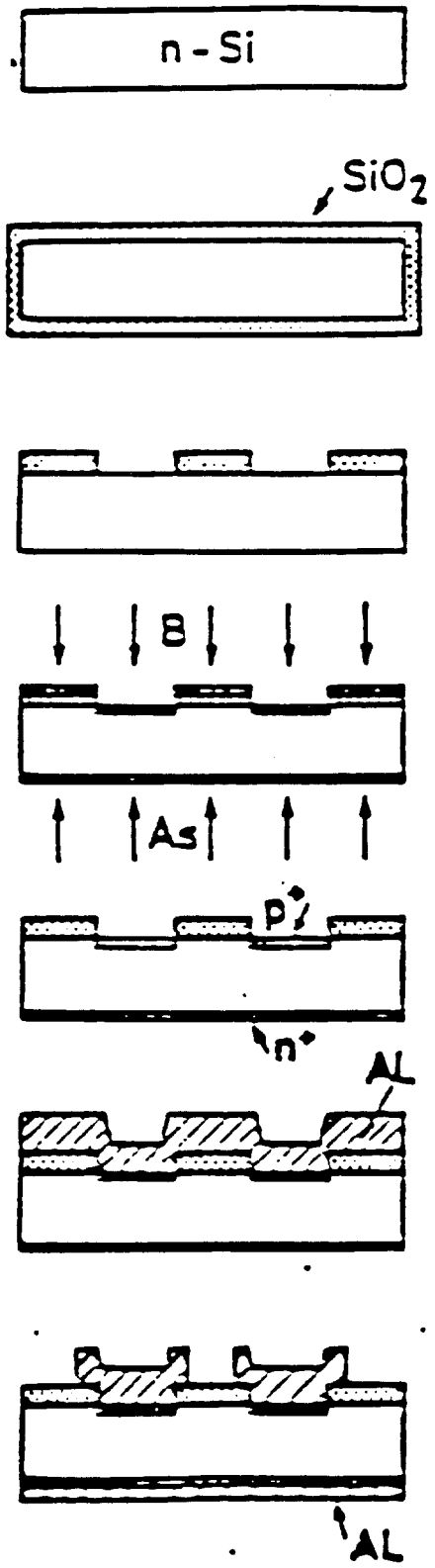

— n-Si WAFFER

OXIDE PASSIVATION

OPENING OF WINDOWS

DOPING BY ION IMPLANTATION
B : 15 keV, 5×10^{14} cm^{-2}
As: 30keV, 5×10^{15} cm^{-2}

ANNEALING AT 600°C, 30 MIN

AL METALLIZATION

AL PATTERNING AT THE FRONT

AL-REAR CONTACT

Figure II-4: The major steps involved in the planar process for the manufacture of SMD's.

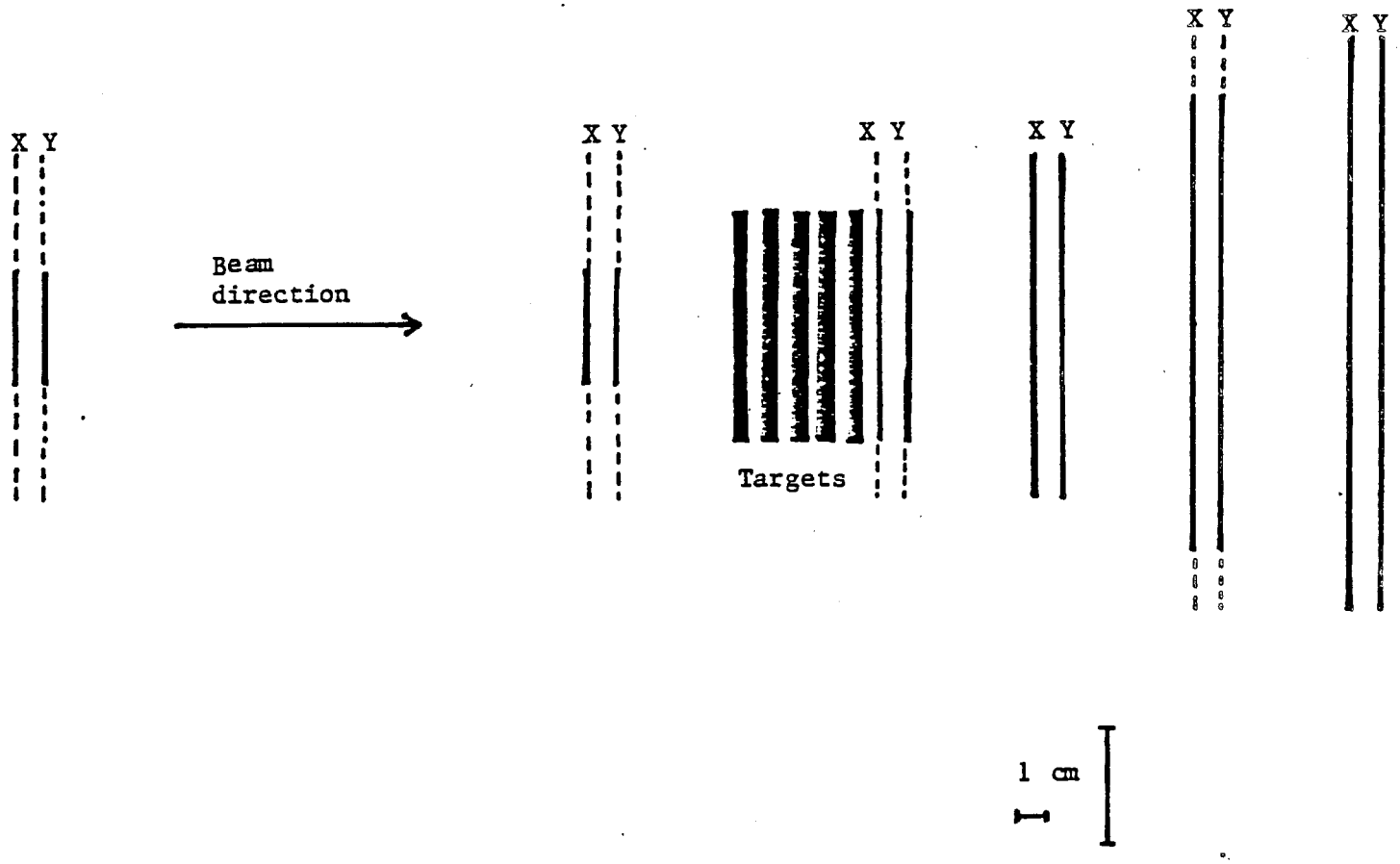

Figure II-5: The segmented target region of E706. The broken lines show the sizes of the wafers used while the solid lines show the instrumented region.

B. THE FRONT-END OF E706

The detailed design of the SMD telescope is shown in Figure II-5. The vertical scale has been magnified for clarity. The wafers are put in pairs with their lines perpendicular to each other to make up X-Y modules. There are 4 modules with surface area of 3X3 cm^2 and 2 with 5X5 cm^2 making up a total of 8800 strips available for instrumentation. The thick lines on each module show the fraction of the wafer that is actually instrumented and define the sensitive cone. This scheme uses 6600 channels of electronics. The target is segmented and varies in thickness depending on the material used. As mentioned earlier the SMD telescope serves the dual function of tracking charged particles before the magnet for momentum measurements and also for reconstructing interaction vertices. Now we can evaluate the performance of this design. Figure II-6(a) shows a simplified version of the magnetic spectrometer with only the first and the last planes of the SMD's and PWC's. This allows us to get an estimate of relevant quantities without detailed analysis. The bending angle for the particle in the magnet is given by,

$$\theta = 0.3 \frac{B.L(\text{Tesla-m})}{P\ (\text{GeV/c})} \qquad (\text{II}-1)$$

implying a momentum resolution of,

$$\frac{\Delta P}{P} = \frac{P}{(0.3\ B.L)}\ \Delta\theta \qquad (\text{II}-2)$$

where $\Delta\theta$ is the total uncertainty in the measured angle. Assuming no error in the z-location of the planes, the main contributions to the error come from the spatial resolutions in the tracking devices and the smearing due to multiple scattering. The average angle due to multiple scattering, for a particle of momentum p, in a thickness x of a medium with a collision length X_o, is given below.

$$\langle\theta\rangle_{M.S.} = \frac{21}{\sqrt{2}} \frac{1}{\beta c} \sqrt{\frac{X}{X_0}} \frac{1}{P\ (\text{MeV/c})}$$

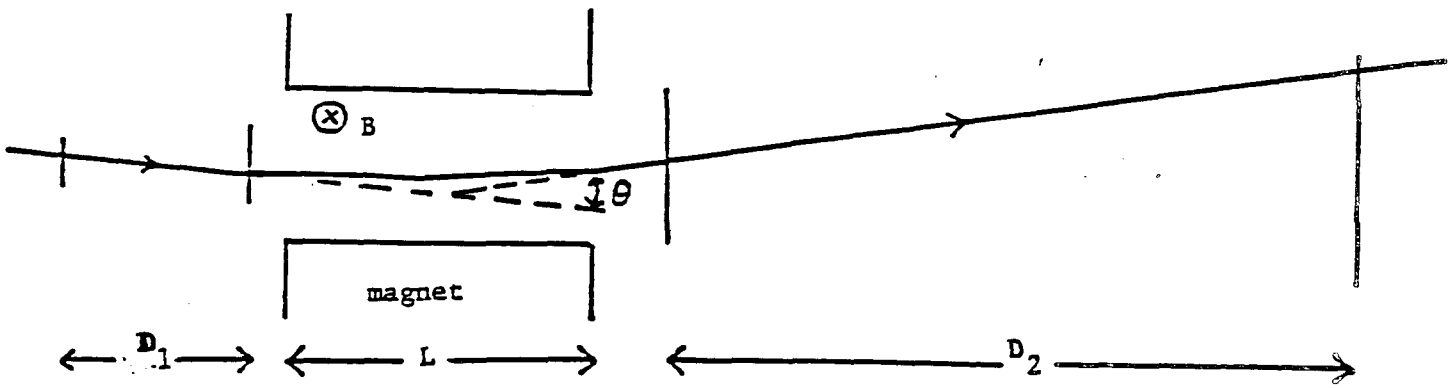

(a)

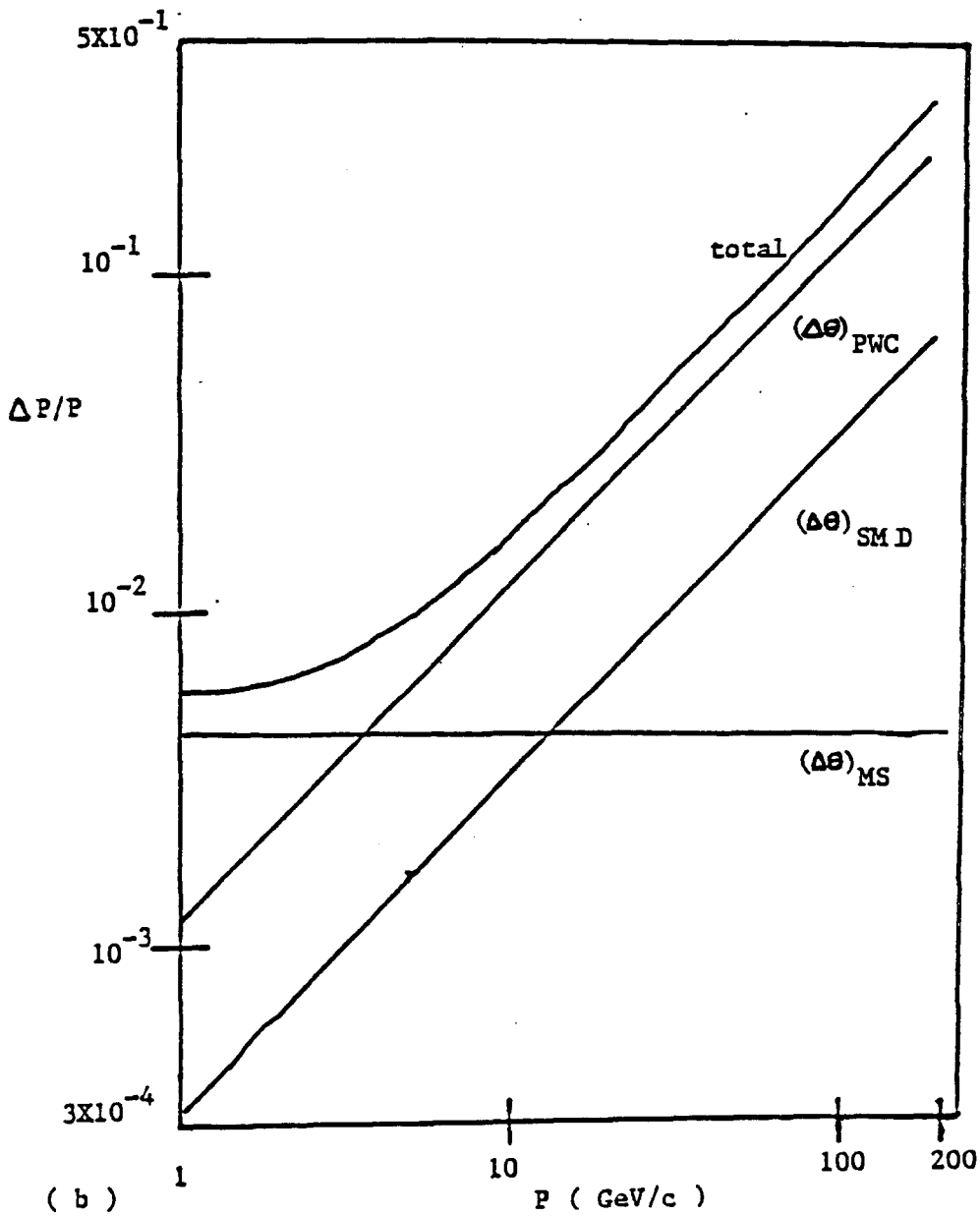

(b)

Figure II-6: A simplified version of the magnetic spectrometer (a), and an estimate of the momentum resolution based on this design (b).

$$\text{or} \quad \langle\theta\rangle_{MS.} = \frac{15.5}{P(MeV/c)\,c}\sqrt{\frac{X}{X_0}} \qquad (II-3)$$

For a track made from two hits in detectors with a pitch d and placed a distance D apart the uncertainty in the measurement of the slope is given by,

$$(\Delta\theta)_{exp} = \sqrt{2}\,\frac{d}{\sqrt{12}}\cdot\frac{1}{D} \qquad (II-4)$$

Figure II–6(b) shows a plot of momentum resolution over the expected range of momenta in E706 based on the angular uncertainty from different sources. The overall curve with the errors added in quadrature is also shown. A total of 2 mm of silicon is used for x and multiple scattering in the PWC's is ignored. The value of 1 Tesla-meter is used for H.L, which is the expected field strength. The angular resolution of the SMD's can be improved by putting them further apart but, as can be seen, it will not improve the overall momentum resolution. Hence, in the interest of maximizing angular acceptance, and using a maximum of 6600 channels of electronics, this angular resolution is acceptable. Also, it can not be improved much further before the multiple scattering starts to dominate.

We can also get a rough estimate on the z-resolution for locating interaction vertices in a similar manner. Figure II–7 shows a simplified version of the SMD telescope with a beam track constructed from two hits and another two hits from a track emerging from the primary interaction vertex. The angle $\Delta\theta$ is represents the total uncertainty in the angle from the sources discussed above. From this picture we get,

$$\frac{\Delta z}{z} = \frac{\Delta\theta}{\sin\theta}$$

$$\text{or} \quad \Delta z = \frac{z}{\sin\theta}\left((\Delta\theta)^2_{exp} + \langle\theta\rangle^2_{M.S.}\right)^{1/2} \qquad (II-5)$$

Clearly this depends on the momentum of the particle and the angle θ. Taking θ = 60 mr and p = 5 GeV/c, which are typical, and using the numbers for the angular

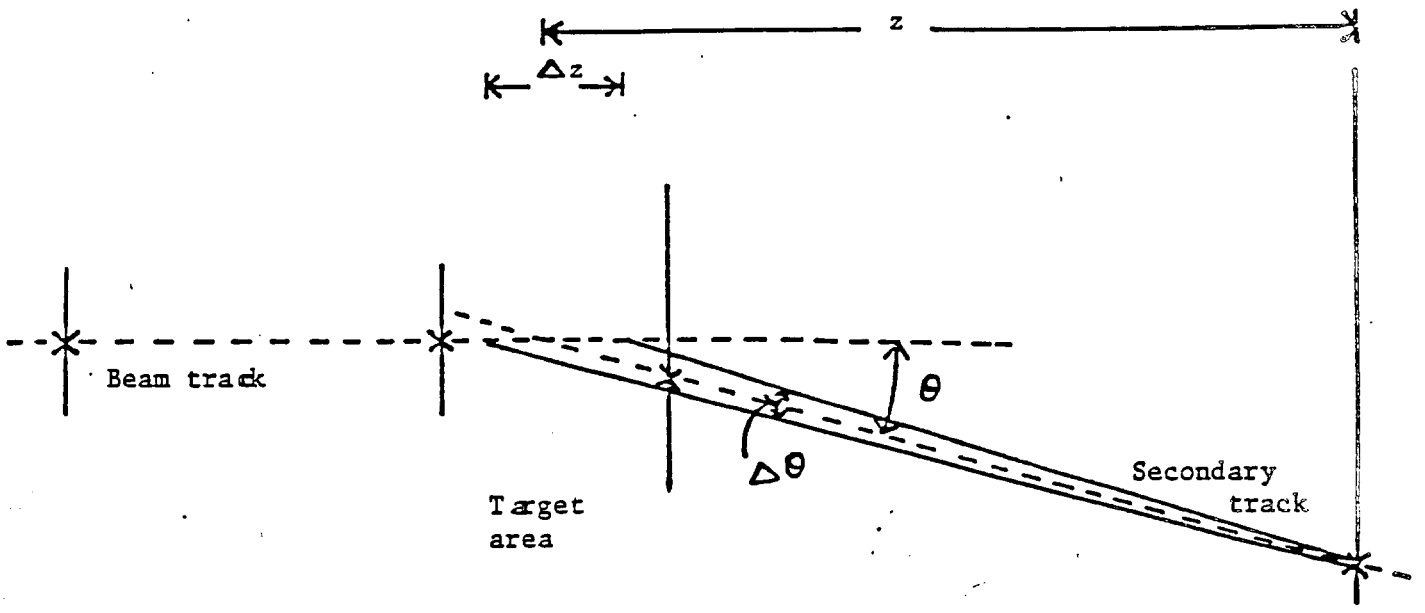

Figure II-7:

uncertainty from above, we have Δz = 3 mm. The resolution will be improved by taking all the available tracks and comparing them in both X and Y views. In practice this is done by matching tracks with hits and finding the best fits and then matching vertices with tracks, the entire procedure involving extensive use of computer software. Nevertheless, the crude estimates arrived at here are very close to the answer from sophisticated analyses. In chapter 5 we will present some results based on the software under development.

C. INSTRUMENTATION SCHEME FOR X-Y MODULES

Here we are concerned with the problem of taking up to a thousand signal lines originating 100 μm apart on either side of an SMD to locations typically a mm apart which is a reasonable density for discrete electronic circuits. This is usually accomplished with the help of printed circuit boards (PCB's) designed to have a pattern of traces that fan-out. Figure II-8 shows our scheme for doing this. It consists of two distinct stages of lines going from a higher to a lower density and a third one that

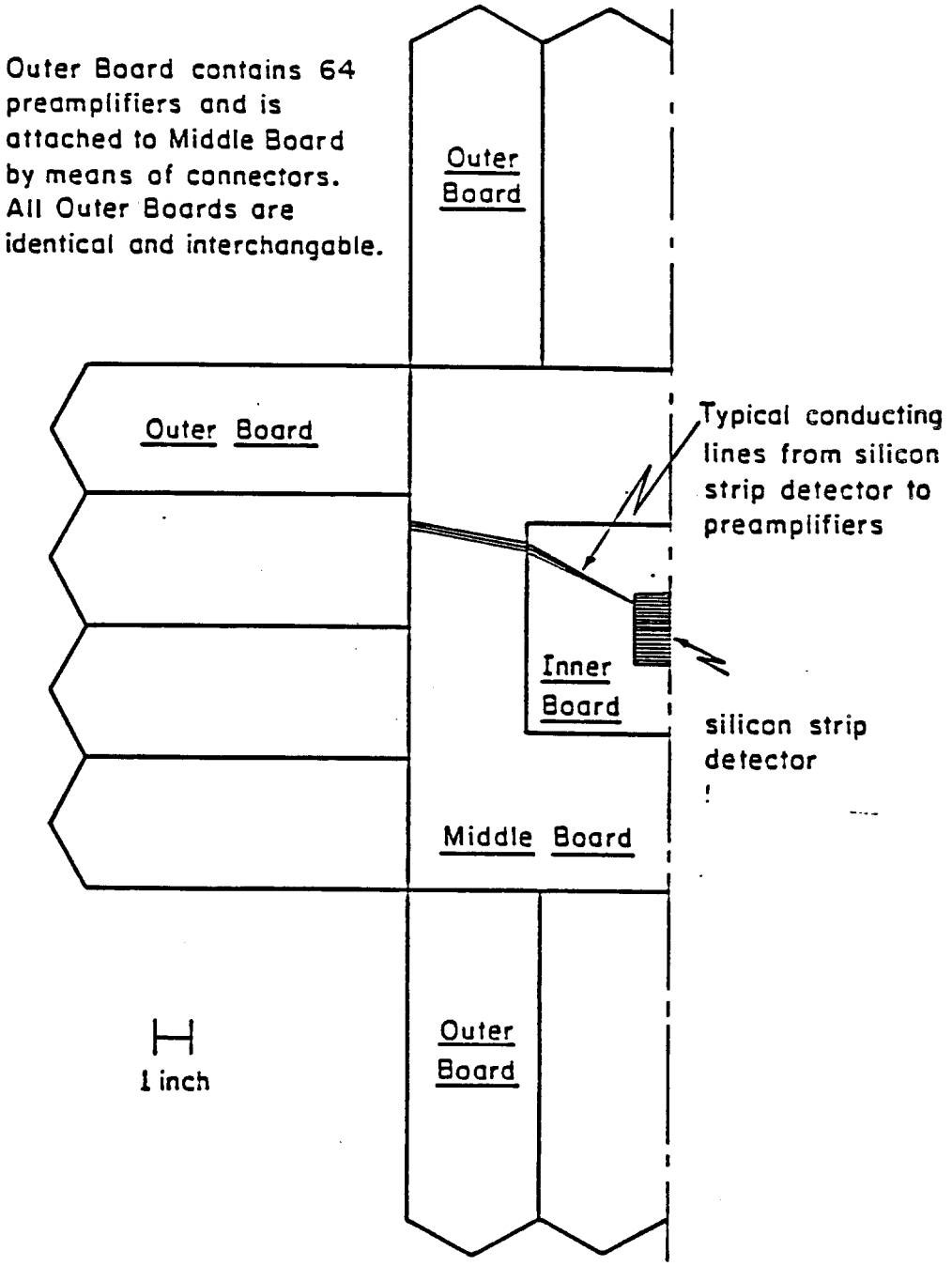

Figure II-8: A schematic of the three stage fan-out used for instrumenting SMD's. A common design serves both 3X3 cm^2 and 5X5 cm^2 wafers using different Inner boards.

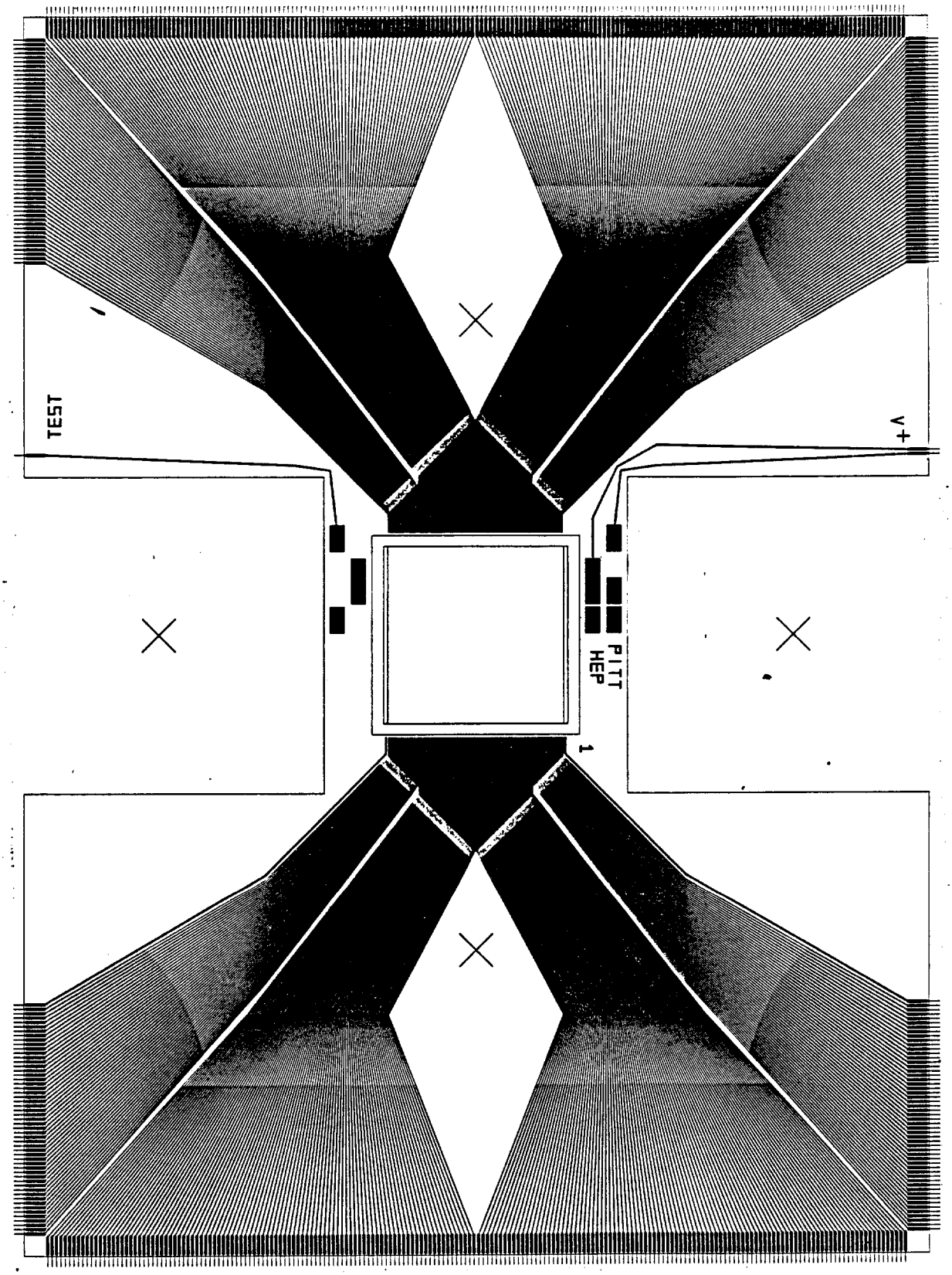

Figure II-9: The design of the mask used for fabricating the fan-out printed circuit board. The details are partially lost in photocopying the actual film.

routes them to preamplifiers. For obvious reasons they have been called Inner, Middle and Outer boards. There are two well defined advantages of this modular design. First, the three boards can be easily separated into different classes of PCB technology and hence allow for the fabrication to go on in parallel. Because of the fine lines the Inner board requires very careful processing whereas the Middle board has thicker lines and does not need special treatment. It was found that the parameters needed in the processing for the two different densities compete with each other and hence they are best treated separately. The Outer board manufacture requires techniques for making plated-through holes and wave-soldering which make it different from the others. Although the Middle board also has plated-through holes the clearly different features in this case are its large size and low density. Second, the design allows us to have common Middle and Outer boards for the 3x3 cm^2 and 5X5 cm^2 wafers as long as we make two different Inner boards to match the lines of the Middle board. This allows for a greater flexibility in the design and makes future upgrades in the apparatus easy. The design and fabrication of the Inner boards was done mostly at the University of Pittsburgh with some steps in the processing done in industrial houses.

Figure II-9 shows the lay-out of the PCB used for instrumenting the 3X3 cm^2 wafer. It is a photocopy of the actual mask used in the fabrication. It was designed using computer graphics developed by us. The software required is not very complicated in that it only has to generate commands that have the format understood by a photoplotter. Photoplotters typically have a precision of 10 μm and they can be used to expose a film with a collimated light source in a pattern defined by digital commands. The mask shown here was made on one such machine available at Cad Services Inc[20]. The same software was later used to make the mask for the 5X5 cm^2 wafer and a few other masks for various PCB's needed for the electronic circuits. Appendix B contains the details of this effort. The steps involved in making fine-line PCB's are shown in Figure II-10. Copper-clad G-10 is etched on both sides so that the copper laminate is reduced to a thickness of 10-15 μm and then coated with a photo-resist material. These two steps were done at Compunetics Inc.[21] and Kepro [22] respectively. The material is exposed to ultra-violet light through the mask and developed to obtain the pattern reproduced in the form of hardened resist. It is baked to further harden the resist. This is followed by the crucial step of etching the exposed

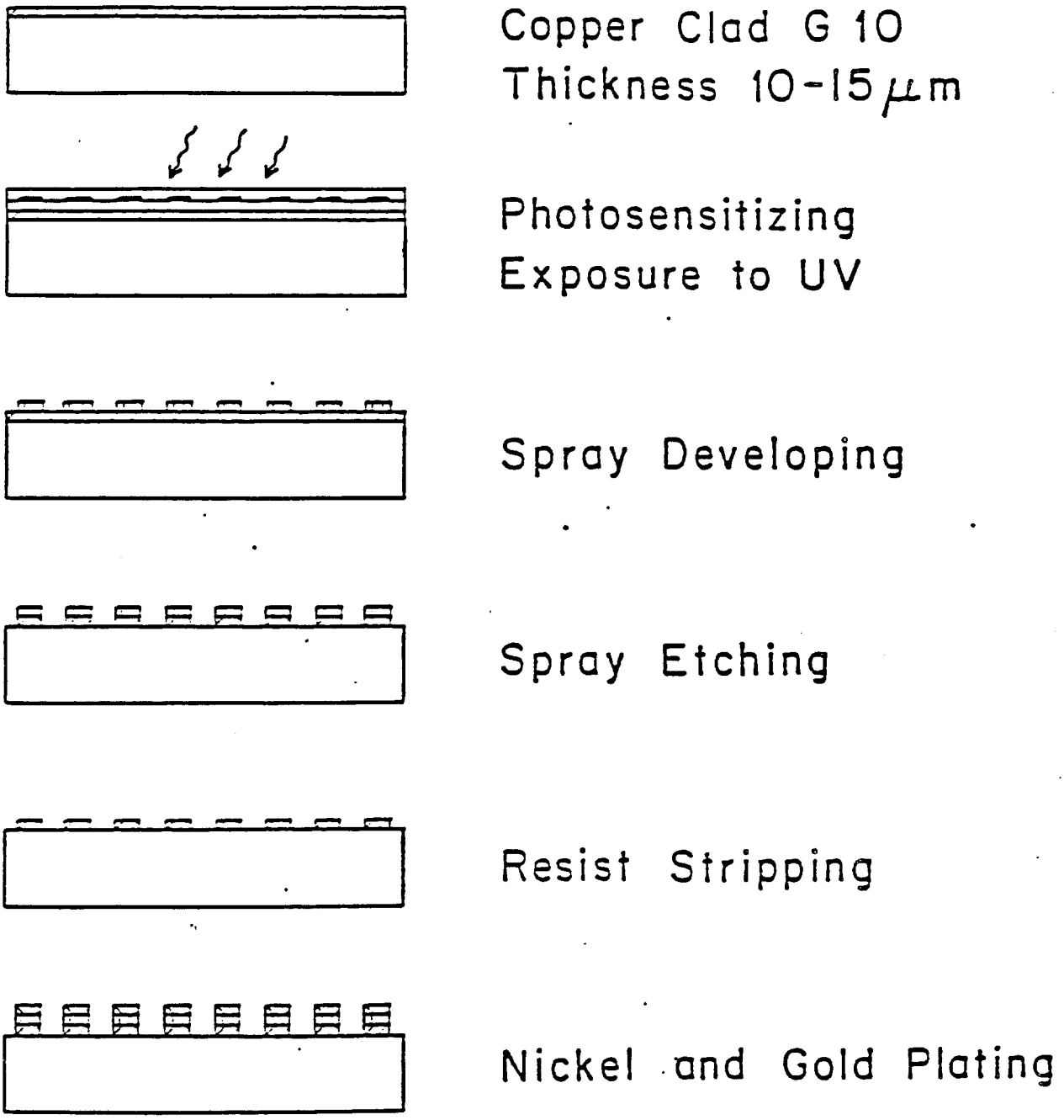

Figure II-10: Steps involved in making a fine-line PCB.

copper with a spray of $FeCl_3$, while making sure that the copper under the resist does not get etched. It was found, after many rounds of changing the etching time and temperature of the etchant, that it was not possible to accomplish this with spray etching alone. A successful method evolved which involved partial spray etching followed by etching by hand using cotton swabs and a weak solution of $FeCl_3$. The resist from the etched board is stripped and the bare copper is cleaned in a weak acidic solution. The final step in the process is electroplating the copper lines first with a layer of nickel and then a layer of gold. The wafer fits into a window which is machined out in the center of the Inner board. The n-side is attached to the copper surface on the other side of the board with conducting epoxy so that it can be connected to a dc power supply. The connection between the aluminum on the p-lines and the gold on the PCB lines is made by a thin aluminum wire of 25 μm diameter. The wire is rubbed at ultrasonic frequencies on the aluminum surface till the locally generated heat creates bonds between the two. A similar bond is made at the gold surface and then the wire is cut. All this is made possible using a commercial ultrasonic bonding machine which was successfully put into operation at Pitt.

The Middle boards have lines that start with pads on locations matching the pads on the periphery of the Inner board and fan-out to edge connectors all along its own periphery. The Outer boards have the female half of these connectors and they plug into the Middle board. The boards were manufactured by Compunetics Inc. based upon designs provided by us. We will return to the Outer boards in chapter 3 when we discuss preamplifiers. The connection between the Inner and Middle boards can not be done using commercially available connectors because the lines are only 750 μm apart. We developed a method of soldering thin strips of copper foil between corresponding pads using low-temperature indium solder. The special solder is necessary because the copper laminate on the Inner boards does not stand up to high temperatures and the traces come off. Patterns with a large number of 500 μm wide strips at a pitch of 750 μm are etched on 25 μm thick copper foil, in a process similar to PCB making, to produce what we call a 'harness'. A thin strip of kapton tape is laid along its length to add strength to the foil. The ends of the strips, as well as the pads on the two boards, are tinned with indium solder. Once these harnesses are soldered to the boards the wafer is ready for use. Figure II-11 shows a photograph of a completed X-Y module containing two such wafers.

We will return to the X-Y modules when we discuss the scheme for the assembly of the entire telescope in chapter IV.

Figure II-11: A photograph of a fully assembled X-Y Module showing one plane of a 5X5 cm^2 SMD

CHAPTER III.
PREAMPLIFICATION AND NOISE

A. INTRODUCTION

The signal from a minimum ionizing particle traversing 300 μm of silicon is 24,000 e-h pairs appearing over about 25 ns. Unlike gas ionization detectors, in SMD's there is no electron multiplication and hence this is the net charge in the signal. This signal has to be amplified before it can reach the sensitivity of conventional circuits. In this chapter we discuss the evolution of a two-stage amplification scheme. As it turns out the first stage is the most critical and here we will present our process of arriving at a successful solution.

B. BEAM TEST OF AN SMD

We exposed an SMD in a beam of electrons at the A-2 test beam at Brookhaven National Lab to test a simple scheme of amplification. The test beam consisted of mainly π's and electrons from a production target. A bending magnet could be used to select a beam mometum in the range 3 - 8 GeV/c. The experimental set-up is shown in figure III-1(a). The three scintillation counters were used to obtain a charged particle trigger. In the event of a 3-fold coincidence the discriminator sent out a 60 ns wide trigger pulse. A 5 ms wide pulse was fed back as a veto signal to the coincidence unit. This ensured a maximum trigger rate of 200 Hz. This scintillator telescope enabled us to select charged particles that were perpendicularly incident on the SMD.

As shown in Figure III-1(b) the amplification scheme consists of two stages. The first stage is a preamplifier (preamp) built by us based on a circuit shown in Figure III-2(a). The first element at the input is a common base transistor circuit which is followed by a common emitter amplifier. The CB circuit ensures a low input

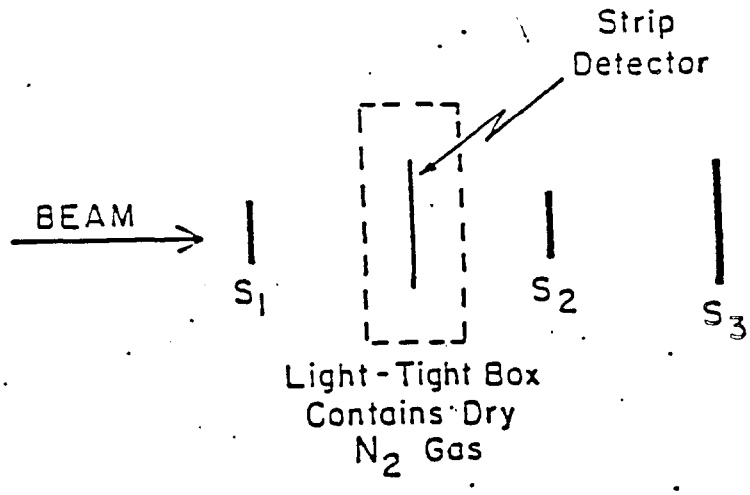

(a) Plan View of Apparatus

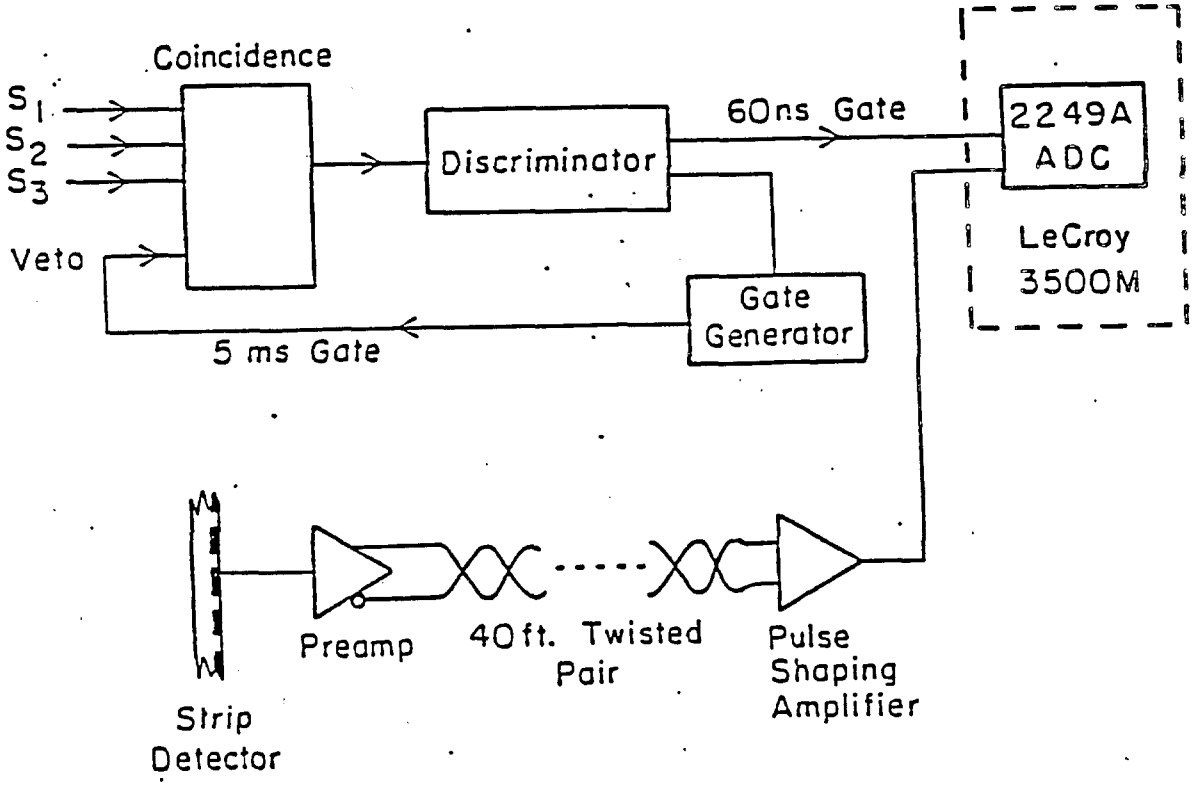

(b) Electronic Schematic

Figure III-1: The experimental set-up for the beam-test of an SMD (a) and the amplification and read-out electronics scheme (b).

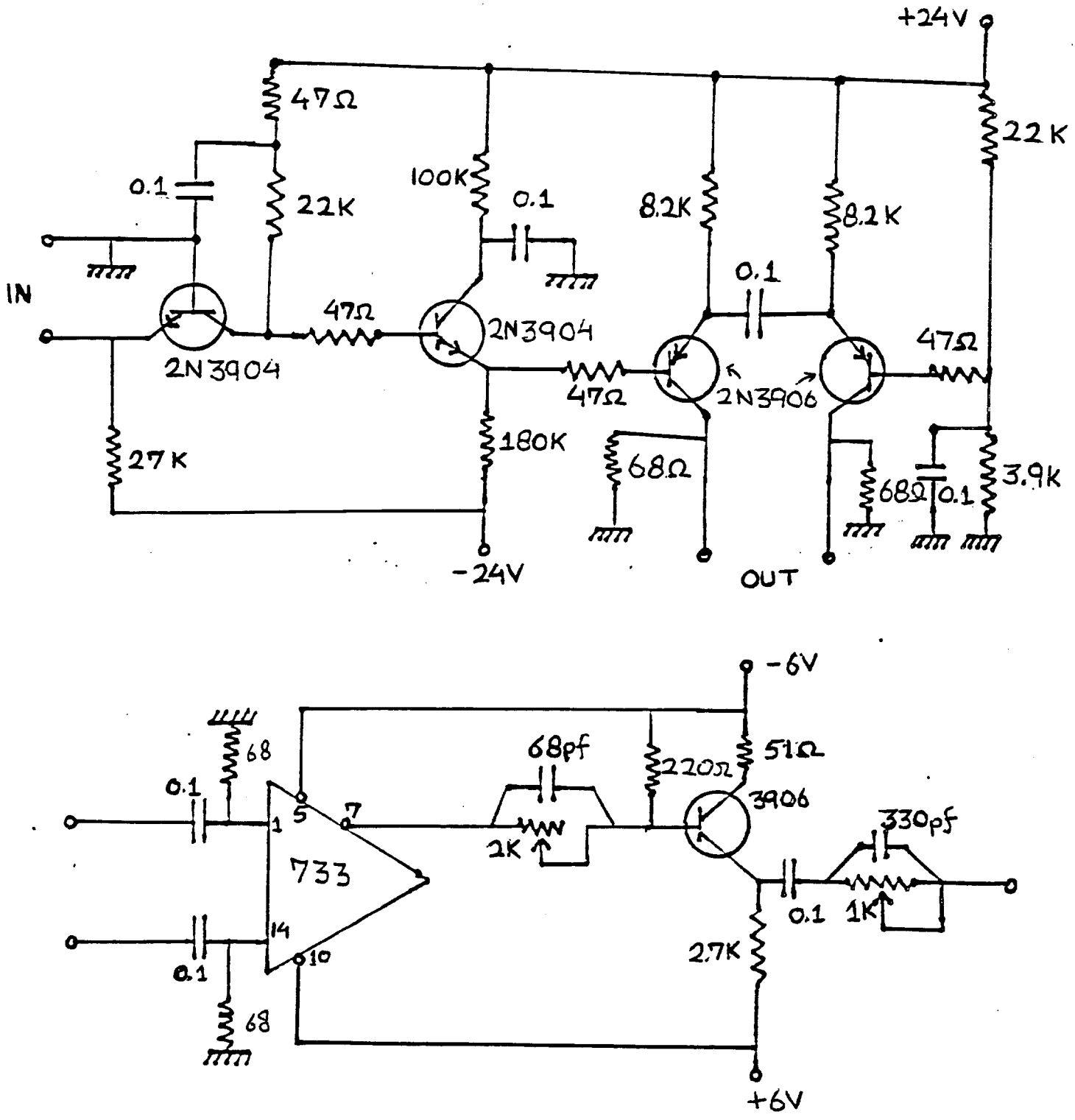

Figure III-2: The circuits for the preamplifier (a) and the post-amplifier (b).

impedance and hence a short RC time (few 100 picoseconds) constant for the charge on the SMD to decay into the amplifier. This makes the preamp a fast device. The CE cicuit ensures a high current gain thus providing us with a fast current amplifier. It has a line driver push-pull amplifier circuit at the output which is capable of delivering a signal through a 100 m long cable. The next stage is a post amplifier with a wide-band differential amplifier integrated circuit (IC) as its main element. The schematic is shown in Figure III-2(b). The output of the IC is fed into a pair of RC element networks called pole-zero cancellation circuits. These are used to restore the tail-end of the pulse to ground. A total of 48 channels of these circuits were used in the test. The trigger was used to open a gate in the analog to digital converters (ADC's) that integrated the outputs from the post-amps. The gate width was 60 ns. A LeCroy 3500M multichannel analyzer (MCA) controlled the readout and histogramming of the digital data from the ADC's. The schemes for digital control and read-out of a large number of channels will be discussed in more detail in chapter 4. For now, looking at the output of only one channel of the electronics will suffice for our understanding of the amplification scheme.

Figure III-3 shows a histogram of the integrated charge from an ADC for a typical strip on the SMD. This plot needs some explanation as we will discuss quite a few similar ADC curves in the course of this chapter. The vertical line at the peak on the right corresponds to the pulse height that would be produced by the signal from a mip. The dotted curve around it is a Gaussian with a width of 155 electrons which is the statistical error on 24000. In reality the amount of charge deposited by a mip is governed by a Landau distribution for energy loss through ionization. The Landau distribution has to be modidied for our case. The need for the modification arises because of two reasons. First, in practice some of the ionization charge leaks out of the detector. These are the so called δ-ray electrons and they can cause fluctuations in the amount of charge actually collected. Second, the atoms in the silicon crystal are bound rather than free as in gas ionization detectors. The original calculations were done by considering free atoms. The energy transfer to atoms at a large distance from the particle's track are affected by the structure of the electron energy levels. The curve has been studied very thoroughly[23] and the fluctuations in charge deposition have been measured[24]. It is shown that the effect due to charge leaking out is not

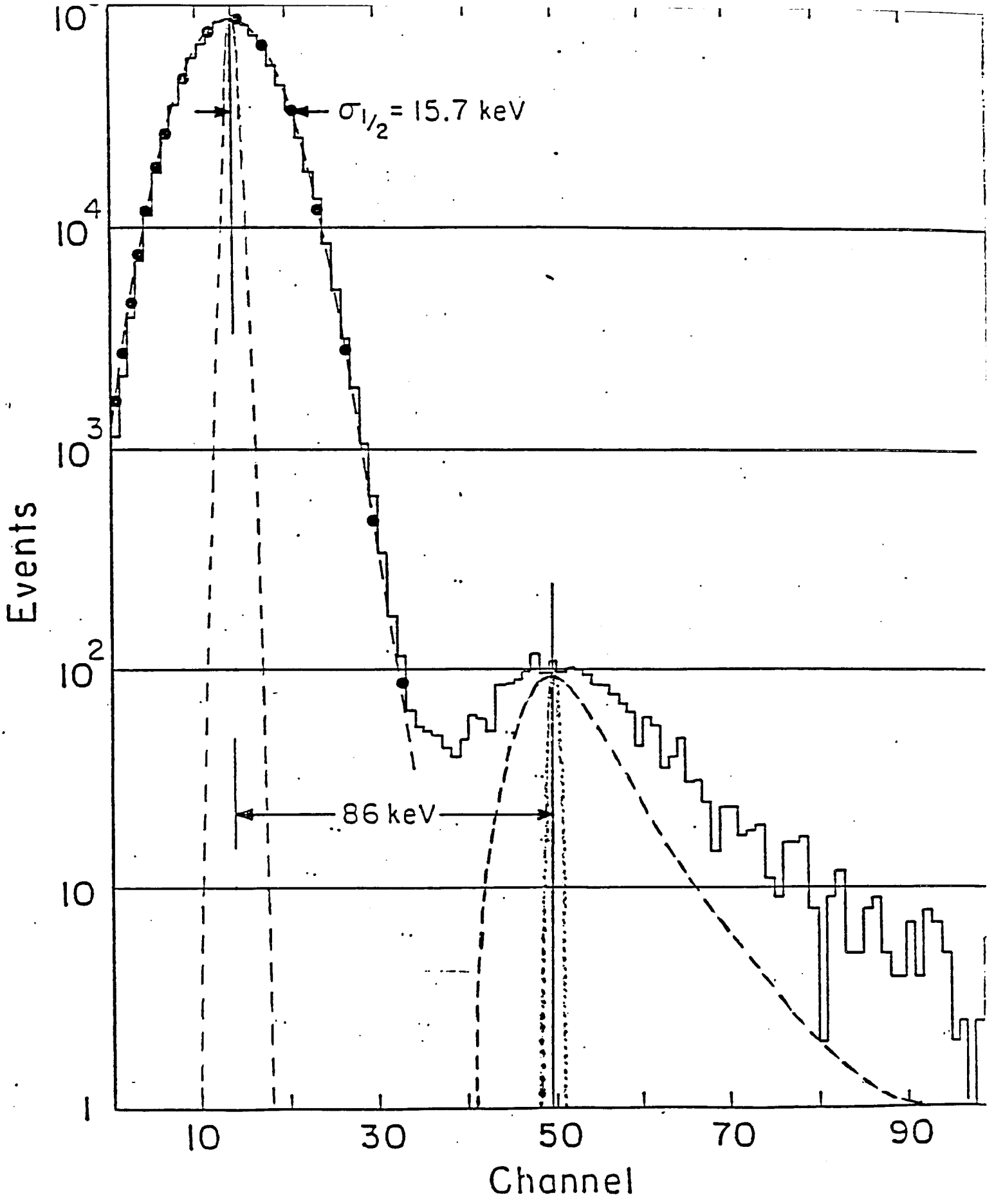

Figure III-3: A histogram of the integrated charge recorded from one channel of the SMD every time an electron went through the scintillator telescope.

important[16]. The dashed curve at the right is a schematic drawing of such a distribution. Here we only want to look at its qualitative features. The width is much broader than the expected statistical error and there is a tail due to the δ-rays.

This is the curve one would expect if the amplifiers and the ADC were perfect and one was looking only at signals from mips. However, all that the triggering scheme discussed above guarantees is that an electron went somewhere through the scintillation counter telescope. The ratio of the areas of one strip on the SMD and that of the scintillators was 2.5×10^{-3}. This is the probability, per trigger pulse, that a particle went through any given strip of the SMD. The peak on the left in Figure III-3 is the histogram of pulse heights observed for a trigger in which a particle did not go through this particular strip. The dashed curve within this peak is obtained by leaving the input to the ADC open and integrating for an arbitrary sequence of triggers. This is called the pedestal and is due to the reference current source that is present in ADC circuits and is used to define the zero of any scale. Hence at the outset we expect that the above scheme of testing should provide us with the two dashed curves of Figure III-3. It is seen, however, that both the observed peaks are considerably broader than the dashed ones. This broadening is due to electronic noise. The two dashed curves have to be folded with the noise spectrum in order to explain the experimental data. As is apparent, successful detection of mips depends on the ability to discriminate between the two peaks. A signal to noise (S/N) ratio is defined as the ratio of the difference between the two peaks and the half width at half maximum (HWHM) of the noise-peak. As shown in Figure III-3 a Gaussian curve was fitted to the noise and when calibrated it yielded a HWHM of 15.7 KeV or 4360 electrons. This is equivalent to a S/N ratio of 5.5. In the next section we look into the physics behind the noise and discuss ways of reducing it.

C. SOURCES OF NOISE GENERATION

Noise in electronics is broadly defined as any undesired signal that is present in the circuitry. As we will see in this section, it can be understood in statistical terms and in most, cases it can be evaluated. Noise sources are random in nature and will usually contain a large number of frequency components. In order to describe them we need to define average quantities. The formal introduction to random sources can be found in many text-books on this subject[25, 26, 27]. Here we will use the definitions needed for our analysis. The time average of a noise source v(t) over an interval T is defined in the usual way in eqn. (III-1).

$$\overline{v(t)} = \frac{1}{T}\int_0^T v(t)\,dt \qquad \text{III.1}$$

Fourier transforms for random sources are not defined. Instead, an *auto-correlation* function $R(\tau)$ and its Fourier transform $S(\omega)$ are defined as,

$$R(\tau) = \lim_{T\to\infty} \frac{1}{2T}\int_{-T}^{T} v(t)\,v(t+\tau)\,dt \qquad \text{III.2}$$

$$S(\omega) = \int_{-\infty}^{\infty} R(\tau)\,e^{-i\omega\tau}\,d\tau \qquad \text{III.3}$$

$$R(\tau) = \frac{1}{2\pi}\int_{-\infty}^{\infty} S(\omega)\,e^{i\omega\tau}\,d\omega \qquad \text{III.4}$$

$S(\omega)$ is called the spectral density of the random signal. From equation (III-4) the mean square of a random signal can be defined as R(0) as in equation (III-5). Equation (III-6) is called Parseval's theorem which states that the mean square of a random signal is the area under the spectral density.

$$\overline{v^2(t)} = R(0) = \lim_{T\to\infty} \frac{1}{2T}\int_{-T}^{T} v^2(t)\,dt \qquad \text{III.5}$$

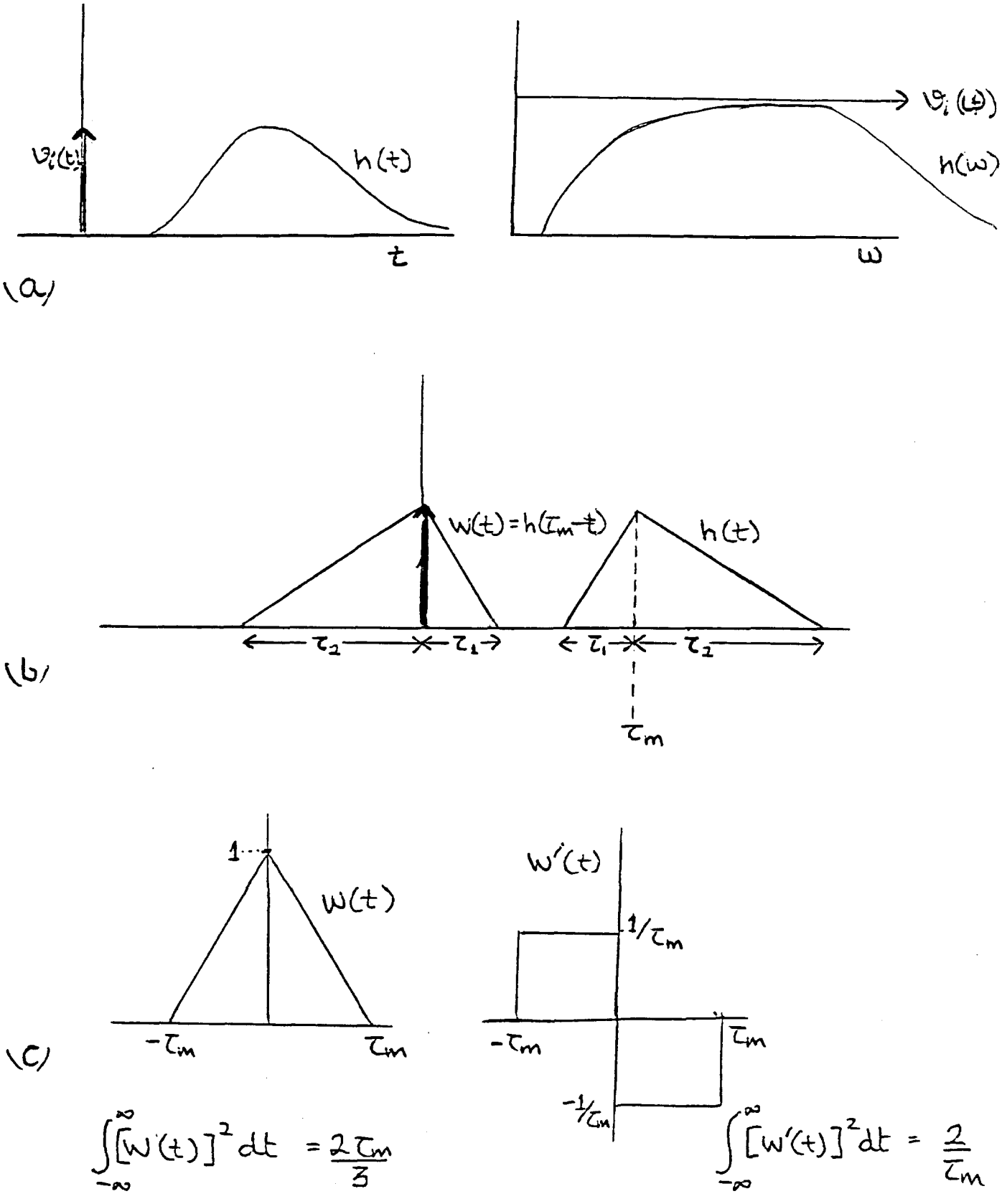

Figure III-4: (a)The relationship between the impulse response and the transfer function. (b) The weighting function is the mirror image of the impulse response. (c) A simple weighting function and its integrals for noise analysis.

$$\overline{v^2(t)} = \int_{-\infty}^{\infty} S(\omega)\, d\omega$$

$$\int_0^{\infty} S_p(\omega) = \frac{\overline{v^2(t)}}{2} \qquad \text{III . 6}$$

If this noise source was a voltage or a current source feeding into a 1 Ω resistor, $S(\omega)$ will be the power spectral density.

BAND-WIDTH LIMITED NOISE

All the integrals defined above usually do not converge. This does not matter from a practical point of view because all measurements are in some finite time-interval or band-width. Here we study the effect of frequency dependent circuits on noise. The impulse response, h(t), is the output of a circuit when an impulse is fed into its input. This is a useful function because any signal can be treated as a series of impulses with varying amplitudes. In effect, h(t) is the Fourier transform of the transfer function of a circuit. These are defined in equations (III-7) and shown schematically in Figure III-4(a). If we want to find the output v_o of a circuit for an input v_i, we have to convolute the input with the impulse response. The convolution integral is defined in equation (III-8). From this we can see that the response of a circuit to a δ-function input $v_i = \delta(t)$ is h(t).

$$h(t) = \frac{1}{2\pi} \int_{-\infty}^{\infty} h(\omega)\, e^{i\omega t}\, d\omega$$

$$h(\omega) = \int_{-\infty}^{\infty} h(t)\, e^{-i\omega t}\, dt \qquad \text{III . 7}$$

$$v_o(t) = \int_{-\infty}^{\infty} v_i(t_1)\, h(t - t_1)\, dt_1 \qquad \text{III . 8}$$

From equations (III-7) and (III-8) we get equation (III-9) which states that a

convolution in time-domain is equivalent to a product in frequency-domain. From equations (III-3) and (III-9) we can see that the spectral density output can be related to the input spectral density by multiplying with the transfer function squared as in equation (III-10)

$$v_o(\omega) = h(\omega)\, v_i(\omega) \qquad \text{III.9}$$

$$S_o(\omega) = S_i(\omega)\, |h(\omega)|^2 \qquad \text{III.10}$$

The measurement of a signal is done at a point in time that is later than the time of origin. For obvious convenience we will always measure the signal at the time where it peaks. A weighting function w(t) is defined as $h(\tau_m - t)$, where τ_m is the peaking time. From this definition, the peak voltage $v_o(\tau_m)$ is given by equation (III-11).

$$v_o(\tau_m) = \int_{-\infty}^{\infty} v_i(t)\, h(\tau_m - t)\, dt \qquad \text{III.11}$$

$$= \int_{-\infty}^{\infty} v_i(t)\, w(t)\, dt$$

Figure III-4(b) shows that w(t) is a mirror image of h(t) with a time shift. This picture brings out the importance of the function w(t). The peak of the weighting function coincides in time with the impulse. The signal from an SMD can be considered to be $Q_o \delta(t)$ where Q_o is the total charge in the signal. The integral in equation (III-11) then gives us the peak current at the output. If we normalize w(t) to have a height of unity, the peak at the output is calibrated to be Q_o. Now we can use w(t) to evaluate the contribution of random noise impulses as well. The result will directly be in terms of noise charge. Before we evaluate this charge we will discuss the physical origins of noise.

D. PHYSICAL NOISE MECHANISMS

In a typical PIN diode detector circuit the sources of noise are, (i) the diode itself, (ii) external resistive elements, and (iii) the input stage of the preamp. Below we will discuss the fundamental noise generating mechanisms, and their contribution to these three sources.

SHOT NOISE

This source of noise, associated with direct currents, is a consequence of the fact that currents consist of discrete carriers, namely electrons. If we observe such a current flow across a region Δx, we will see a series of current pulses with a width w, equal to the transit time of an electron with a drift velocity v_e such that $w = \Delta x/v_e$. The height of the pulses will be e/w so that the area under any pulse will be equal to the electron charge. These pulses will be statistically uncorrelated and now our direct current appears to be a superposition of a large number of fast pulses. If on the average there are $\bar{n}$ pulses per second, the mean square current per second is $\bar{n}e^2$. The dc current is given by, $I_o = \bar{n}e$. Hence the spectral density is given by, $S(\omega) = eI_o$. The physical power spectral density (psd) is defined only in terms of positive frequecies, and is equal to twice of $S(\omega)$. The simple argument can be made more rigourous by considering square impulses instead of δ-functions. From equation(III-10) this is equivalent to a multiplication by the transfer function squared of a square filter. This is done in equation (III-12)[28].

$$S_p(\omega) = eI_o \frac{\sin^2(\pi w f)}{(\pi w f)^2} \qquad \text{III.12}$$

The width Δx is of the order of 1 μm for p-n junctions and 1/w is in the GHz range. Hence we can consider the shot noise to be *white*, that is it has the same rms strength in any frequency interval. Figure III-5(a) shows the noise equivalent circuit for the diode. The leakage current in the diode is a source of shot noise and is shown as a current source in parallel with the diode capacitance and resistance. The asterisk in the symbol represents the random nature of the source.

THERMAL NOISE

The random thermal fluctuations of the electrons in a resistive element create an emf at its terminals. Being random in nature this emf is a source of noise. We expect these fluctuations to be of order kT for a system in thermal equilibrium at a temperature T. This is the so called Nyquist or Johnson noise. The spectral density is also white, and is given by[28]

$$\frac{d}{df}\overline{v_n^2(t)} = S_p(\omega) = \frac{1}{2}\cdot\frac{4kT}{R} \qquad \text{III.13}$$

where R is the resistance, T the temperature, k the Boltzman constant, and v_n the rms noise voltage. The equivalent circuit for a resistor can also be considered as a current source in parallel with a noiseless resistor in Figure III-5(b).

1/F NOISE

The exact mechanism for this source of noise, sometimes called flicker noise, is not understood. Nevertheless, it is observed in silicon devices and is sometimes attributed[29] to surface states at the oxide interface. As the name suggests the spectral density has a 1/f dependence,

$$S_p(\omega) = A/f \qquad \text{III.14}$$

where A is a parametrized constant. Since we have a fast device, the associated electronics has to have a high band width and at the frequencies of interest (>1 MHz) the 1/f noise is not very important. This takes care of the noise sources other than the preamp.

AMPLIFIER NOISE

For the purpose of noise analysis an amplifier can be represented by a noise- free black box of gain A_v and a pair of noise generators at the input, as shown in figure III-6. These sources can be understood by looking at the input stage transistor in the preamp. The strength of these sources can be readily calculated for bipolar junction

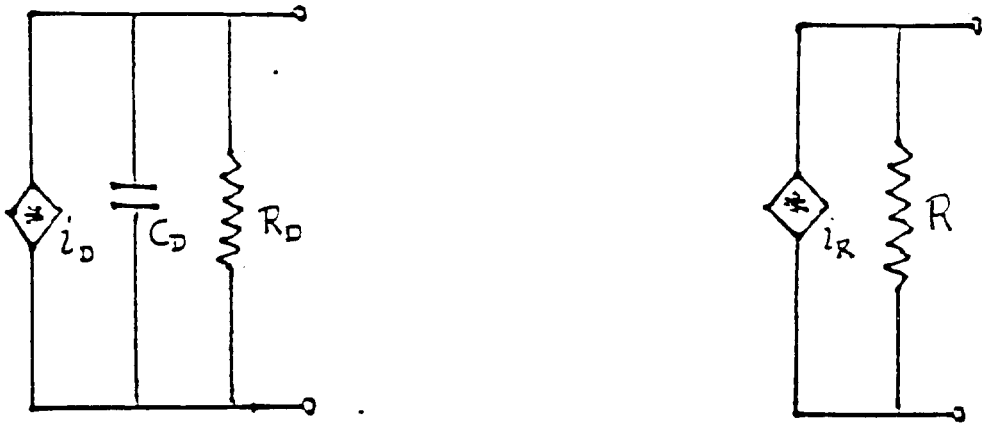

Figure III-5: The noise equivalent circuits for shot noise(a) and thermal noise (b).

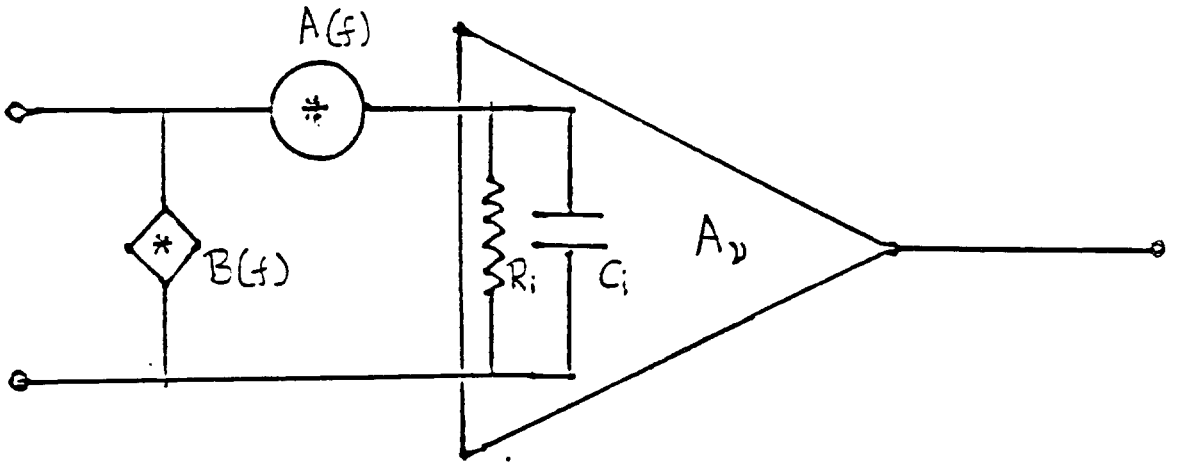

Figure III-6: Noise equivalent circuit for an amplifier.

transistors(BJT's). As an example, below we give them for a common emitter amplifier circuit :

$$A(f) = \frac{1}{2} 4kT \left(R_{BB'} + \frac{1}{2 g_{m,B}} \right) \qquad \text{III.15}$$

$$B(f) = \frac{1}{2} . 2eI_B \qquad \text{III.16}$$

The parallel noise source, B(f), is due to the shot noise in the input dc current, which in this case is the base current, I_B. The first term in the series noise source, A(f), is due to the the thermal noise in the base spreading resistance, $R_{BB'}$, of the transistor. The base spreading resistance is obtained by considering the actual current path through the base region. Due to different current densities along the junction surface the resistance is distributed and the effective resistance is less than the bulk base resistance, R_B. This becomes important for low bias currents. A simple calculation[30] shows that $R_{BB'} = R_B/3$ is a good approximation.

The term involving g_m needs some explanation. The quiescent level current at the output of the transistor is a source of shot noise. The series noise voltage source is equivalent to this noise when referred to the input of the preamp. For a BJT the diode equation under forward bias for the collector current is given by[31]:

$$I_C = I_{CK} e^{eV_{BE}/kT}$$

$$g_{m,B} = \frac{\partial I_C}{\partial V_{BE}} = \frac{e}{kT} I_C \qquad \text{III.17}$$

The Thevenin equivalent of the resulting shot noise current source can be written in terms of g_m as following :

$$S_p(\omega) = 2eI_C = \frac{2kT}{g_{m,B}} \qquad \text{III.18}$$

The strength of the noise sources for a junction field effect transistor(JFET) can also be given in a similar way[32],

$$A(f) = \frac{1}{2} . 4kT \frac{0.7}{g_{m,F}}$$

$$B(f) = \frac{1}{2} . 2eI_G . \qquad \text{III.19}$$

where I_G is the gate leakage current and $g_{m.F}$ the transconductance which relates the drain current to gate voltage.

EQUIVALENT NOISE CHARGE

Equivalent noise charge (ENC) is a useful parameter as it enables us to determine the S/N ratio. It is evaluated by referring all noise sources to the signal-source. The parallel noise source is already referred to the signal and we can represent noise as random impulses. The contribution from the series noise source can be evaluated at the signal source by taking the input capacitance into account. The voltage impulses $v_n \delta(t)$ are equivalent to current impulses $i_n(t) = v_n \delta(t) / Z_i$, where Z_i is the input impedance. In equation (III-20) we show that this can be written as a source of impulses and doublets, $\delta'(t)$.

$$i_n(t) = \vartheta_n \, \delta(t) \left[\frac{1}{R_i} + j\omega C_i \right]$$

$$= \vartheta_n C_i \left[\frac{\delta(t)}{R_i C_i} + \delta'(t) \right] \qquad \text{III.20}$$

The equivalent noise charge (ENC) is given by the output response of these sources. For white noise sources the ENC is given by[33],

$$(ENC)^2 = A(f) \left[\int_{-\infty}^{\infty} \left\{ \frac{w^2(t)}{R_i C_i} + w'(t)^2 \right\} dt \right] + B(f) \int_{-\infty}^{\infty} w^2(t)\, dt \qquad \text{III.21}$$

where C_d and C_i are the detector and input capacitances and A(f) and B(f) are the sums of all parallel and series noise currents respectively.

E. NOISE EVALUATION AND CHOICE OF PREAMP

Having defined all the sources of noise in a systematic fashion, now we can evaluate the noise level of any given circuit. We would like to introduce another circuit for a preamplifier and compare its noise level with that of the circuit in Figure III-2(a). As shown in Figure III-7(a) this circuit has a JFET as the input transistor which feeds into a common emitter amplifier and is itself fed back through an RC

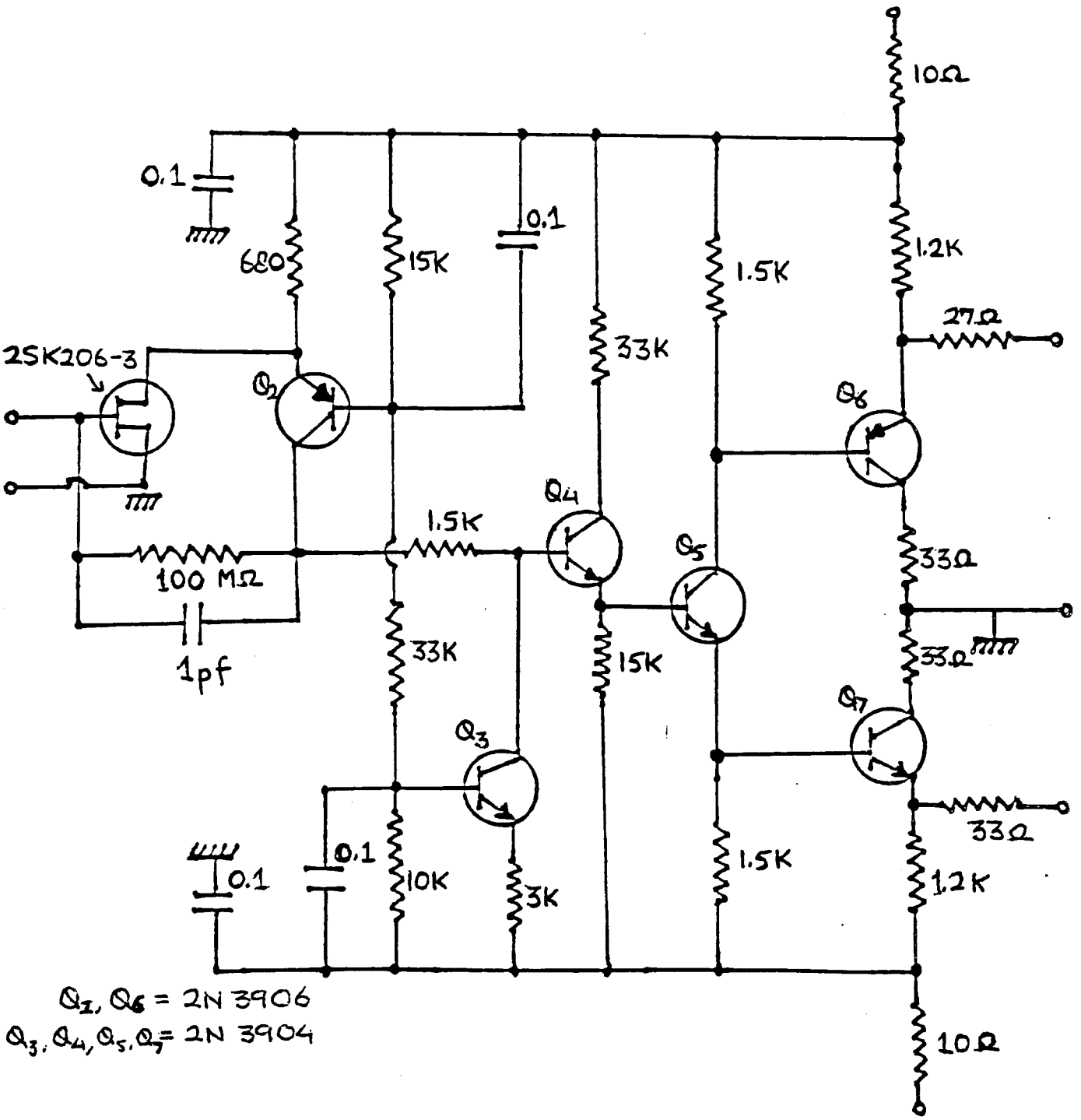

Figure III-7: The circuit for a charge sensitive preamp using a JFET at the input.

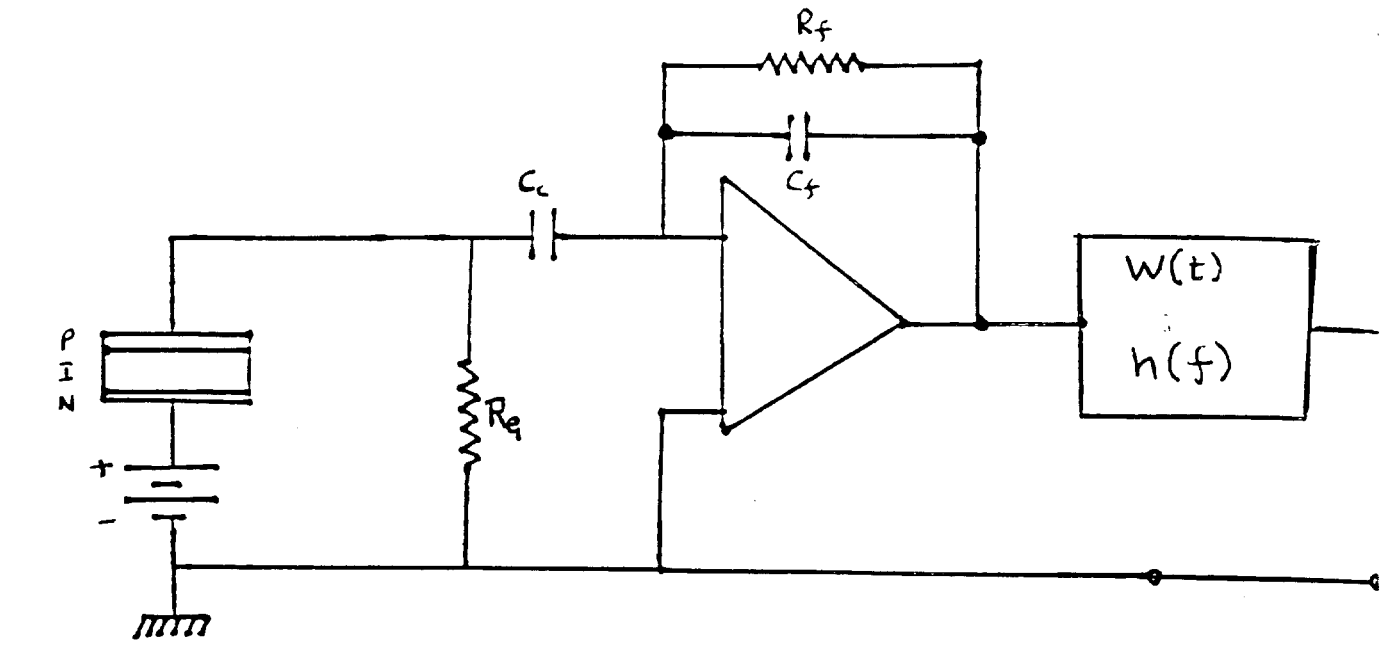

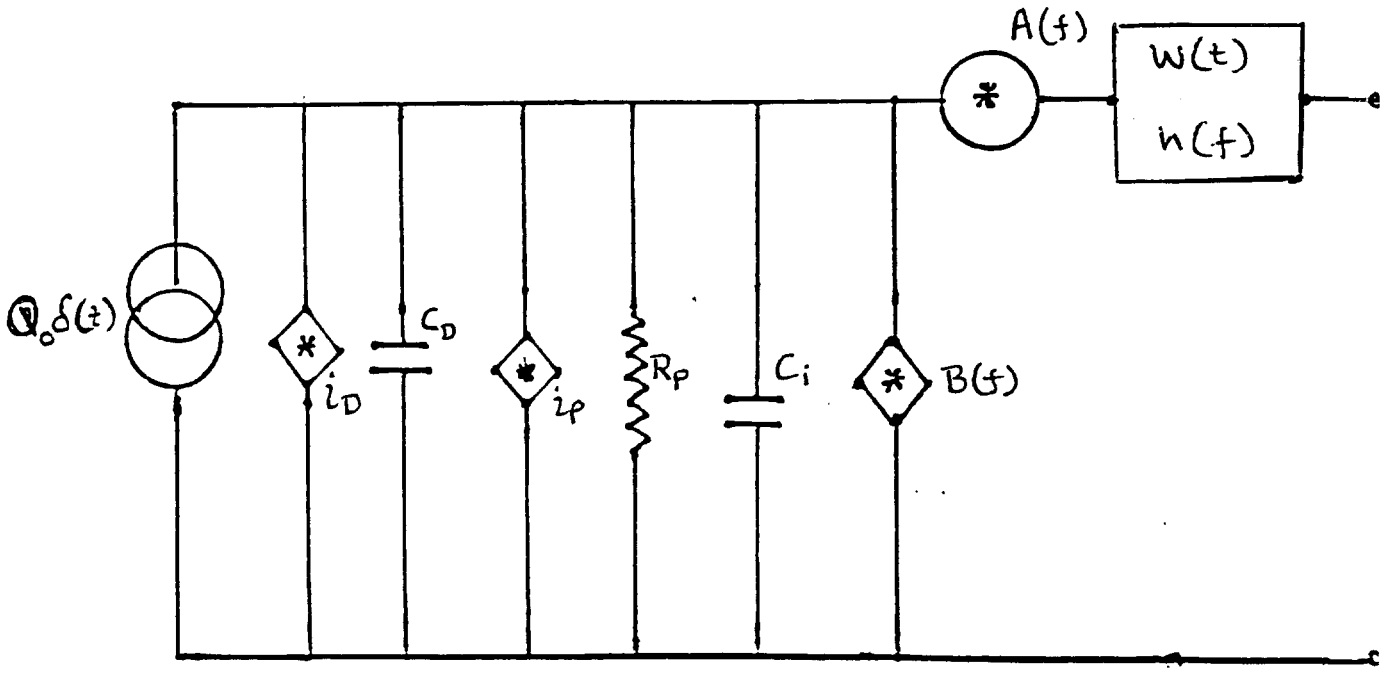

$$\frac{1}{R_P} = \frac{1}{R_f} + \frac{1}{R_{e_1}} + \frac{1}{R_D} \qquad i_p^2 = \frac{4kT}{R_p}$$

Figure III-8: The equivalent noise circuit for a PIN diode detector.

circuit. This is followed by a cascaded amplifier and a driver circuit at the output. The design of the input stage makes it a charge sensitive amplifier in the following way. The current impulse from the detector charges up the feed-back capacitor and the output of the common emitter circuit establishes a voltage v=q/c. The charge now leaks through the feed-back resistor at a rate given by the RC time constant and the output follows the voltage faithfully. Hence, we have a circuit that produces a voltage at its output that is proportional to the current impulse, or the charge, at the input.

Figure III-8(a) shows a typical channel of the PIN detector circuit. The resistor R_G and the capacitor C_c are used to ac couple the preamp to the diode. The shaping circuit is shown as a black-box filter with a gain of unity. Figure III-8(b) gives a detailed equivalent circuit for the PIN diode detector circuit. where we have included all the noise sources discussed above. R_p is the sum of all the resistors in parallel. i_p is the shot noise source associated with it. i_D is the detector shot noise source in parallel with the detector capacitance C_D. C_i is the stray capacitance at the input. The signal from the diode is shown as a current impulse source $Q_o\delta(t)$.

Below we present the contributions from each term in the ENC for the the preamplifiers in Figures III-2(a) and III-7. In order to simplify the analysis we can choose a triangular weighting function as shown in Figure III-4(c). The integrals are simple to evaluate and the results are shown in the figure. Even though we did not have a perfectly triangular shaping for the pulse we can assume τ_m to be the rise time in order to get a good estimate. Folding in the values of the integrals in equations (III-20) and (III-21) we get equation (III-22) for the ENC. The second term in the series noise can be neglected because the input time constant is much longer than the filter time constant. The contributions to the ENC are tabulated in Figure III-9.

$$(ENC)^2 = A(f)\, C_i^2 \left[\frac{2}{\tau_m} + \frac{2\tau_m}{3R_iC_i}\right] + B(f)\frac{2\tau_m}{3} \qquad \text{III.22}$$

The first thing we notice is that our estimate of 4725 electrons noise for the current amplifier is in good agreement with the measured value of 4360 electrons, considering the approximations in our treatment. The biggest contribution is from the

ENC for various terms.	CURRENT AMP WITH BJT $\tau_m \sim 6ns$ $I'_E \sim 0.86mA$ $g_{m,b} \simeq g_{m,e} \sim 25 mA/V$	CHARGE AMP WITH JFET $\tau_m \sim 20ns$ $R_f \sim 100M\Omega$ $g_m \sim 15mA/V$ @$I_{DS} \tilde{} 3mA$ $I_e < 10nA$
(i) $A_f \frac{(C_D + C_i)^2}{\tau_m}$ $C_D + C_i \sim 25pF$	$A(f) = 2kT/g_m$ 913 e^-	$A(f) = 2.8\ RT/g_m$ 955 e^-
(ii) $B(f) \frac{\tau_m}{3}$	$B(f) = 2eI_E$ 4636 e^-	$B(f) = 2eI_e$ 29 e^-
(iii) $2eI_D \frac{\tau_m}{3}$ $I_D \sim 10nA$	16 e^-	29 e^-
(iv) $\frac{4kT\tau_m}{R_f 3}$	———	7 e^-
TOTALS (ADDED IN QUADRATURE)	4725 e^-	960 e^-

Figure III-9:

input current I_E. This can be reduced by using a common emitter circuit but there is a corresponding increase due to the thermal noise in the base-spreading resistance. Secondly, the charge sensitive preamp promises a much better performance with a noise

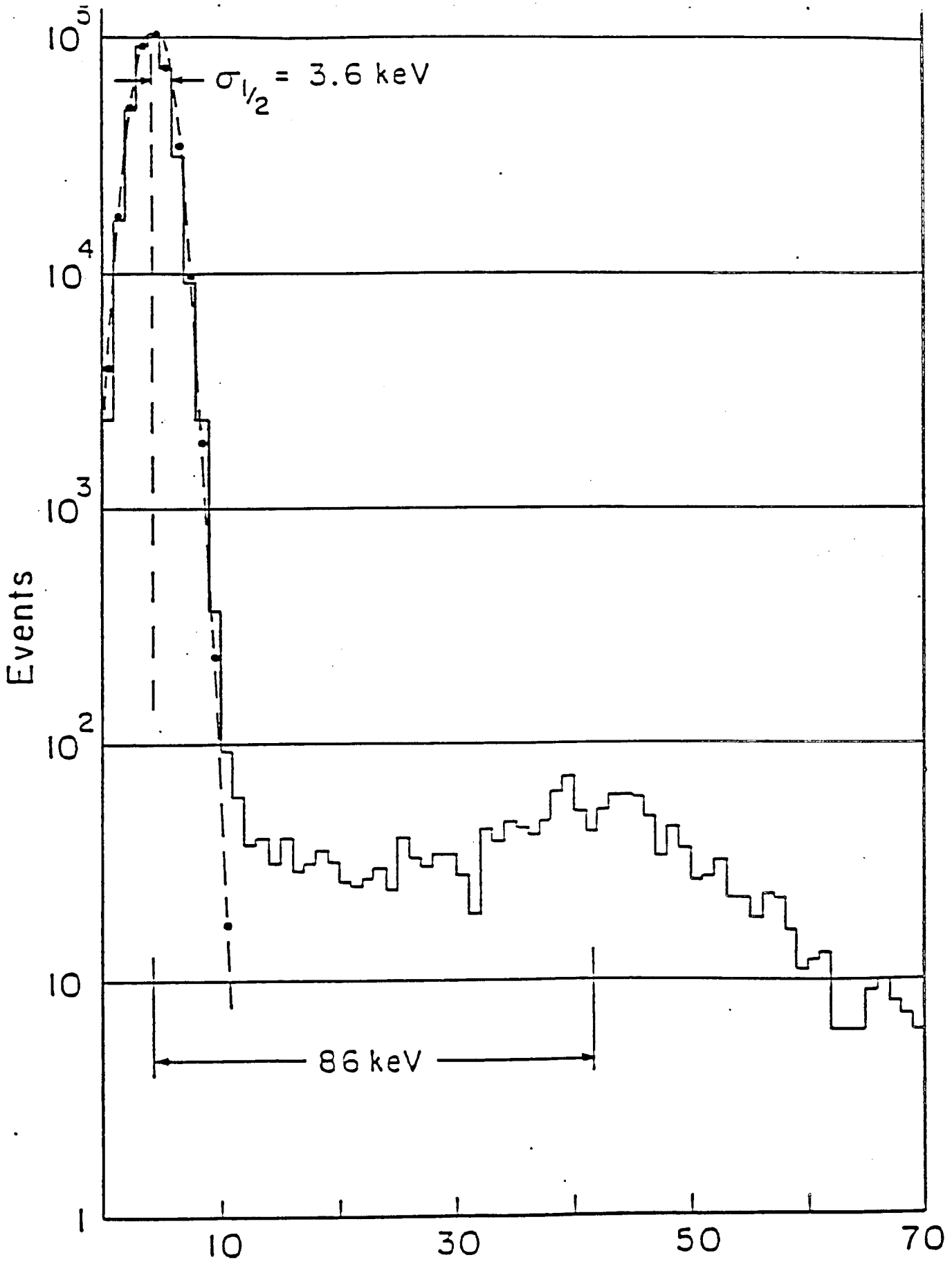

Figure III-9: The ADC curve for the preamp of figure III-7.

of 950 electrons. This is confirmed by the ADC curve in Figure III-10 which has a noise level of 1000 electrons. This example shows that a charge sensitive preamp with an FET at the front end is the better choice for our application. The current amplifier would be a better choice if the main criterion was speed.

As we can see, the biggest contribution to noise in this case comes from the input capacitance term. Figure III-11 shows the dependence of ENC on the input capacitance for the two preamps. The intercept is the contribution from other noise sources. For the case of the JFET there is a contribution of nearly 10 pF from the gate to source capacitance which can not be eliminated. The rest of the capacitance comes from the strays at the input. A copper trace on G-10 has a capacitance of nearly 1pF/cm. Hence in the interest of reducing the noise the trace length to a preamp should be minimized. This in turn requires that, in order to bring the preamps as close to the wafer as possible, the preamp's physical size should be miniaturized. In our present design, for a typical channel, the capacitance can not be made much smaller than the present value of nearly 30 - 40 pF, which comes from the total trace length of 30 - 40 cm. For the wafers that have fewer channels it is conceivable that a design using shorter trace lengths be used, but it is not in the interest of standardizing the design of X-Y modules. In any case, the requirement for a miniature size calls for the use of commercial units because industrial houses posses the necessary technology for such manufacturing.

From equation (III-23) we can see that the series noise depends inversely on the shaping time τ_m while the parallel noise depends on it directly. Hence there exists a unique value of τ_m at which the ENC is a minimum. This can be obtained by differentiating the expression for ENC with respect to τ_m. This suggests that the preamp be followed by a shaping circuit designed to put out a pulse of base width equal to twice the optimum τ_m. At this point we would like to mention the cost factor involved in the design of our amplification scheme. We would like to argue that a sophisticated shaping circuit is an unnecessary expense for our needs because a sufficiently high signal to noise ratio was achieved by using only passive filters. This is demonstrated in the next section.

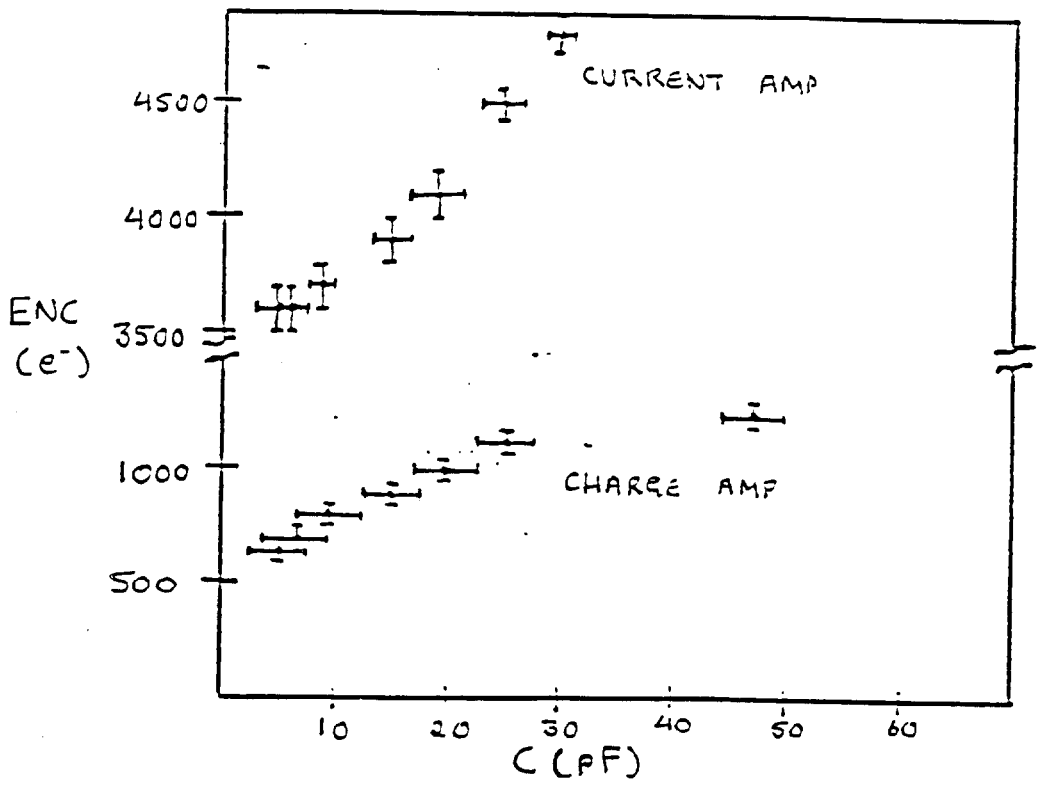

Figure III-11: ENC versus capacitance for the two preamps.

F. TESTS WITH A RU^{106} SOURCE

In order to select the most suitable preamp for our purposes we tested all the commercially available units. The criteria were low noise and small physical size. It was not possible to do all the tests in a beam, so a Ru^{106} beta source was used. It has a decay chain in which Ru^{106} goes to Ro^{106} by emitting a gamma-ray photon. Ro^{106} is short lived and decays by emitting an electron. The electron has an energy of 3.5 MeV implying an E/m of 7 which is sufficient to make it minimum ionizing. We were able to acquire a 10 μCurie source deposited in a spot size of 1 mm. This was quite adequate for doing our tests on noise except for one problem. A 3.4 MeV electron has a large cross-section for large angle scattering making it impossible to collimate them. Hence we could not ensure that they were restricted to one strip in their passage through the wafer. This resulted in a large spectrum of pulse heights coming out of any given strip which in turn broadened the signal peak in ADC curves. One needs a good definition of the peak in order to calibrate the width of the noise.

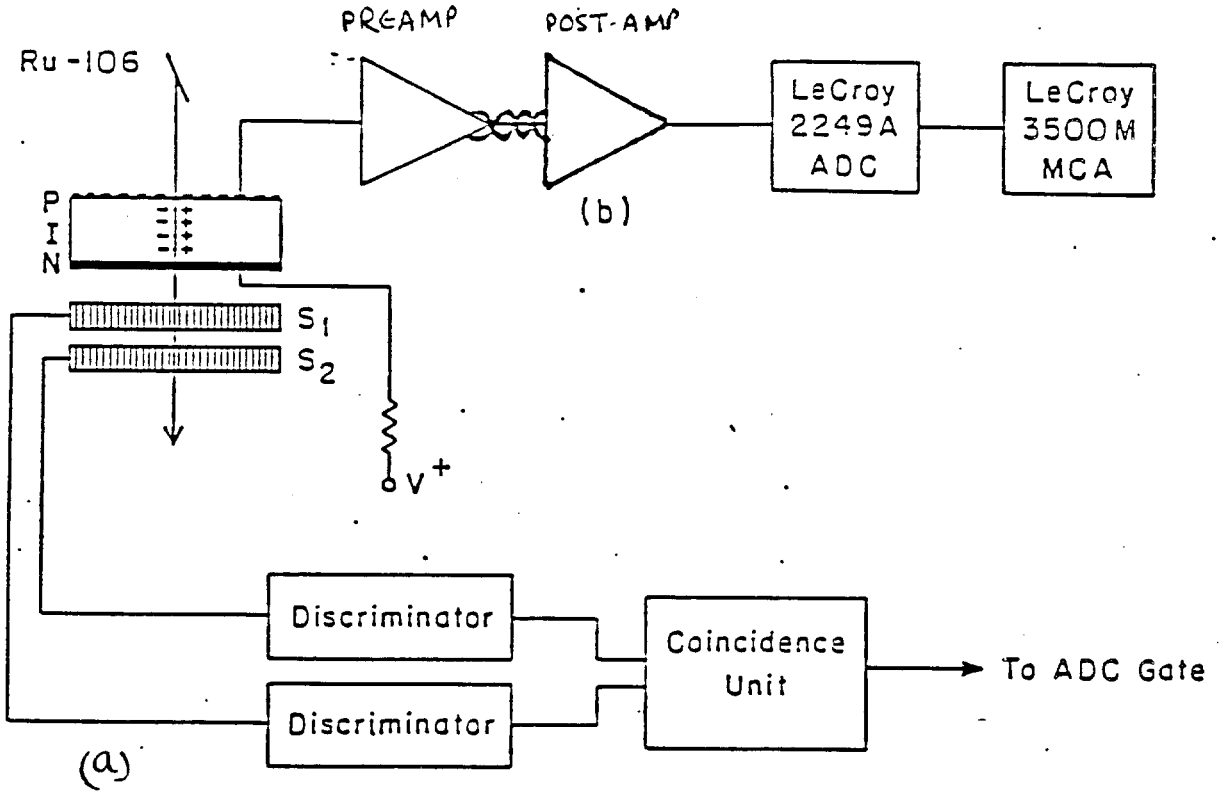

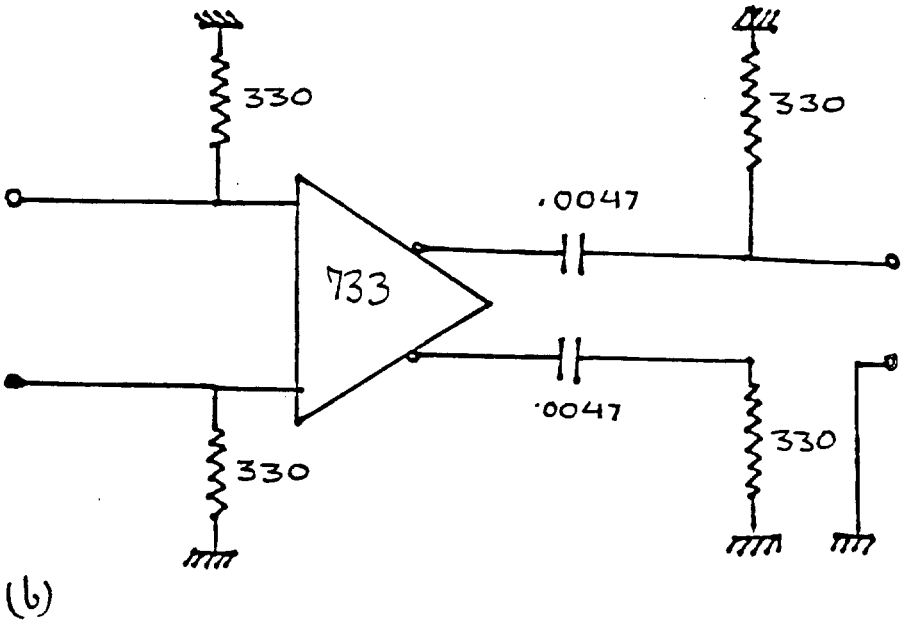

Figure III-11: The experimental set-up for testing preamps using a Ru^{106} source on the SMD (a). A simplified post-amplifier circuit without any shaping (b).

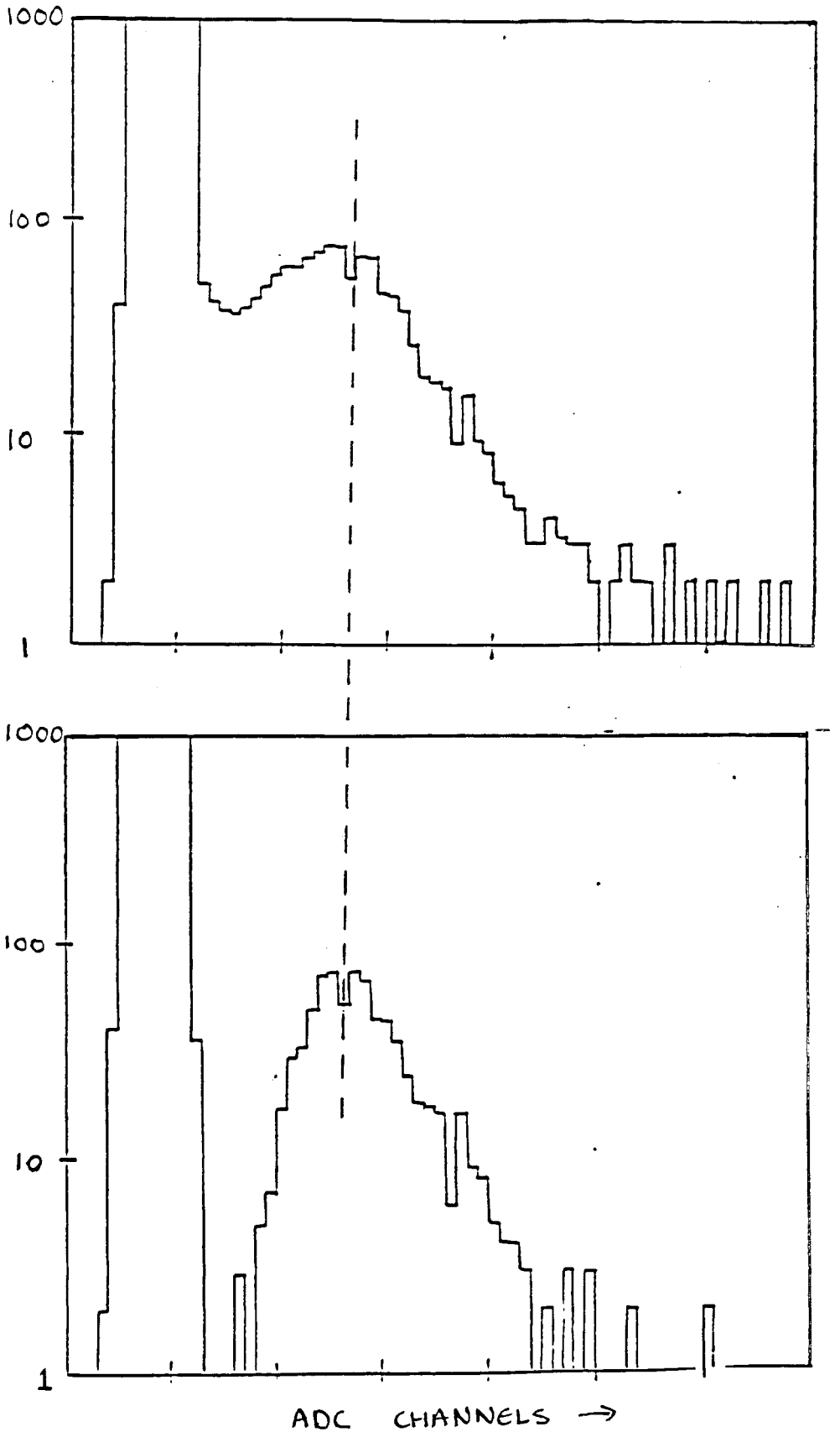

Figure III-12: The ADC curves taken with (b) and without (a) the cut imposed to remove valley events.

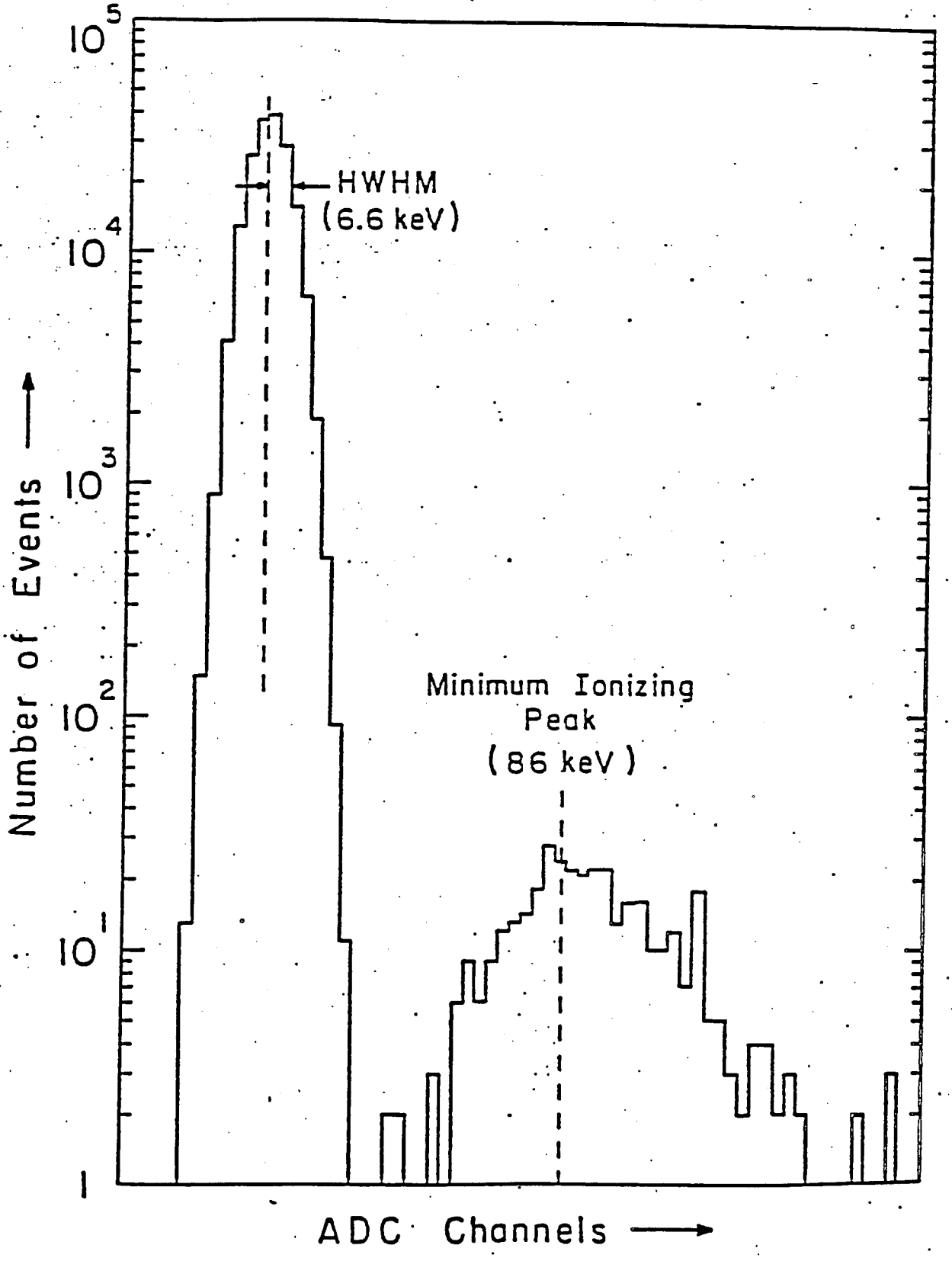

Figure III-13: ADC curve for the HQV-810 preamp

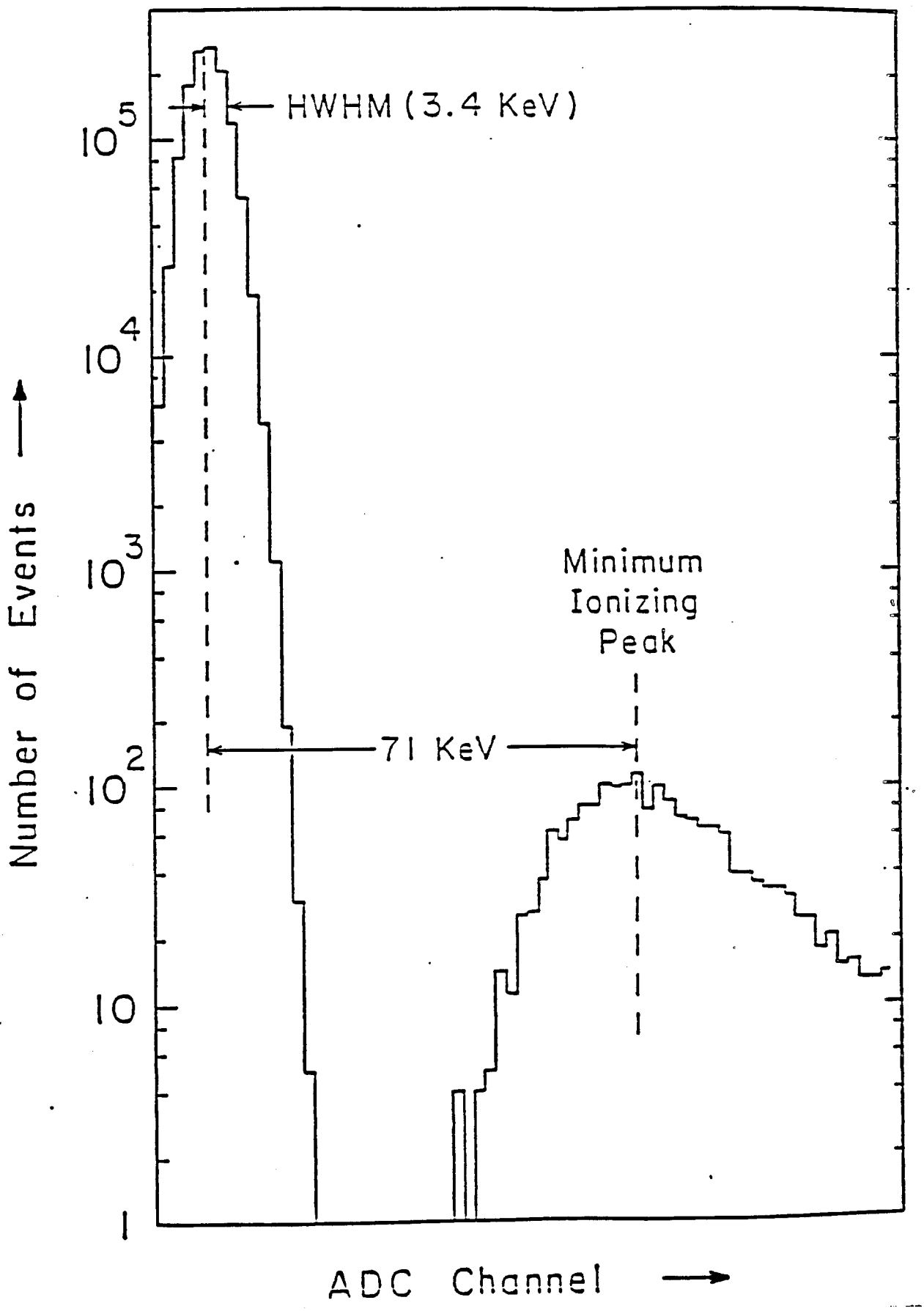

Figure III-14: ADC curve for the Rel Labs IO-323-C preamp

Figure III-12(a) shows the experimental set-up for testing the electronics. The post-amplifier used here did not have pole-zero cancellation circuits because we intended to test feasibility of running with only a differentiator for the shaping. This is provided by the 4.7 nF capacitor and the 330 Ω resistor. The simplified circuit is shown in Figure III-12(b). Figure III-13(a) shows a pulse height spectrum obtained using this set-up. On comparing it with the curve in Figure III-3 one can see that the signal peak is at the same location. This confirms the fact that these electrons are minimum ionizing. On the other hand, there is a larger population of pulse heights in between the two peaks. These are the signatures of electrons that went through the wafer at a large angle thereby dividing the signal strength among two or more strips. We will refer to them as 'valley' events in the ensuing. We tested this claim by introducing the following selection criteria. For every trigger produced by the scintillation counters all the channels being tested were digitized but if any two neighboring channels had a pulse height greater than some pre-selected 'cut' value the event was discarded. This criteria cleaned out the valley as shown in Figure III-13(b). As we can see there is a better definition of the signal peak now than in Figure III-13(a). The cut value used was equal to three times the HWHM of the noise peak. All the tests that followed and the ADC curve in Figure III-10 were done using this scheme.

Figures III-14 and III-15 show the ADC curves under similar conditions for two commercially available charge sensitive preamps that satisfied our criteria. The post amplifier used was the one shown in Figure III-7(b) which has no active shaping circuits. The LeCroy HQV-810 and the Rel Labs IO-323-C are both charge sensitive preamps with JFET's at the input. The former is an 8-channel device housed in a DIP while the latter is a single channel device in the form of a surface mounted hybrid circuit. On comparison it can be seen that the Rel Labs preamp provides the better noise level (950 electrons). Other considerations, such as the ease in replacing one channel versus eight if one of them were to fail and the ability to group channels according to their gains, clearly showed it to be the most suited. In addition, as claimed before, it provided a good enough S/N that it eliminated the need for a sophisticated filter.

CHAPTER IV.
READ-OUT ELECTRONICS

A. INTRODUCTION

In the previous chapter we described the design of the preamplification scheme. For the SMD system what we are interested in knowing is which strips were hit by a particle in a particular event. Digitizing a signal in an ADC and suppressing the channels that have a value below some threshold is one way of doing it. We take the alternate approach of discriminating the signal pulse and converting it to a logical pulse. The logical signal can then be filtered in order to suppress all the 'false' data. The event size is thereby reduced considerably to typically a few hundred 'true' signals. Electronic hardware for such a read-out system is manufactured by Nanometric Systems (Nano)[34] for PWC's. This system was chosen as a common read-out scheme for both the SMD's and the PWC's in E706, in order to standardize the required computer hardware and software. In this chapter we describe this system and present results on the successful interfacing of our preamps to it. Some other issues like grounding, shielding and cooling are also addressed.

B. TESTS ON THE NANO ELECTRONICS

Figure IV-1(a) shows the schematic circuit for one channel of Nano N-277, the first stage of the Nano system. It consists of a wide-band differential amplifier at the input followed by a discriminating circuit. The threshold level can be set with an external dc voltage such that 1V corresponds to one μA at the input. For signal strength of 24,000 electrons and a feedback capacitor of 1 pF the output of the preamps is 3.8 mV. The peak current of our signal pulse from the preamps is approximatately 3.8 mV/330 Ω = 11.5 μA into one input. The dynamic range of the amplifier is 0.5-20 μA which is quite sufficient for our signal strength. If we recall the

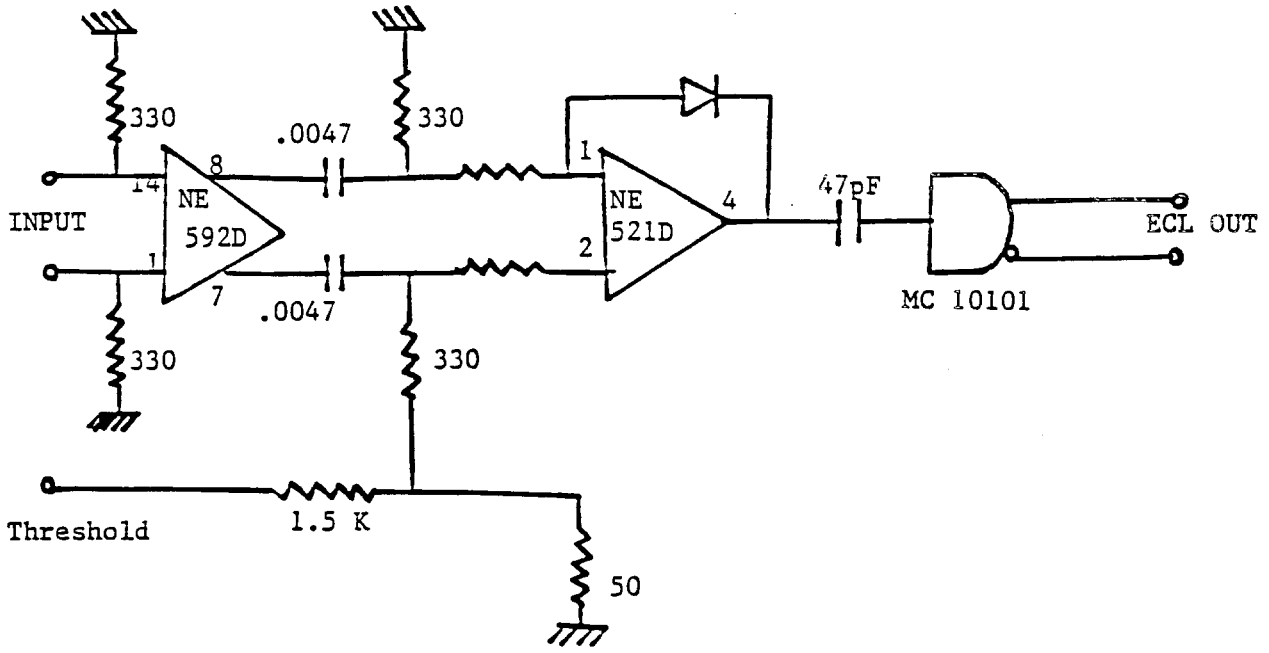

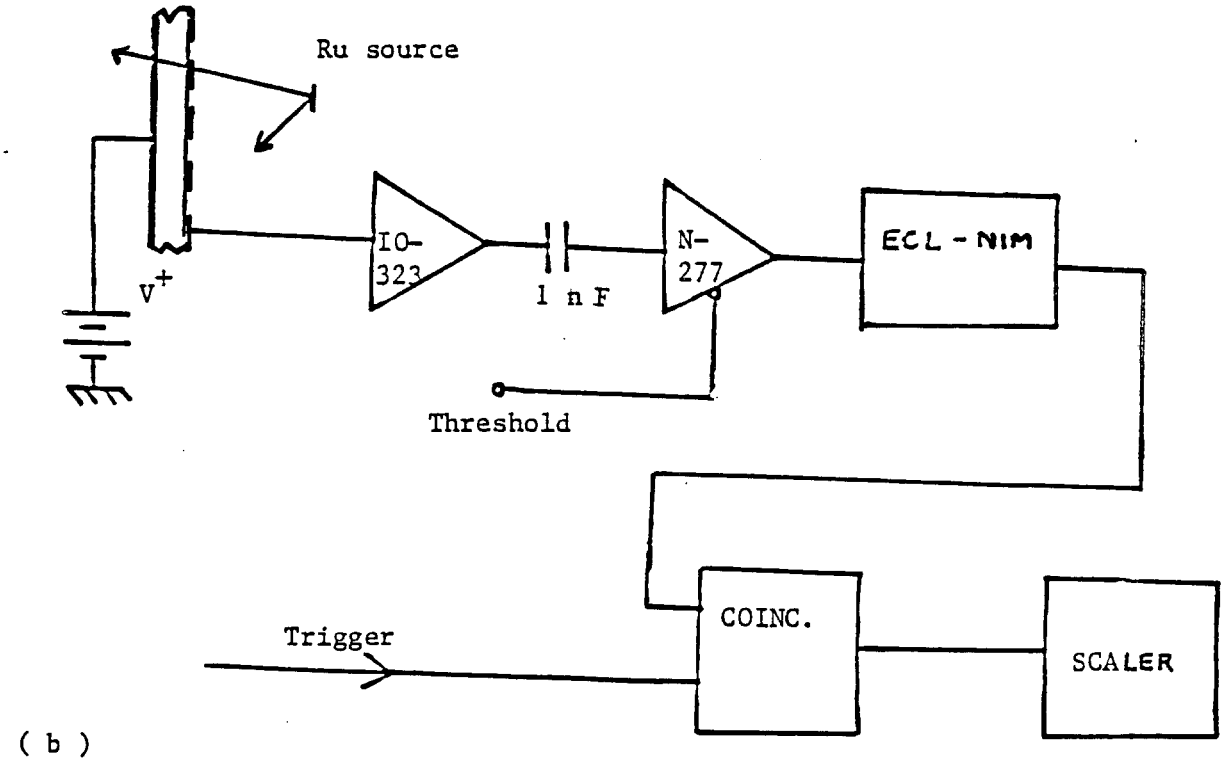

(b)

Figure IV-1: The schematic circuit of one channel of the Nano N-277 amplifier-discriminator (a) and a simple set-up for testing it for our needs (b).

simplified version of the post amplifier from the previous chapter we will notice that it imitates the front end of the Nano system. This was done deliberately in order to test the preamps under conditions in which they operate. Hence, at first glance the interfacing of the preamps to the Nano system does not pose any problems. The last stage in the N-277 circuit is an ECL driver. It sends a logical pulse of a width equal to the duration for which the signal stays over threshold up to a maximum of 45 ns. For a mip signal from the preamp this circuit should respond with a 45 ns ECL pulse.

Figure IV-1(b) shows a simple set-up for testing this electronics. The experiment involves counting ECL pulses coming out of the circuit for various settings of the threshold voltage. As before there is a trigger circuit involving scintillation counters that is not shown here. The trigger pulse is put in coincidence with the output of the Nano circuit and the resulting output pulses are scaled. A plot for such an experiment is shown in Figure IV-2. The curve can be understood in terms the curves shown in the previous chapter for the response of an ADC. The curve in Figure IV-2 corresponds to the area under and ADC curve. The rapid fall-off on the left is the noise spectrum. followed by a slowly falling region. This region is due to valley events discussed in section III.E. In the absence of such low pulse height events this region would have zero slope, thus giving us a plateau. The knee on the right and the subsequent fall-off is the integral of the minimum ionizing pulse height spectrum. The half point on the fall-off corresponds approximately to the peak. To get a measure on the knee of the noise curve we impose similar cuts as before to get rid of valley events. The percentage of gates for which there were two or more hits was measured at each threshold setting. The data points on each strip were then corrected by this fraction. The discrimination curve using this criteria is shown in Figure IV-3. The plateau region is now very well defined and is approximately 1.6 V wide.

This proves that the Rel Labs preamp and the Nano N-277 can provide us with a successful scheme for discriminating mips from noise. The system also provides us with a scheme for filtering and reading out a large number of channels. This will be described in section IV.E. At this stage we would like to describe our instrumentation scheme for the two stages of the electronics.

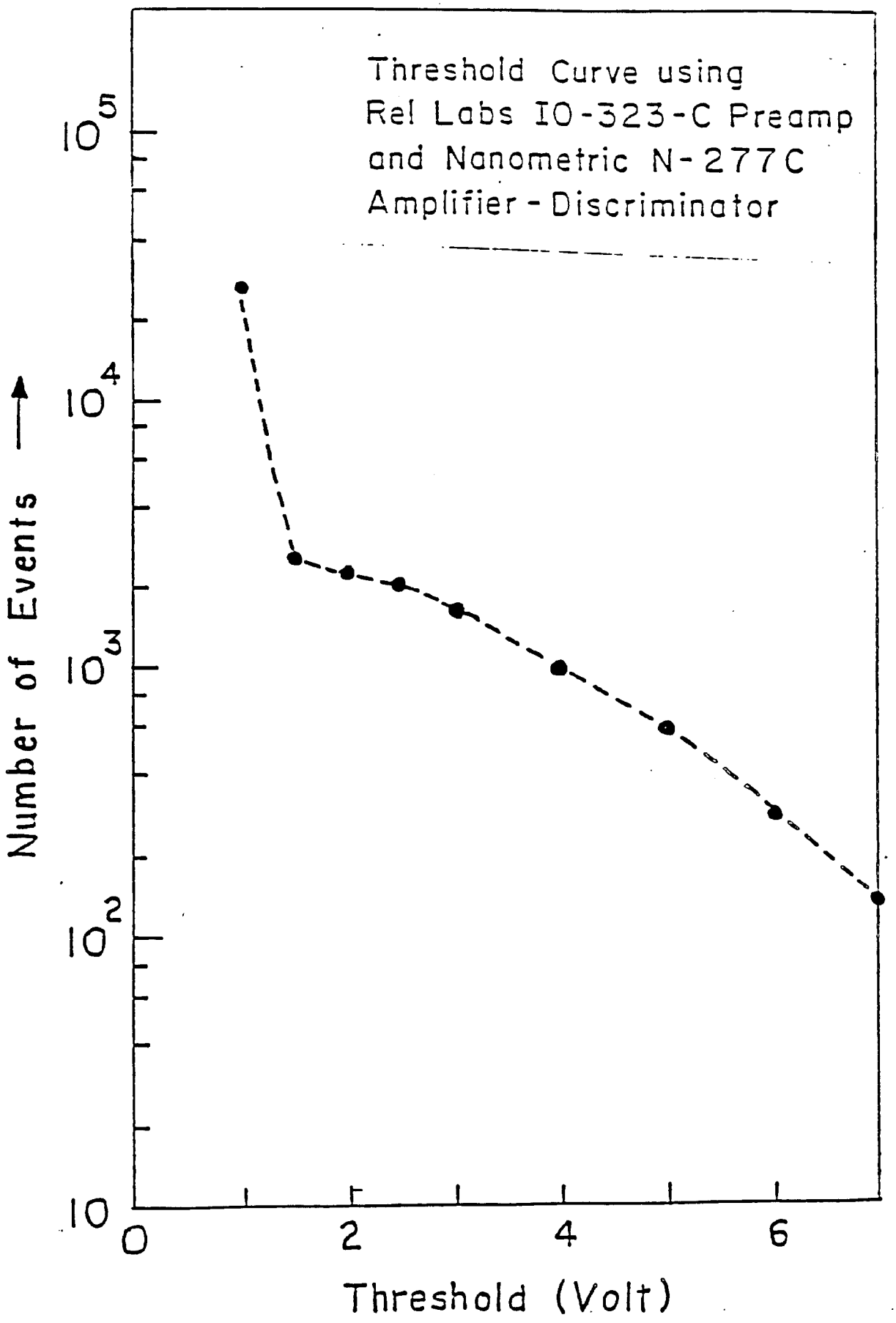

Figure IV-2: The discriminator curve obtained using the scheme in Figure IV-1(b).

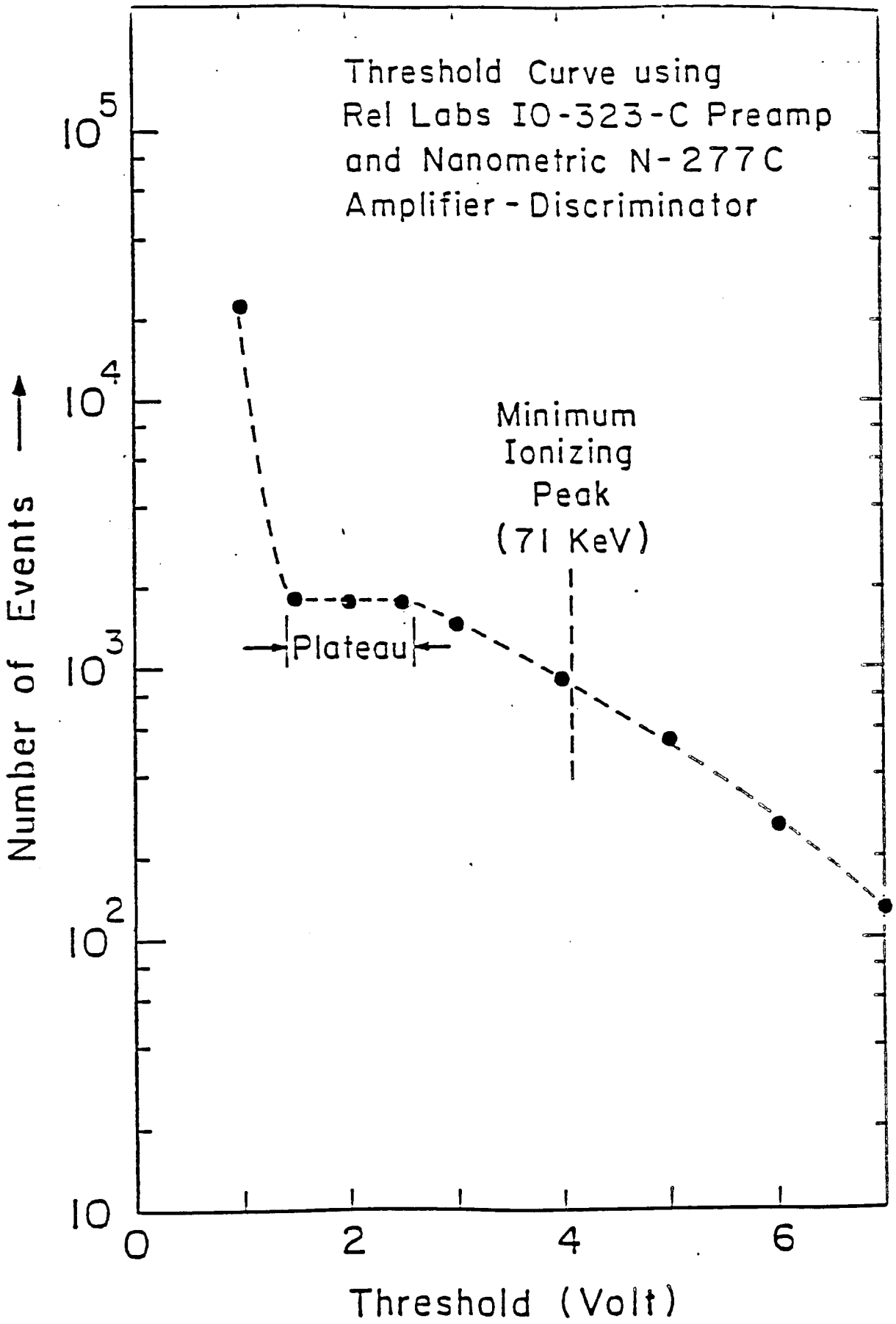

Figure IV-3: A similar discriminator curve obtained with cuts imposed to remove valley events. The plateau region is well defined and broad enough for successful discrimination.

C. ELECTRONICS INSTRUMENTATION

In section II.B we discussed the need for an electronics board for housing a large number of preamplifiers. Figure IV-4 shows the design of the Outer board that is used to mount 64 preamps. It is a two sided PCB and as the design shows the area has been efficiently used in order to have the maximum possible density of channels. The preamps are inserted into small sockets that are soldered to traces on the board. At the input end sockets are provided for ac coupling in the future if the need arises due to increased leakage currents that may cause the JFET to pinch-off. The preamps were calibrated for their gains and groups with gain within 1% of each other are plugged into the same board. The outputs of these preamps are carried on twisted-pair ribbon cables to the next stage of the electronics. The assembled version of this design can be seen in the photograph of the X-Y module in chapter II.

The N-277 circuits are provided on PC boards containing 16 channels. The number of channels on the Outer board were chosen to be 64 so that it could couple to four N-277 cards. We designed special a crate that contains 20 such cards. For two of the four groups of signals coming from an Outer board the polarity of the twisted pair gets inverted. This can be seen to be due to the symmetry of the design in Figure IV-4. A back plane for the crates was designed to unscramble the polarities. This back plane also provides an interface for coupling ribbon cables to the edge connectors needed for plugging in the N-277 cards. In the design of this instrumentation scheme we have preserved the modular nature of the overall design.

D. GROUNDING AND SHIELDING

In our treatment of noise we only considered sources of random noise. An equally important source of interference is purely man-made — the vast jungle of radio frequency (rf) signals present everywhere. These signals can be picked up by the detector electronics, especially in our case due to the large band-width. Conducting surfaces with large physical dimensions, such as plumbing and I-beams in buildings, along with the earth plane, form crude wave guides along which rf signals can propagate. They also travel along power lines that carry the 60 Hz currents. If we look

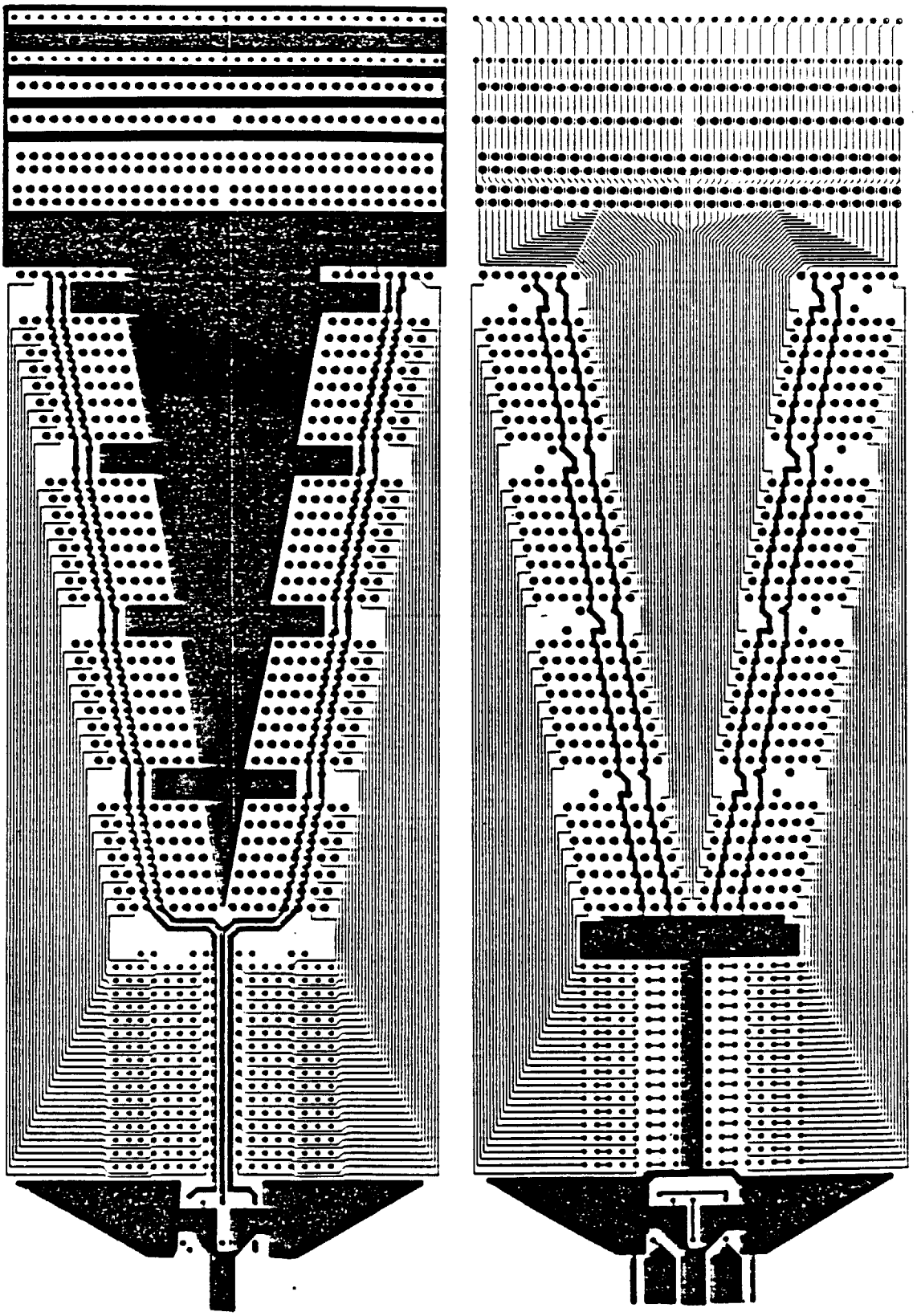

Figure IV-4: The lay-out of the Outer board for housing 64 Rel labs preamps.

at a room as forming a large capacitor between the conductors in the ceiling and the floor we can imagine high frequency potential differences existing in the environment of a lab. Clearly, the first step in solving these pickup problems is to enclose the electronics in a Faraday cage. Such a perfect shield can not be achieved if signals have to come out of it and power lines have to enter it. A small amount of rf will always be carried into shields through these conductors. This brings us to the problem of ground loops in the circuitry that can act as feedback elements and amplify such unwanted rf signals. The same feedback mechanism can also set up oscillations in the amplifiers at some resonant frequency. We will deal with the problem of proper grounding and shielding simultaneously in this section.

Let us look at Figure IV-5(a) to understand the feed back mechanism through ground loops. For simplicity we begin by assuming a perfect shield enclosing the amplifier and the detector. The dashed lines define the shield enclosure and all the relevant stray capacitances are shown as dotted lines. The capacitative link A-D-C is a feedback element and it will set the amplifier oscillating at a frequency determined by the capacitances. This is shown in the equivalent diagram of Figure IV-5(b). In order to eliminate this feedback loop the zero-reference of the signal should be tied to the shield, that is the points B and D should be shorted. For a large number of channels this requirement amounts to having the ground on every preamplifier tied to the same point on the shield. This is not too practical. Instead, simply ensuring a good connection of every preamplifier ground to a common ground and a connection of the shield to this common ground is sufficient. In our scheme, the X-Y modules are mounted on a 1/4" thick aluminum plate which serves the purpose of the common ground. The back-plane of the Middle and Inner boards are pressed against this plate and the ground plane of the Outer board is connected to it through pins. The various plates are mounted on a common support structure which is itself bolted on to a steel table. The table is a part of the shield and in this fashion we achieve a ground to shield connection. This has to be carefully done such that there is the least amount of ac impedance between the circuit ground and the shield. Any residual impedance will allow the feedback of undesired potentials.

At frequencies of the order of MHz the shield stops being perfect due to

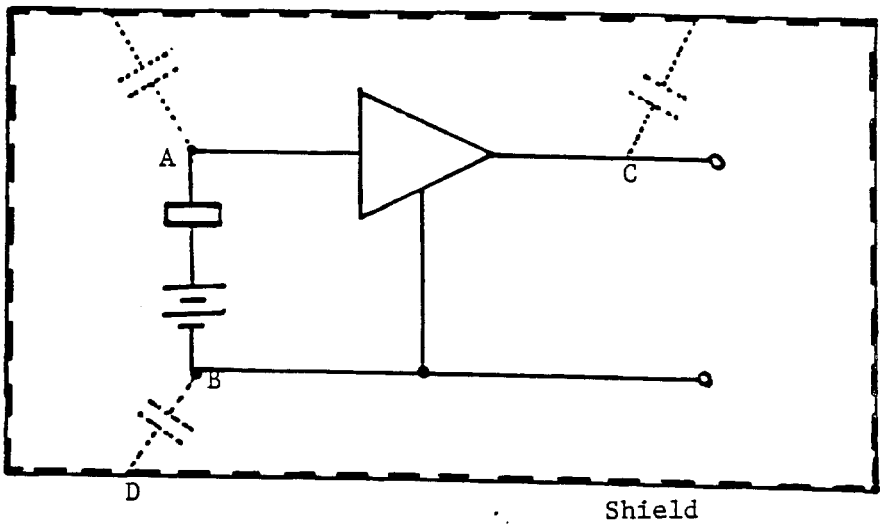

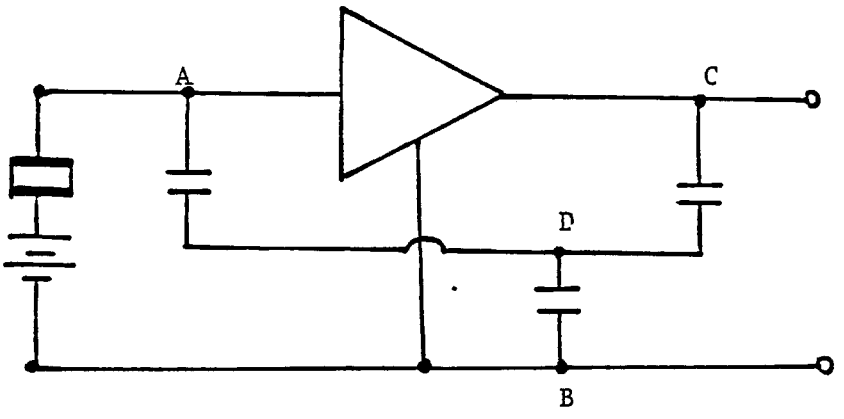

Figure IV-5: A model for understanding ground loop mechanisms (a) and the equivalent circuit for the model (b).

inductive effects. Different points on the shield can be at different ac potentials and currents can flow along the shield. In Figure IV-6 we illustrate a more realistic shield which encloses the two stages of our amplification scheme. We also allow the shield to have some holes at one end where the output of the N-277 circuit exits. The blocks A, B and C outside the shield represent external conductors that have ac potentials present on them that are different from each other. The block F is the common ground we discussed above and here we assume that it is perfect. The loop A-B-F-E-D-A is one example of current flow that will result due to external potential differences (The path F-E is through the detector capacitance). This unwanted current can be eliminated by eliminating the external differences. One way of doing this is to have a double shield arrangement and earthing the outside shield. This again may not be too practical. The currents can instead be reduced by reducing the capacitance C_{DE}. Sufficient suppression can be achieved by keeping the shield far away from signal conductors in order to reduce C_{DE}. The entire SMD system is housed in a shielded enclosure of dimensions 6' X 4' X 4', which enables us to do this.

Due to the reasons discussed above the second stage amplifier needs its own ground connection to the shield as shown in Figure IV-6 as point G. The ground connections on the N-277 were improved in order to achieve this. The circuits tended to oscillate at a frequency of nearly 20 - 40 MHz before the modifications were made. If we slowly lower the value of the threshold setting, we find that the oscillations set in at some critical value. This point will vary from channel to channel because of gain variations. With the ground modifications we were able to bring this value down to an average of about 1.1 V. On comparing it to the noise fall-off in the curve of Figure IV-3, we can see that this level is sufficiently below the desirable threshold level of about 1.5 V. Notice that the wire connection G-F will have its own inductance and it will support ac potential differences between the two ends. This leads to more ground loops feeding back all the way to the input of the preamp. This problem can be partially resolved by shorting points G and F using a large diameter copper conductor. The inductance can not be reduced to zero and some feed-back will always be present.

The most direct source of rf pickup is the exposed cable at the output. The signal at this point is digital and hence much more immune to such interference. It

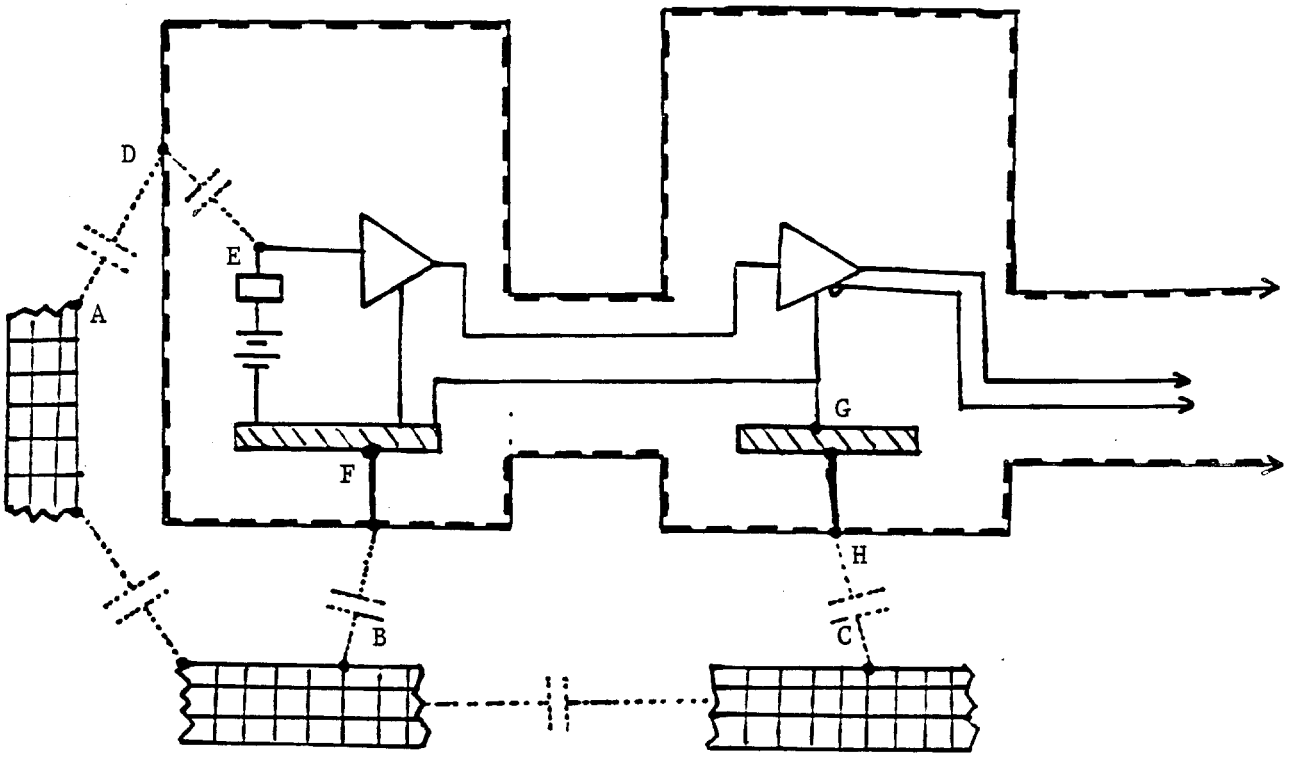

Figure IV-6: A model for a shielded circuit that encloses two stages of amplification. The mechanisms of pickup from external conductors is illustrated.

does, however, create problems as before if some of this pickup is fed back. Using twisted pair cables reduces the strength of the pickup as they present smaller cross-section to the electromagnetic flux. It would be impractical to not have any exposed cable and the extent of the enclosure can be decided upon through experimental evaluation. These cables are 50' in length and in our present design we plan to shield about 40' of its length.

We have not as yet included any power sources in our scheme. All the circuits discussed above operate from dc power supplies which in turn are powered by the commercial ac power. Linear power supplies that have very little (<0.01%) ripple at their output are readily available. Using such supplies ensures that the amplifiers are not contaminated by 60 Hz ac in the signal lines. The ac lines also bring rf along with the 60 Hz power. The most effective solution to this problem is to put the dc power supplies inside the shield enclosure and filter the ac lines in order to let only the 60 Hz current through. This filtering can be achieved using an isolation transformer. Figure IV-7 shows a schematic representation of such a device.

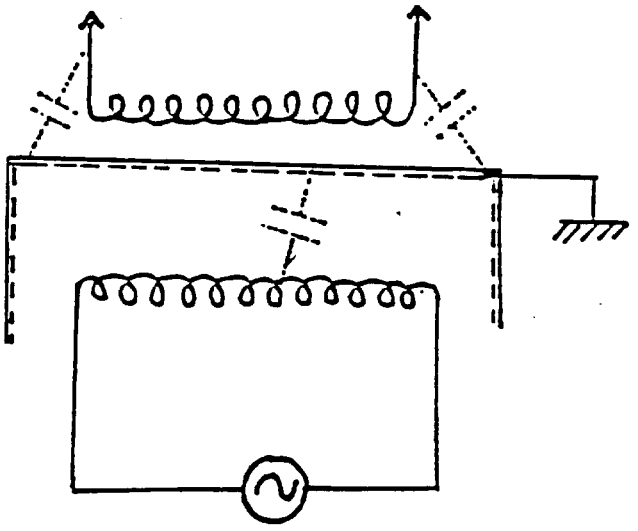

Figure IV-7: The schematic of an isolation transformer.

A thin conducting foil placed between the primary and the secondary coils does not effect the magnetic coupling between them. If it is grounded, however, it does provide a low impedance capacitative path to ground for the high frequency rf signals. Since

the secondary is within the shield it only couples to the low frequency flux from the primary and the 60 Hz signal can pass through. The design shown in Figure IV-7 will not make a very good transformer due to high power losses and hence in practice very complicated geometries are used to maximize the coupling. This results in some of the secondary coil coming out of the shield. Again a double shield could be used. As before, the ground on the transformer should be tied to the signal reference ground to eliminate effects due to shield currents.

The power for the N-277 circuits is provided through switching supplies that can drive high current levels. These supplies have internal switches operating at nearly 40 KHz. The transients from these switches enter the circuitry but they are not a problem as long as they stay at threshold values of nearly 1 V. This can be made possible with adequate filtering of the dc output.

In Figure IV-8 we show the final design for the system based on all the considerations discussed above. It shows a cross-section of the apparatus from a beam's-eye view. Since the preamps on the Outer board are stacked close together the space in between them collects a dead layer of hot air. We employ ac operated fans to force this air out. These fans are fed by the isolation transformer and hence do not present a new source of rf inside the shield. The bulk air from the enclosure will be exchanged continuously with dry and cool air using a compressor and filter system that is not shown in the design. The Nano circuits are housed in crates that have an array of fans at the bottom. This provides sufficient cooling. A blower in the racks takes care of the intake of fresh air.

It should be mentioned that this scheme is adequate for our purposes based on lab tests. However, an understanding of the principles does enable one to modify the design in case the need arises due to the different environment of Fermilab.

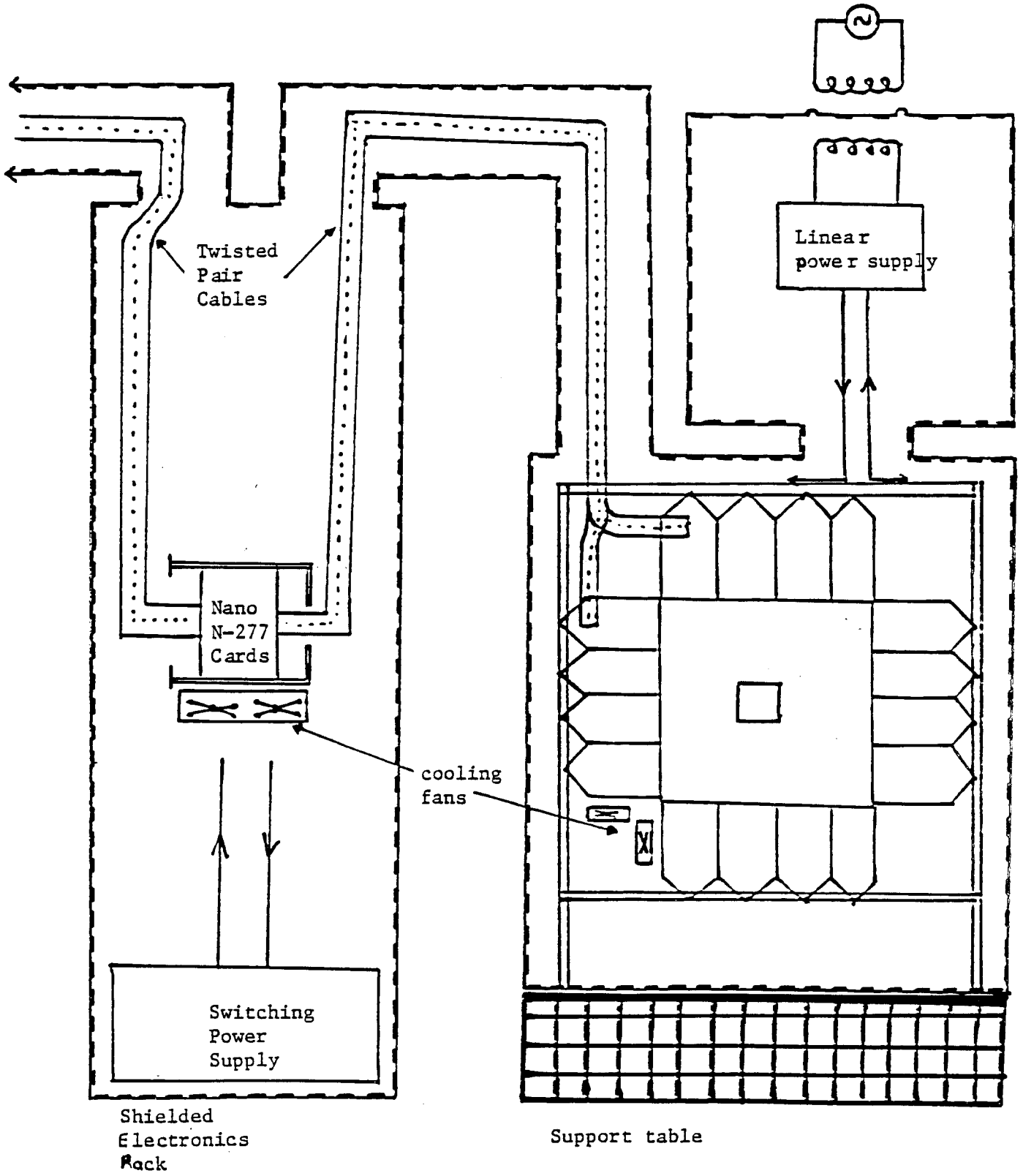

Figure IV-8: The design for the shield enclosure for housing the SMD modules and the two stages of the electronics. The power supplies are shown at the top. This diagram is only schematic and not to scale.

E. DIGITAL CONTROL AND READ-OUT

The signals from Nano N-277 circuits are purely logical and at most 45 ns in duration. These signals in coincidence with a trigger pulse provide us with the data on any event. This coincidence is performed in the next stage of the Nano system, the N-278 CAMAC latch modules. These modules are also capable of delaying the data pulses internally for a maximum duration of 800 ns. The delay time can be programmed into the latches by the user. A dedicated controller module, the N-280, is used to control a CAMAC crate filled with these latches. It is capable of reading the latches, filtering the data and sending the information on the hit strips. Each strip is labeled by an address that can be defined at the beginning of a run by the user's software. The communication between the N-280 and an external computer is carried out using the N-281 CAMAC interface module which in turn can be monitored by another CAMAC controller. The data from the N-280 is received by the N-281 and transferred to the second CAMAC controller. Finally this data can be read into the memory of a computer for processing and storage. This scheme is shown in Figure IV-9 where a LeCroy 3500M system is used for the control. Built into the 3500M is a microprogrammable CAMAC controller that employs a bit-slice processor. This provides us with a sufficient speed to carry out the tests on the Nano system.

As shown in Figure IV-9 a fast pulse can be applied to the back of the wafer through a 1 nF capacitor. This pulse is fed into the preamplifiers through the capacitance of the strips which is of the order of 1 pF. This provides an alternate made of testing the electronics without using the electron source. It also enables us to exercise a large number of channels in the electronics simultaneously. Using this scheme for testing we found and eliminated the faulty electronics channels. The system was tested successfully up to trigger rates of 100 Hz and an event size of typically 500 words.

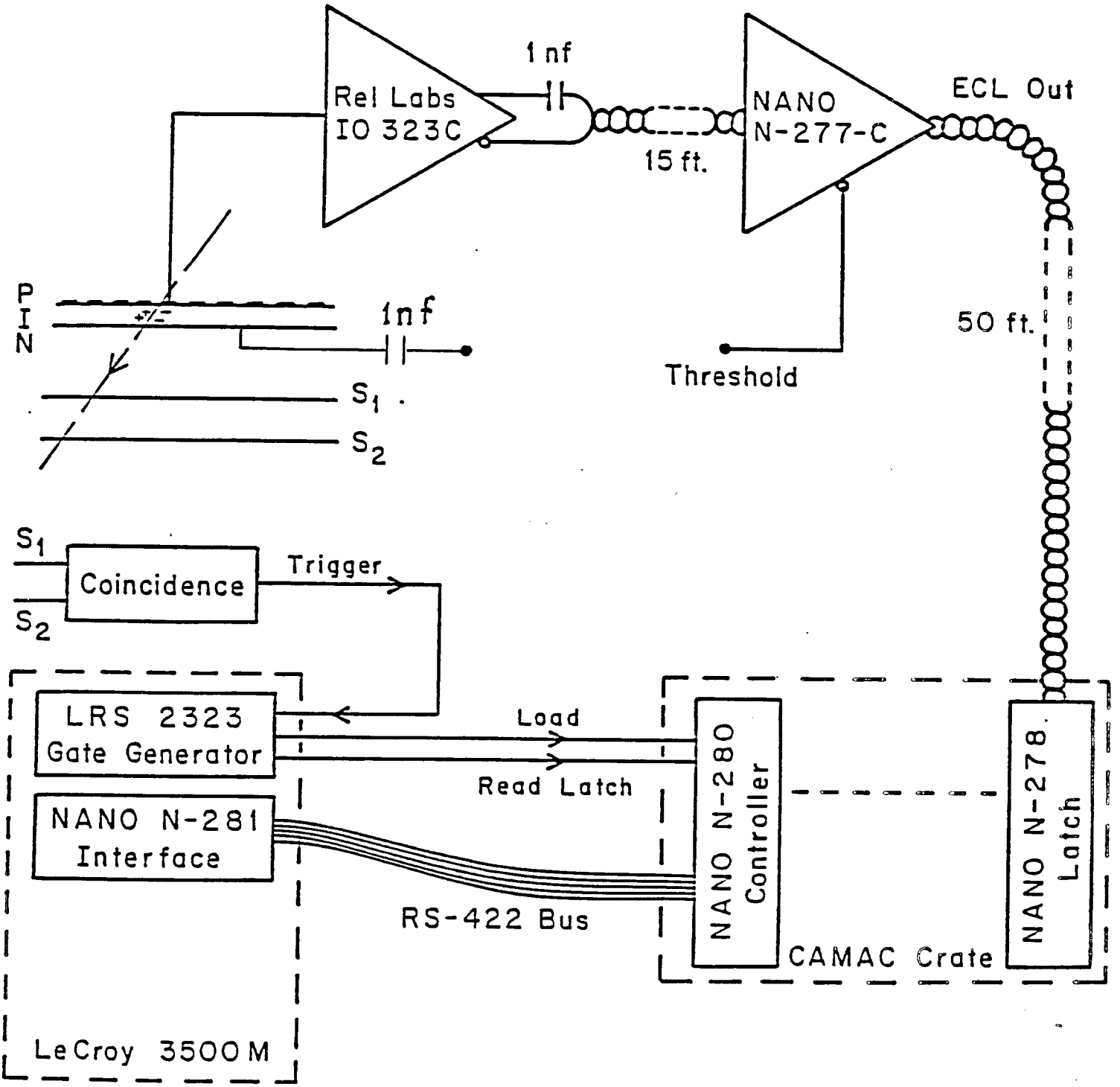

Figure IV-9: The read-out scheme using the Nano system and a LeCroy 3500M microprocessor.

F. TESTS OF AN ASSEMBLED SMD

Figure IV-10 shows an example of the data collected using the electron source in the scheme of Figure IV-9. It is a histogram of the number of hits on the strips of an SMD with a threshold setting of 1.5 V. The profile of the electron source can be seen peaking towards the right. The shape of the profile can be understood in terms of the geometry of the set-up. The peak is directly under the source. The strips further away from the peak receive electrons at an angle to the normal and on the average a certain number of tracks go through two neighboring strips. These tracks may not register on either of the two strips because the pulse heights may fall below the threshold due to fluctuations. This results in a reduction in the number of counts on these strips. A small reduction also occurs because these strips present a smaller solid angle to the source and receive a smaller number of electrons to begin with. The histogram also shows a few strips with off-scale counts. These are channels for which the critical threshold level for oscillation is above 1.5 V. In further tests these circuits get rejected. The strips with zero or nearly zero counts have different problems associated with them. These can be understood by looking at the noise on these strips. Figure IV-11 shows the background levels obtained by removing the electron source and triggering the system for the same number of times. One can see that the strips that showed nearly zero counts have normal noise levels. These are strips on which either the bonding wire has come off during the course of testing or a trace has broken on the Inner board. This is so because a normal noise level means that the circuit is in a working condition. Now, the channels with zero counts are still dead. These are hard to explain and probably are due to a broken wire somewhere in the circuit. From this histogram one can also get an estimate on the probability for a channel to give a false hit signal. The average on this number is about 10^{-4} or .01 %. In other words, for a 1000 strip wafer, on the average we expect a noise count to occur once in about every 10 trigger gates. This is certainly a very acceptable situation.

Figure IV-12 shows the data after background subtraction. The width of the band is considerably broader than the statistical error on the number of hits. This can be attributed to two main causes. First, we expect the areas of the strips to vary by a certain amount which is of the order of the tolerance in the photolithography steps in

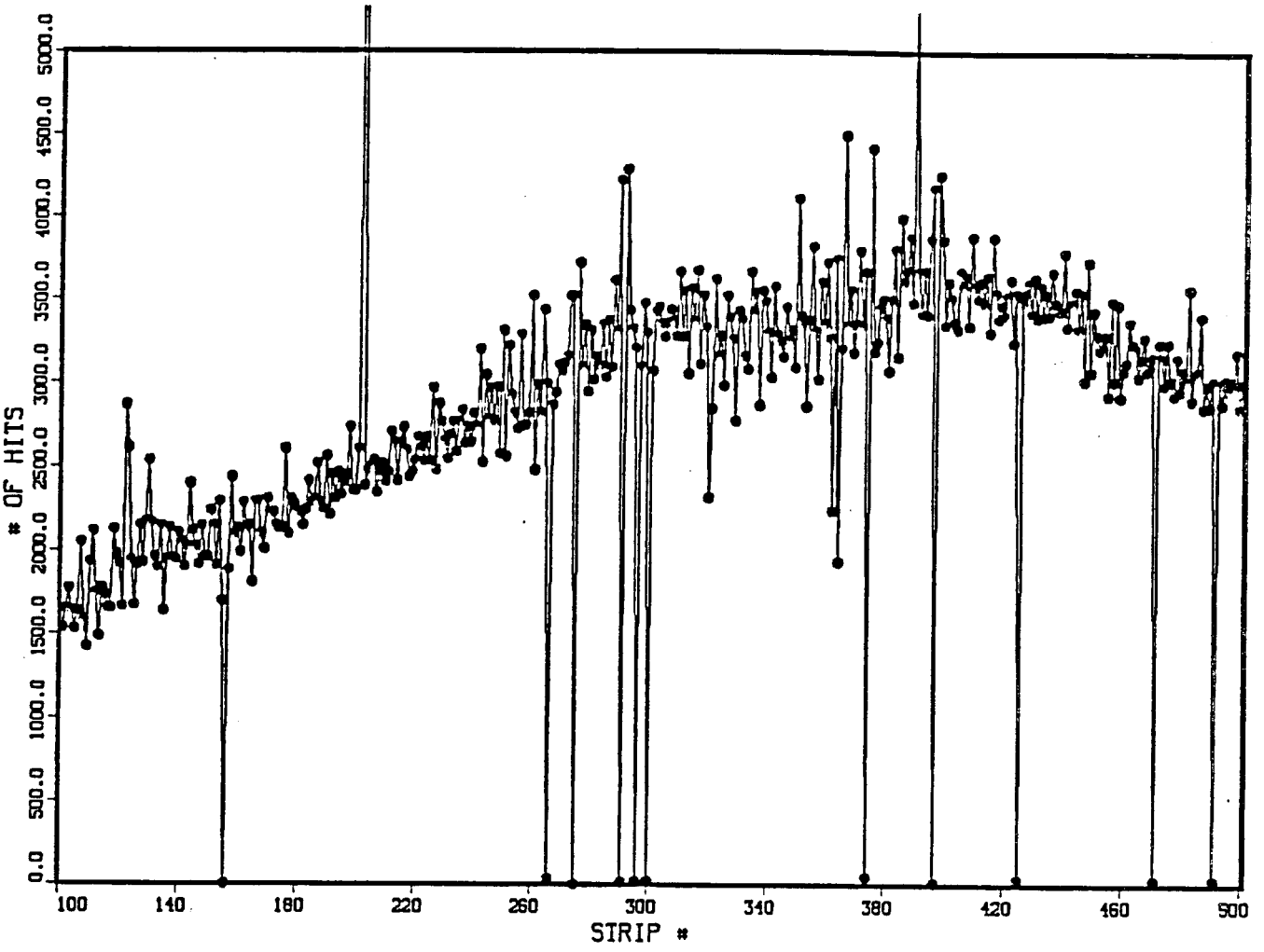

Figure IV-10: A histogram of the hits on an SMD from an exposure to the electron source

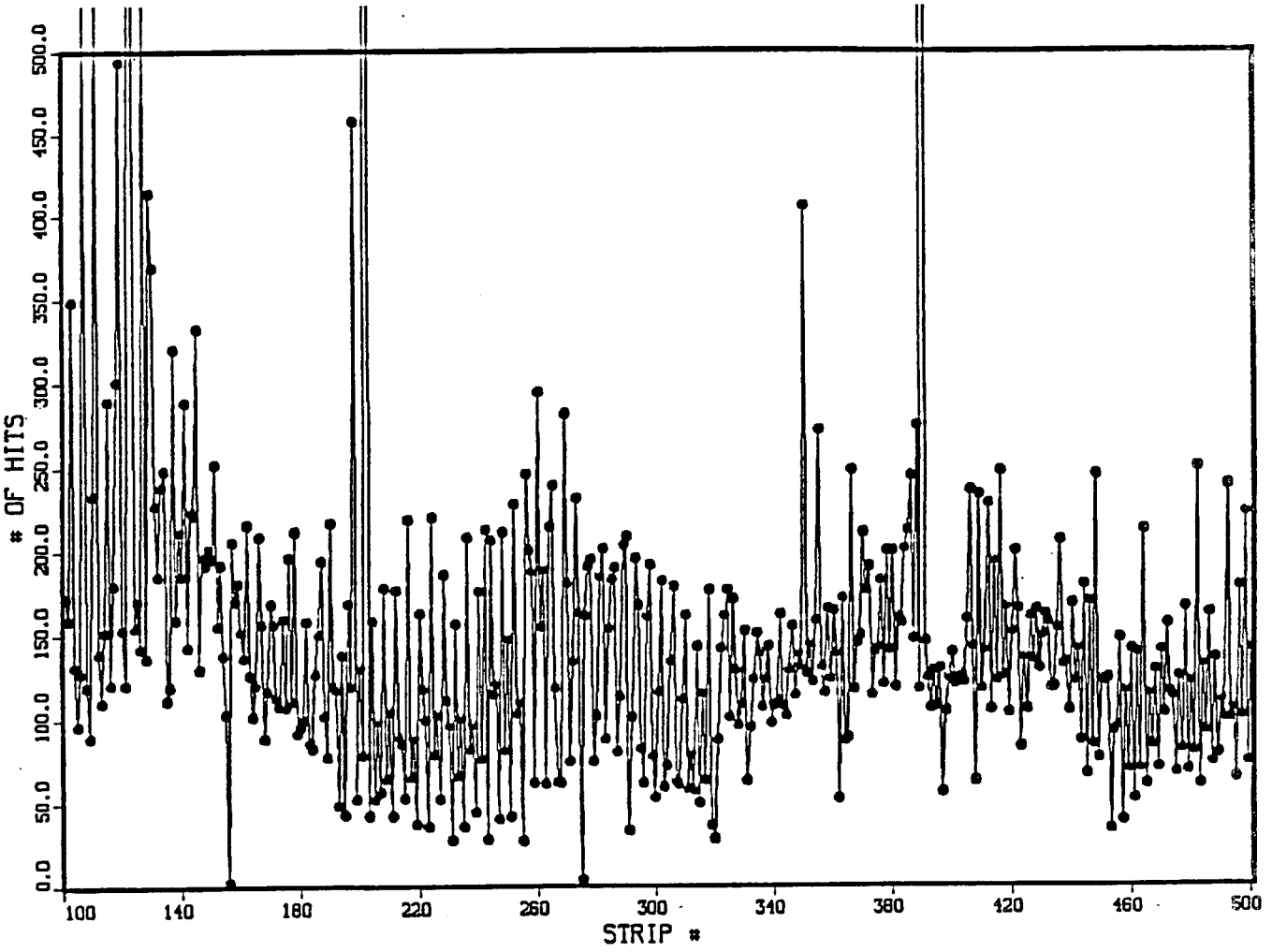

Figure IV-11: A histogram of background hits using the same configuration as in Figure IV-10.

the planar process. An error of 1 μm on either edge of a strip is equivalent to a 4% error in the area. We expect the strips to have this variation in the solid angle that they present to the source. Second, there is a certain amount of variation in the gain from channel to channel in the N-277 circuits. In principle this should not affect the counts due to mips. The much-blamed valley events do affect the counts because some of these pulses are at the same height as the threshold. These pulses will account for extra counts on the channels with high gain. A channel by channel analysis was done for a smaller number of strips. ADC curves were recorded for these strips using the same electronics channel in each case. The differences in the number of counts above a given point in these curves correlated very well with the differences in the counts for the same strips in the data of Figure IV-12. This is not a direct test of the suspicions raised above but it does rule out any suggestions of new problems that have to do with the Nano system.

Some of these details in the performance of the SMD system will only be ironed out in beam tests. Nevertheless, from the instrumentation point of view we can consider this design to be successful. In the next chapter we turn to the issue of event simulation.

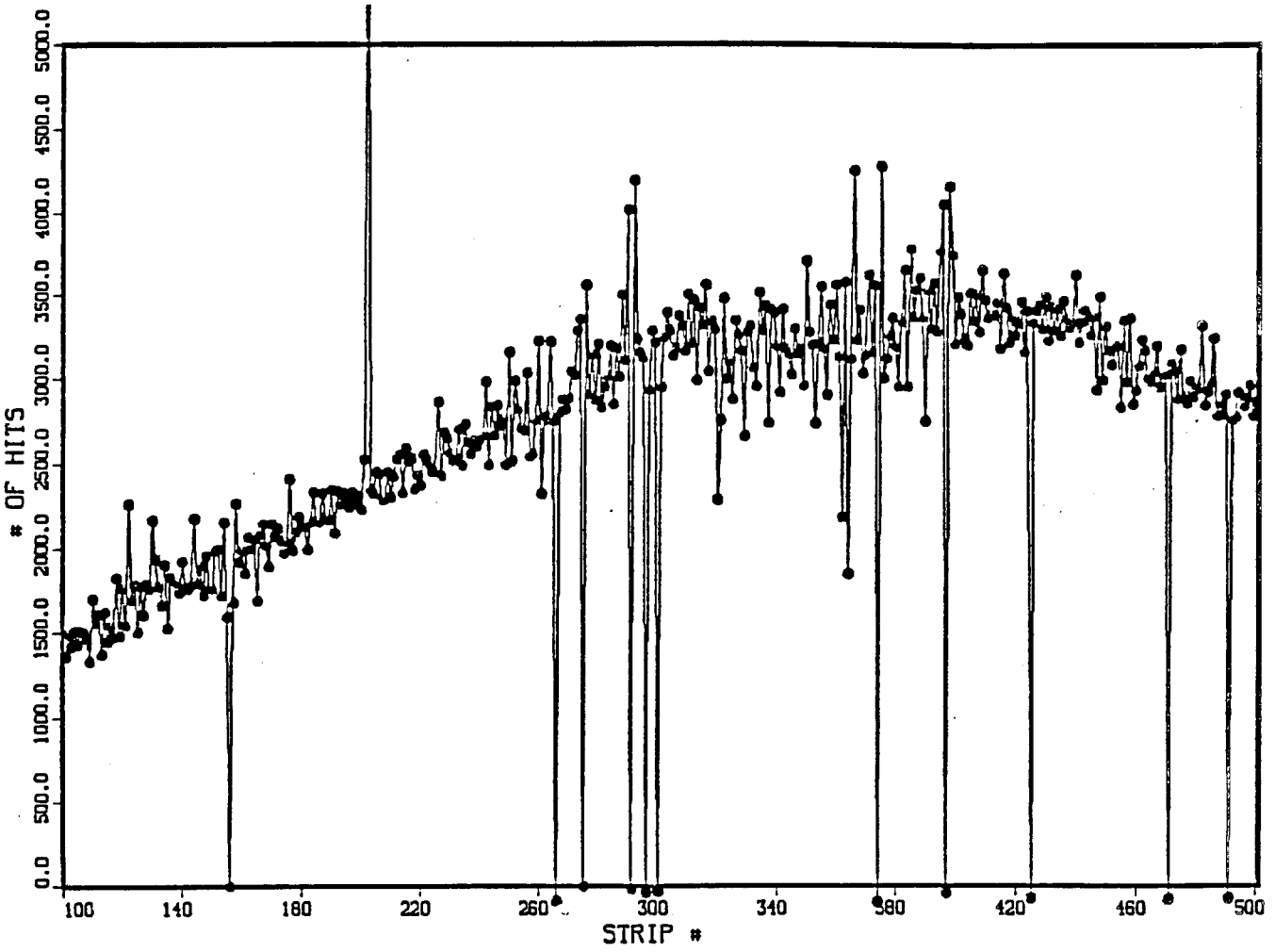

Figure IV-12: The histogram of Figure IV-10 after background subtraction.

CHAPTER V.
MONTE CARLO SIMULATION

A. INTRODUCTION

In section I.B. we discussed the parton model for understanding the scattering of hadrons. The model required the use of various probability functions to get the details of a particular scattering event. The nature of the fragmentation functions makes it impossible to arrive at analytical expressions for the overall cross-sections. This makes the use of Monte Carlo techniques imperative. They are used extensively nowadays both for simulation of events and also for extracting results from the data. In section 2.2 we arrived at rough estimates for the performance characteristics of our design. In this chapter we present our estimates based on Monte Carlo simulation of events. In order to do so we used the ISAJET program[35] which was originally written for simulating p-p collisions at Brookhaven National Lab. It has become more and more sophisticated [36] over the years with continual feedback from experiments. Figure V-1 shows the major components that a present day Monte Carlo simulation program like ISAJET needs. The breakdown is based on the parton model picture of Figure I-2 with a few additional steps. The steps shown are not necessarily executed in that order. The addition of gluon radiation, by initial and final state partons, in the program structure brings it a step closer to reality. This, in effect, is equivalent to considering higher order QCD graphs. The evolution of the final state partons is done using an algorithm based on Altarelli-Parisi functions[37]. The initial state radiation is simulated using the backward evolution scheme developed by Gottschalk[38]. The hadronization of the final state partons follows the Field-Feynaman approach[11]. Another model for hadronization has been developed which uses a string formulation[39] but it is not used in ISAJET. Suffice it to say here that ISAJET is regarded as a highly reliable program and the predictions, though not exact, come close to the experimental results.

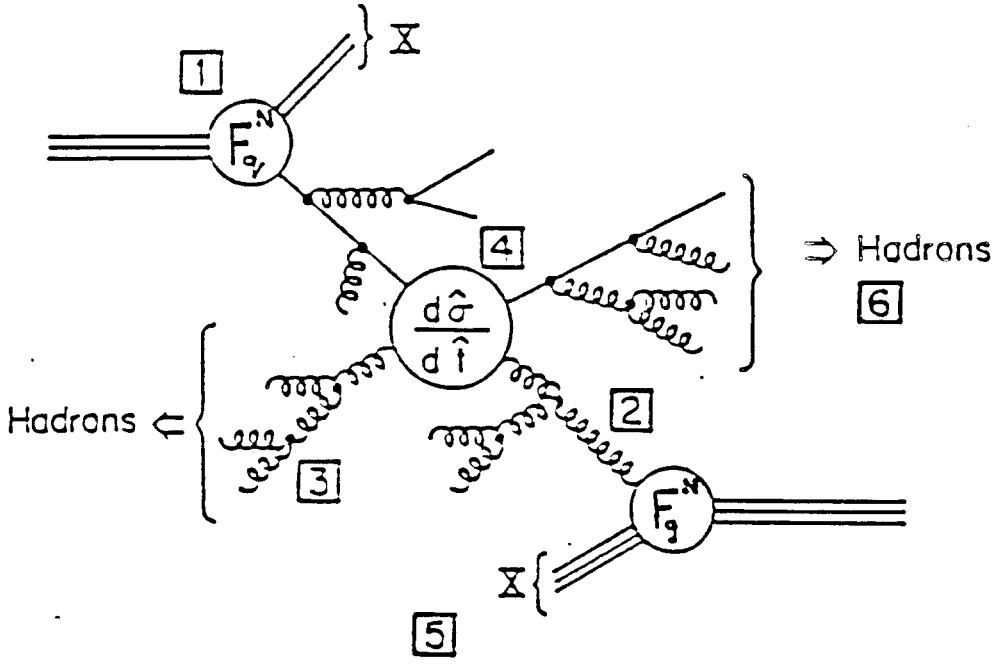

Components of high-p_T scattering models.

1. Parton structure functions
2. Initial state perturbative QCD evolution
3. Final state perturbative QCD evolution
4. Hard constituent subprocesses
5. Evolution of beam remnants
6. Hadronization of the parton final state.

Figure V-1: The major components of a Monte Carlo event simulation program

B. SIMULATION OF DIRECT PHOTON EVENTS

The ISAJET program does not have a process built in for direct photon production. However, it does have a process similar to it as shown in Figure V-2.

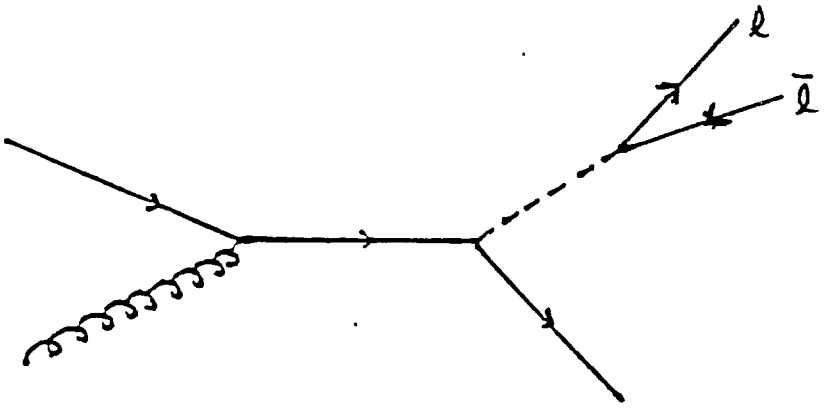

Figure V-2:

The dashed line represents a virtual gauge boson which fragments into a pair of leptons. It can be a photon as well as one of the massive gauge bosons W^+, W^- or Z^0. The program allows the user to select a range for the virtual mass of the gauge boson and by choosing a range of very small masses (5-10 MeV) we can not only restrict it to be a photon but also make it a nearly on-shell photon. Then by adding the four vectors of the e^+-e^- pair and neglecting the small mass we can make this process look like direct photon production. This method is correct except for an overall error in the normalization of the cross-section. The error is of the order α_{em} multiplied by a phase space factor for the lepton pair.* This error is not important if we want to study the general characteristics of events. Figure V-3 shows a relative cross-section versus p_T as estimated in this fashion for proton and anti-proton beams. The relative cross-section can be seen to have a strong dependence on p_T. The relative contributions from the annihilation and Compton diagrams for both the beams is shown

---

*The factor $\alpha_{em}/3\pi m\gamma^2$ gives a result correct to within 10 %

ISAJET PREDICTION OF DIRECT PHOTON PRODUCTION IN $\bar{P}$ P COLLISIONS

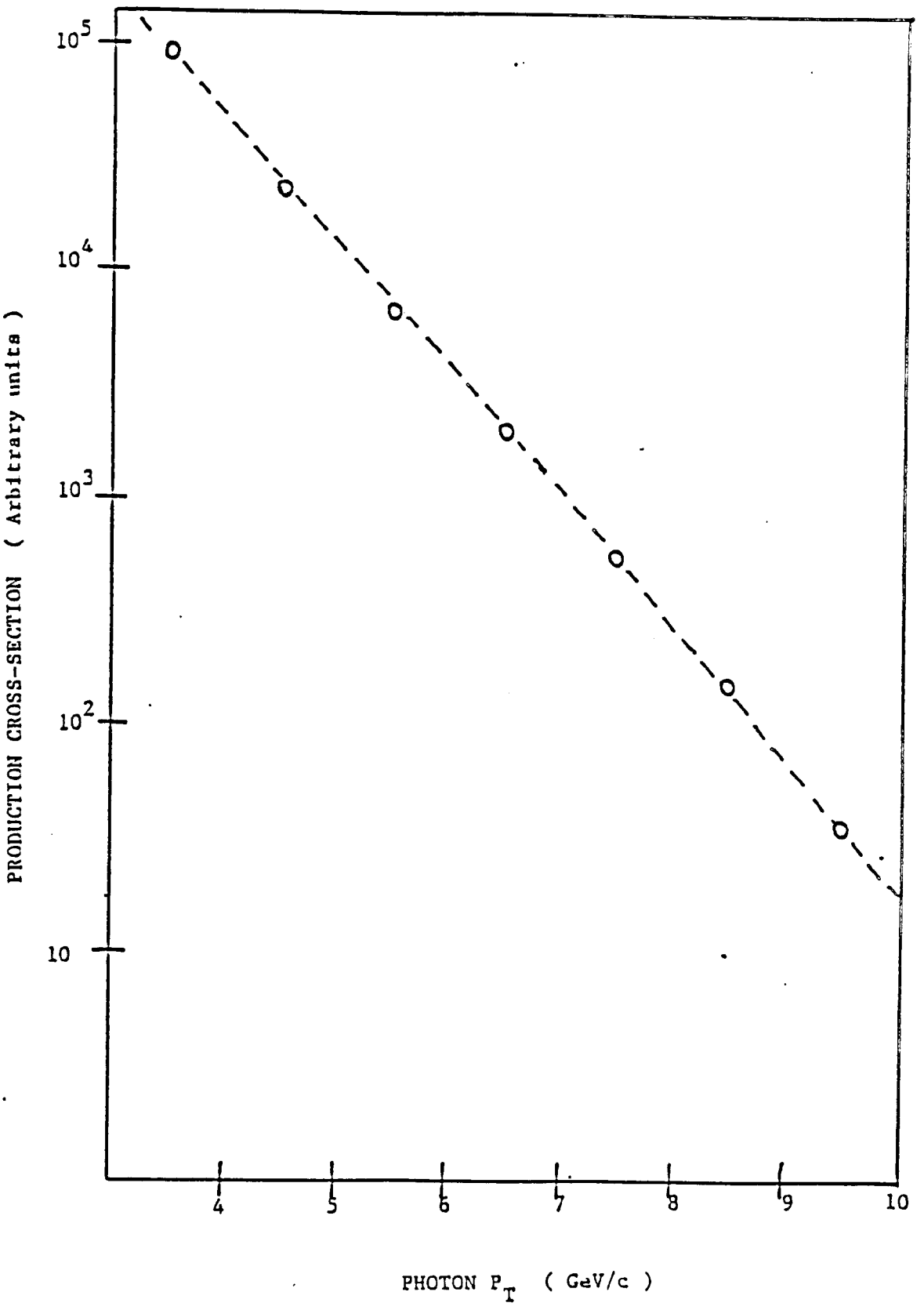

Figure V-3: The relative production of direct photons in proton anti-proton collisions as predicted by ISAJET.

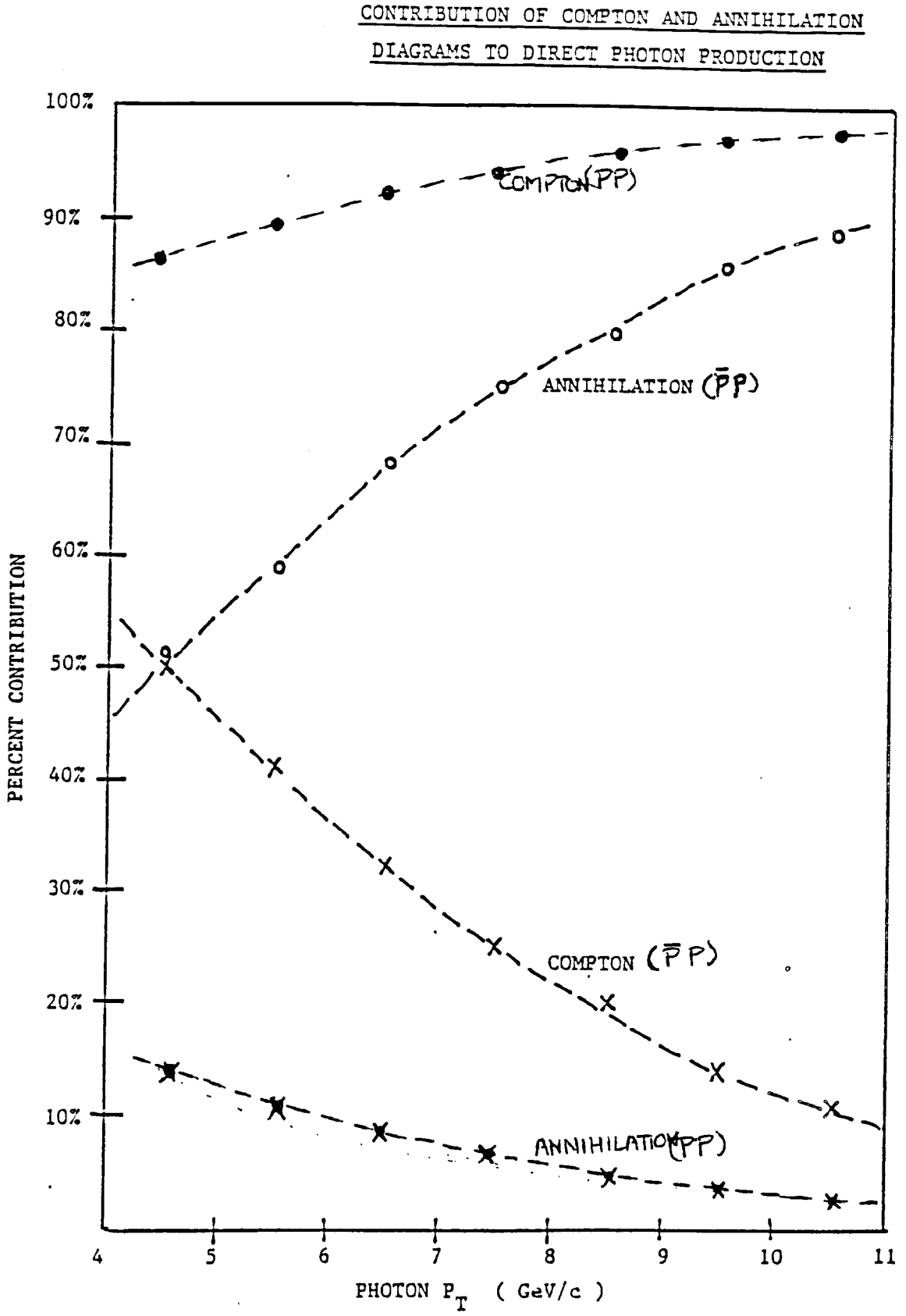
CONTRIBUTION OF COMPTON AND ANNIHILATION
DIAGRAMS TO DIRECT PHOTON PRODUCTION
100%
90%
80%
70%
60%
50%
40%
30%
20%
10%
PERCENT CONTRIBUTION
COMPTON (PP)
ANNIHILATION (P̄P)
COMPTON (P̄P)
ANNIHILATION (PP)
4
5
6
7
8
9
10
11
PHOTON P_T (GeV/c)

Figure V-4:

in Figure V-4. The scattering from pion beams can not be simulated as the structure functions are not contained in the program. A comparison of the two beams as shown in Figure V-4 does show the dominance of the annihilation diagram at high p_T for the $\bar{p}$ beam and of the Compton diagram for all values of p_T for the proton beam.

For the SMD telescope the physics of interest lies in the charged particle content of any event. Hence the relevant event size is the total number of charged particles in the away-side jet and in the beam fragments. Figure V-5 shows an ISAJET event superposed on the SMD system. This is an event with a relatively high photon p_T of 8.22 GeV/c. The tracks are plotted for both the beam (spectator) jet and the away-side jet. The tracks from the two sources can be seen to be not very clearly separated. Further contribution to the charged particle content of an event is made by charged particles coming out of any secondary interactions. To get an idea of the typical event structure we should look at average quantities. Figure V-6 shows the average expected multiplicities versus the photon p_T. All the different components are plotted. Figure V-6(a) shows the break-up of a jet into i) all charged particles, ii) photons and iii) neutral hadrons that do not decay into photons. Figure V-6(b) shows the same thing for beam fragments. The main source of the photons are π^0 decays. These photons average to about 12 per event. This plays an important role in the choice of target materials. For a material with a large ratio of interaction length to radiation length, more photons will convert to e^+-e^- pairs. This can make the task of vertex reconstruction more difficult. In E706 we plan to use a maximum of 0.1 interaction length for the target thickness. This corresponds to 0.1 radiation length for Be, 0.2 for C and 0.95 for Fe. These three are the materials being considered at the moment for various reasons. Clearly, they will provide very different conditions for vertex reconstruction. The rest of the neutral hadrons contribute very little to any event. Hence they do not present a major source of secondary interactions that lead to charged particle production. If we sum up the all the different components the total multiplicity can be seen to stay unchanged over the p_T range as expected from energy conservation. However, the angular distribution of particles in any event will strongly depend on the p_T.

Figure V-7 shows the ISAJET prediction for the average angular distribution of

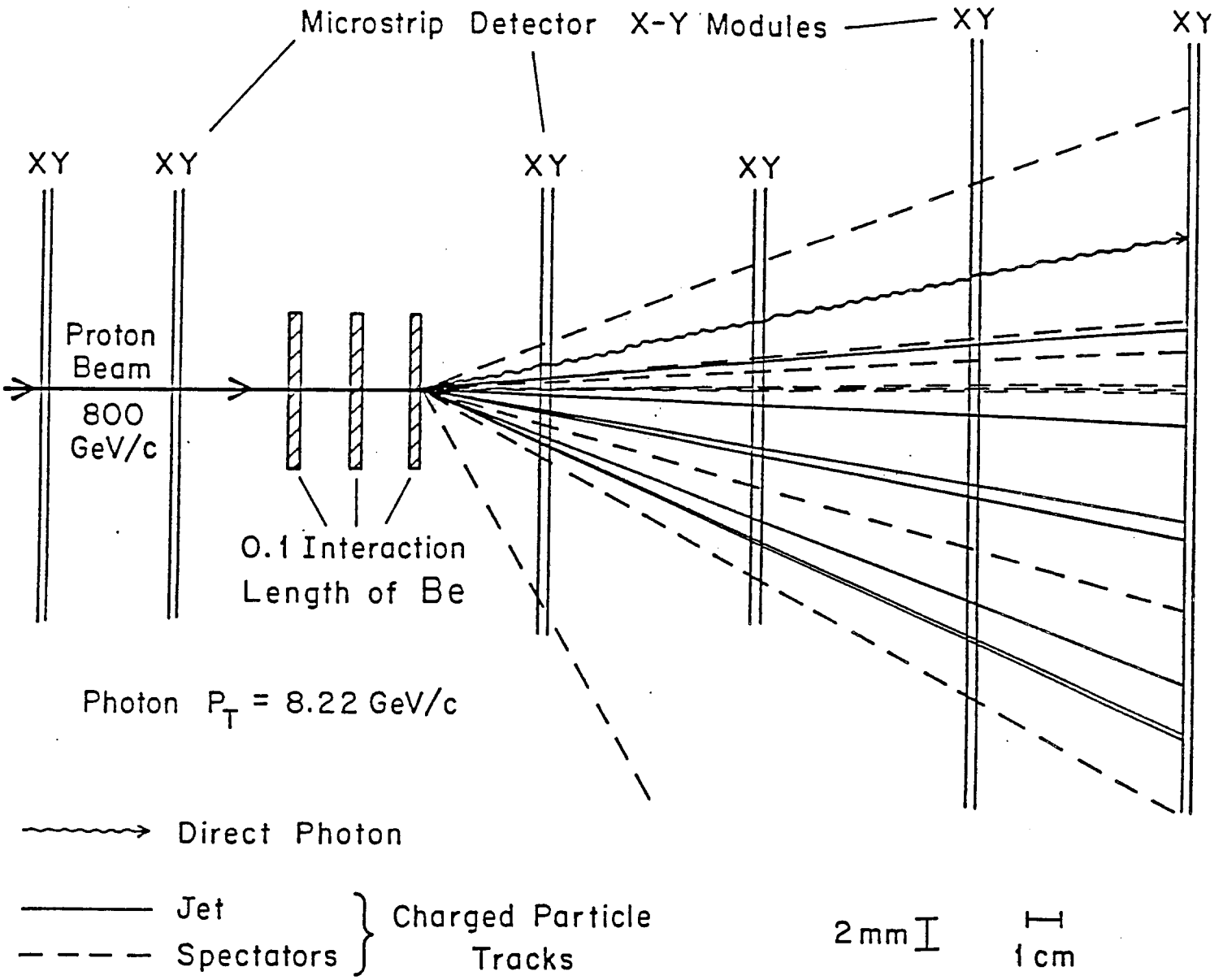

Figure V-5: An ISAJET generated event superposed on the SMD system.

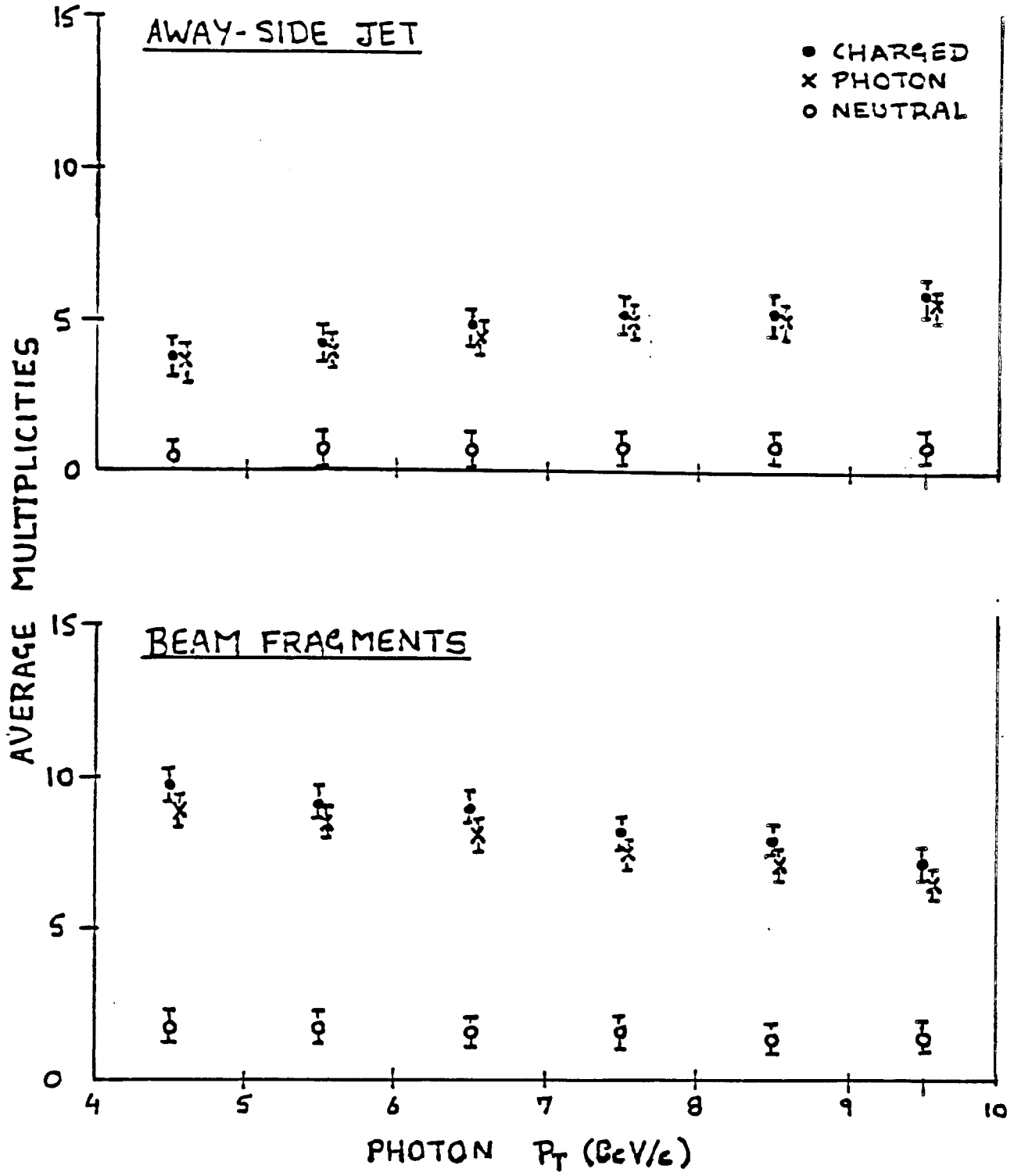

Figure V-6: The predicted multiplicities of particles in an event based on ISAJET. The various components of the a typical event are shown. As can be seen the total multiplicity remains relatively unchanged over the p_t range.

charged particles for typical events with a photon p_T > 7 GeV/c. The average number of charged particles per event per milliradian is plotted against the angle in mr. For the first X-Y module the angle subtended by one strip is approx 1 mr. Hence the plot can be interpreted as the probability per strip for having at least one particle go through it in any event. The probability of any strip at an angle >40 mr being hit is not very large. This is relevant because of pile-up considerations. For a beam rate of 10^7 particles per second we have on the average 100 ns between two consecutive beam particles. For 10 % interaction length we have an interaction every μs on the average. The pulse from the front end of the Nanometric amplifier has a tail of nearly 300 ns. From Figure V-7 we see that the central strips which are in the beam profile have a maximum probability of about 23 % per event. The beam has a spread of about 1 cm and for this central region we can consider 20 % to be an average probability for a strip to be hit. From Poisson statistics we expect a probability of 0.5 % for two interactions to occur within 300 ns of each other. This implies a pile-up probability of 0.1 %. This does not seem to present any limitations on the acceptable rate.

C. COMMENTS ON RESOLUTION

In this section we briefly mention some preliminary results on the reconstruction of events and resolution achievable based on these ISAJET simulated events. We will start by confirming our rough estimate on z resolution from section 1-2. Using the formula for Δz on every track in an event we find the track that gives us the best value. In Figure V-8 we have histogrammed the angles and momenta of the best tracks for a large sample of events. Based on the two peaks we can claim that a 60 mr track with a momentum of 5 GeV/c is typical of any event. Figure V-9 shows a histogram of Δz values for these tracks. A value of Δz in the range 2-4 mm can be seen to be typical.

The resolution can be improved upon by considering all tracks and finding the best fit for a vertex. In Figure V-10 we show some preliminary results from the software under development. It shows an example of a reconstructed ISAJET event. The program takes the ISAJET event and introduces multiple scattering and secondary interactions in it. Then it reconstructs tracks by correlating four hits and finds the

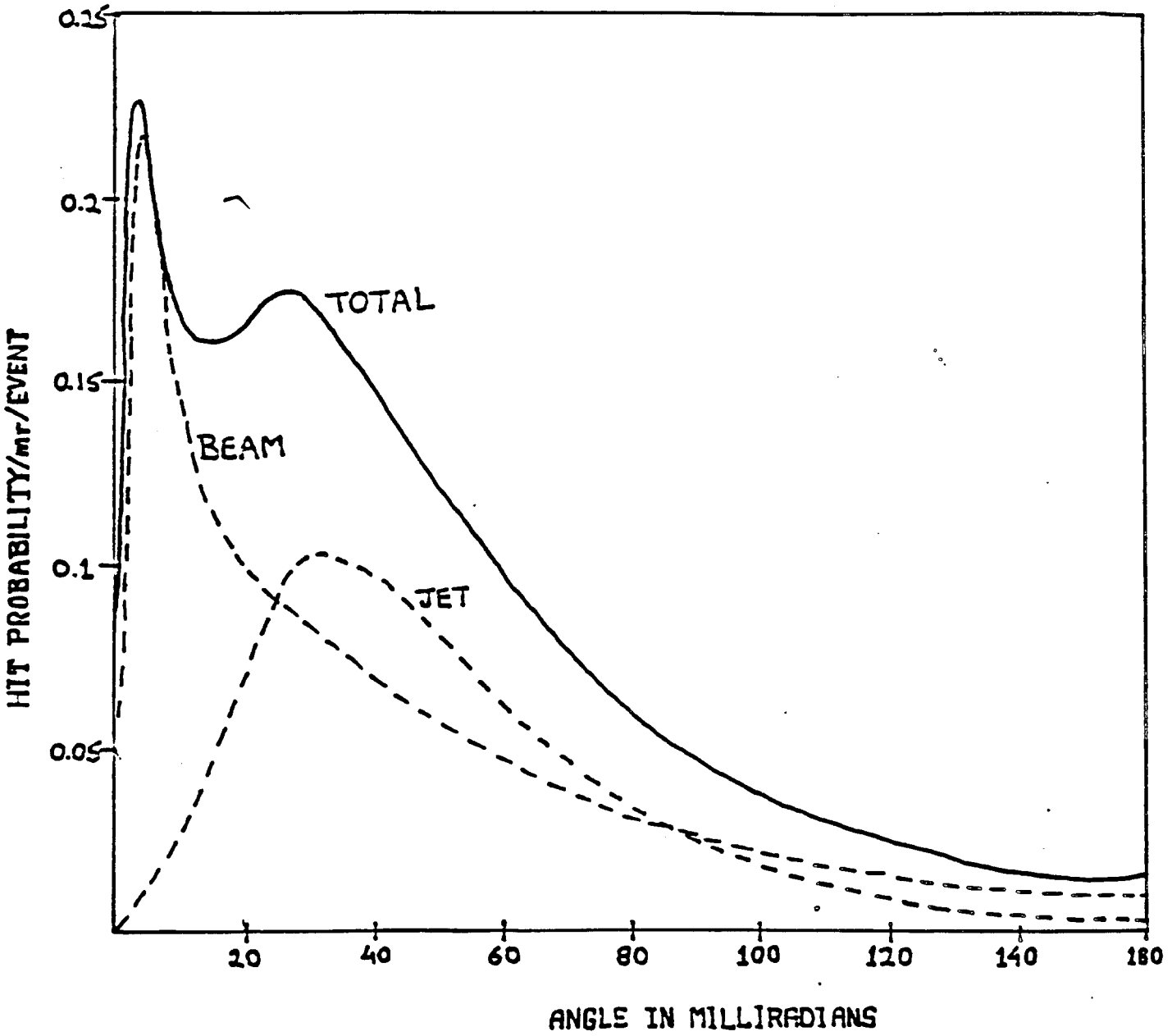

Figure V-7: The probability per event for having a charged particle in a 1 mr cone is plotted versus the angle in mr. The dashed curves show the origin of the particle.

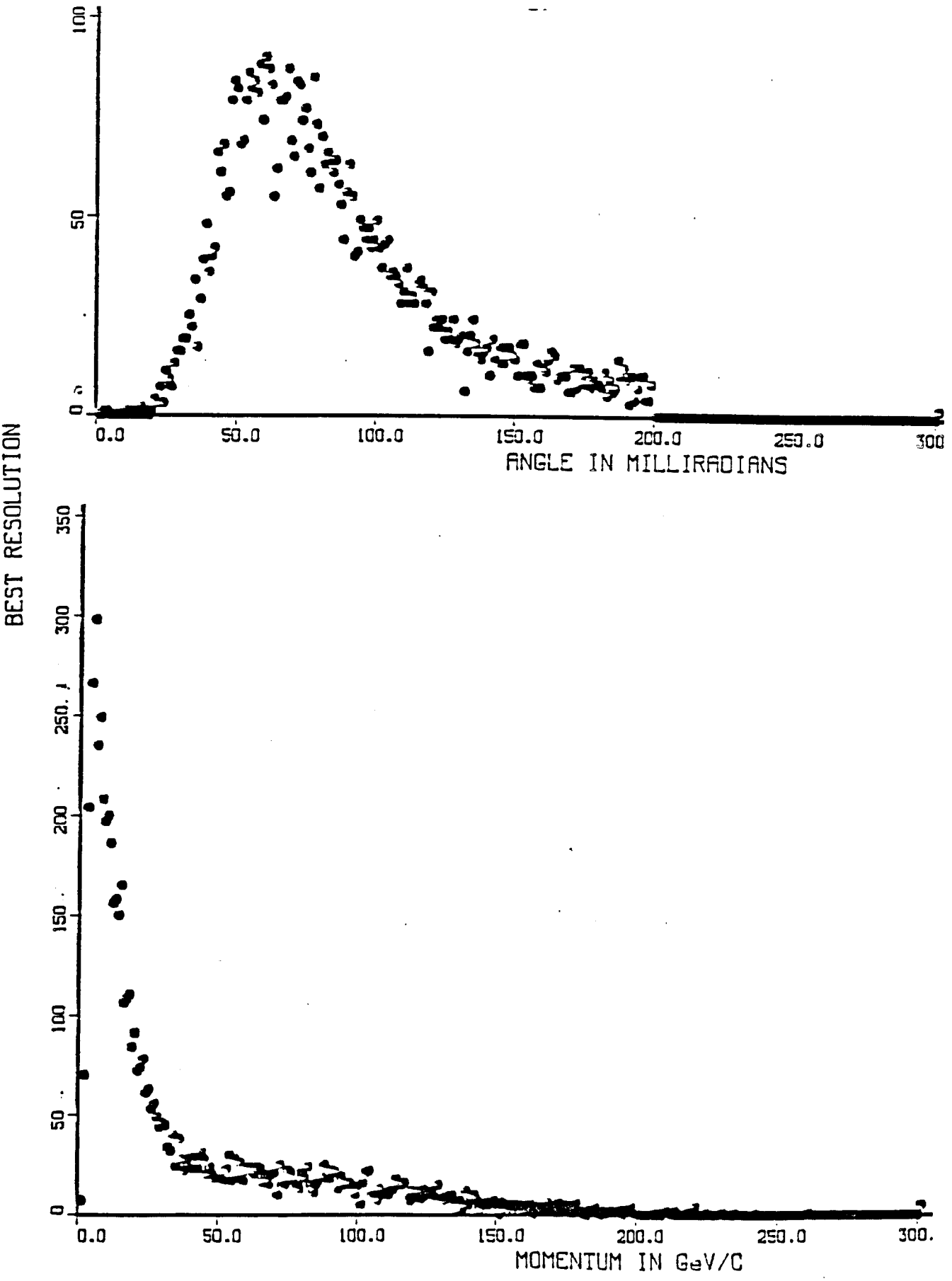

Figure V-8: The histogram of (a) the angles and (b) the momenta of the tracks providing the best z-resolution.

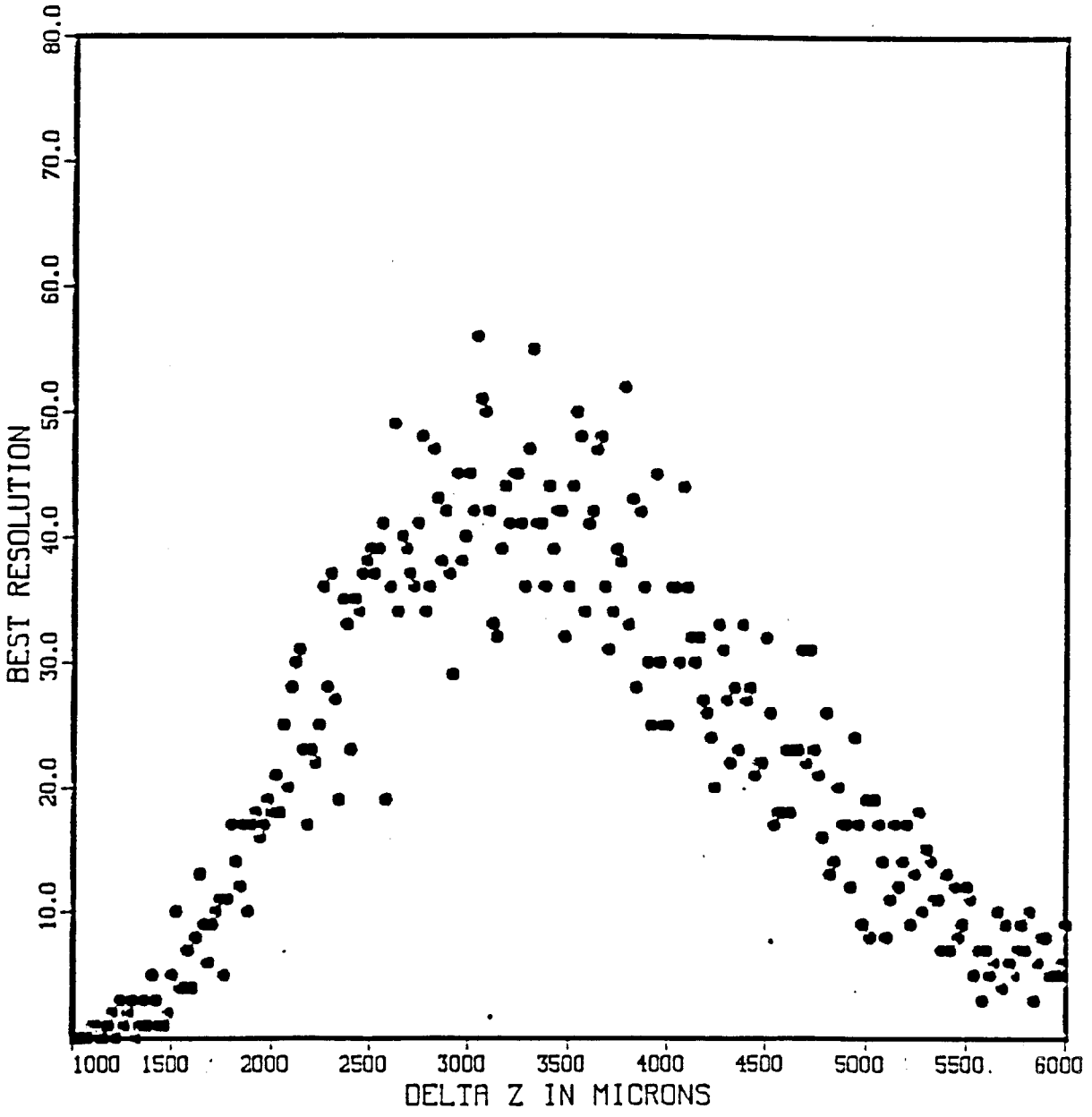

Figure V-9: A histogram of the values of Δz obtained from the best track in ISAJET events.

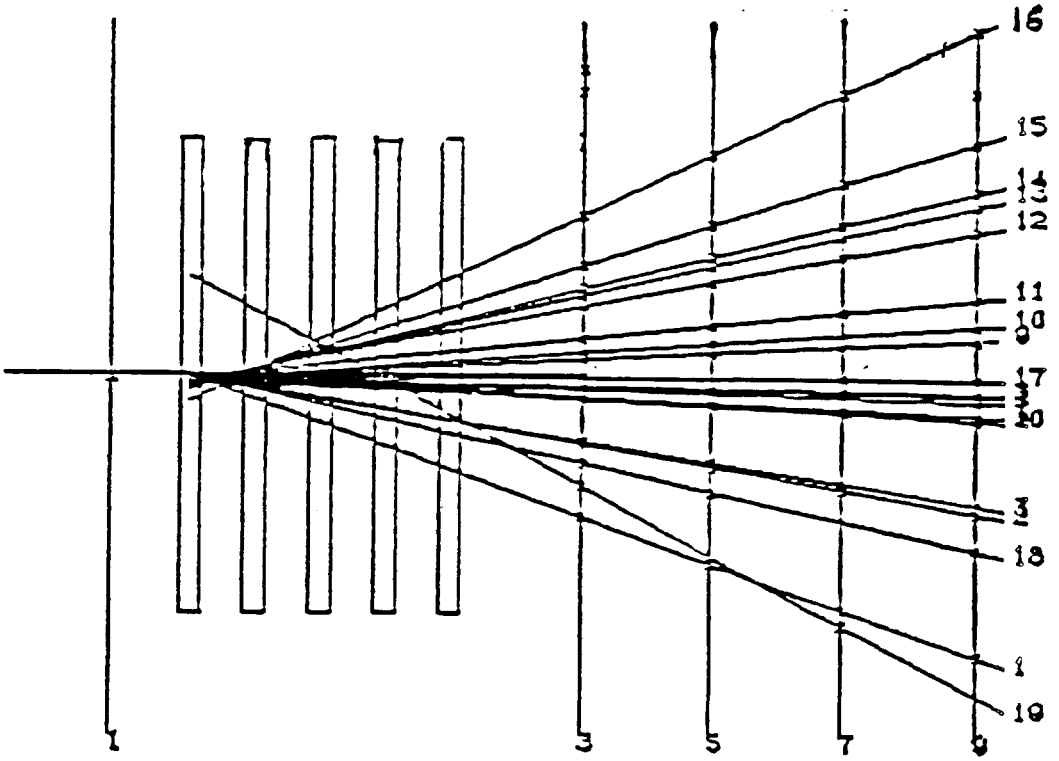

Figure V-10: An example of a reconstructed ISAJET event.

best ones based on a chi-square evaluation. These tracks are used to find and define a vertex. This process is repeated for tracks from three and two hits only. The algorithm is successful in finding the primary vertex with 95 % efficiency to within 2 mm. The efficiency for finding secondary vertices is about 40 %. These numbers can probably be improved upon in the future with the development of more sophisticated algorithms.

CHAPTER VI.
HEAVY QUARK PRODUCTION IN E706

A. INTRODUCTION

The existence of charm(c) and bottom(b) quarks has been experimentally established very firmly for about a decade. Most physicists believe that the discovery of the top quark is just around the corner. Both c and b quarks were first seen in the form of the bound states J/ψ ($c\bar{c}$) and Υ ($b\bar{b}$). Since then a lot of data has appeared, from e^+–e^- machines, on the production and branching ratios of the numerous other mesons containing heavy quarks. Very little is known about the baryonic bound states because they are not produced as often in e^+–e^- collisions. Over the last few years experiments [40, 41] have been done on photoproduction of charm which have yielded some excellent measurements on the life-times of heavy mesons. The production process here is also electromagnetic. The hadroproduction of heavy quarks is one area that is relatively not so rich in data. Some experiments[42, 43] have been done and some others are underway. Here one expects to see heavy baryons but the problem is one of dealing with immense backgrounds. One way of tackling this problem is to develop some efficient triggers based on fast reconstruction of mass from the decay products of the heavy quark. Another approach is one of collecting all the data and using some clever ways of sifting through it during the analysis. Here we look into the question of whether a high p_T photon can be used a trigger for studying the hadroproduction of heavy quarks.

This chapter summarizes the work which we have done to understand the heavy quark content of the away side jet in the expected E706 direct photon data. We also present results of a study of the heavy quark content of high p_T jets in general where one is not restricted to direct photon events. The study was motivated by the qualitative result that massive virtual gluons can be expected to fragment into heavy quark pairs a substantial fraction of the time. Since the annihilation diagram in direct

photon production involves the production of a virtual gluon opposite the direct photon as shown below, one expects that if the p_T of the direct photon is large, then the probability is enhanced that the mass of the away side virtual gluon will be large enough to yield heavy quark pairs ($c\bar{c}$) in an interesting fraction of the events.

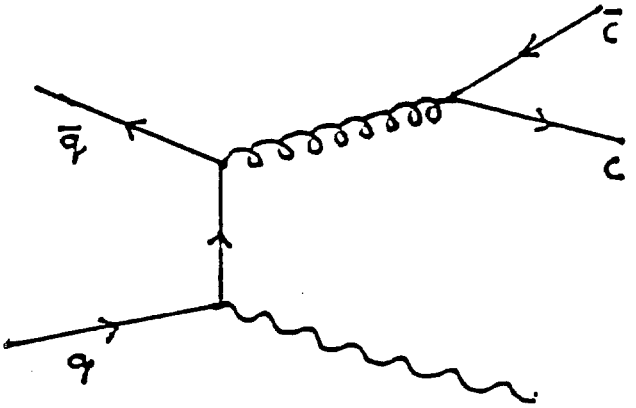

Figure VI-1: Annihilation graph for direct photon production. The fragmentation of the virtual gluon into heavy quark pairs will be enhanced if it has a large virtual mass.

In any case studying the fragmentation of gluon jets in the direct photon sample is certainly well within the physics purview of E706. We will first consider the theoretical basis on which the study rests and then present our Monte Carlo results from ISAJET.

B. THEORETICAL FOUNDATIONS

Fortunately gluon fragmentation into heavy quark pairs ($c\bar{c}$ and heavier) has been well studied theoretically. A good reference is the calculation by Mueller et al [43] Specifically the result from QCD is known including leading logarithmic QCD corrections. Leading non-perturbative corrections have been shown to be extremely small. If we define ρ = (number of $q\bar{q}$ pairs)/(number of gluon jets), then there exists a unique* and well defined QCD result (small theoretical uncertainty) for ρ as a

---

*The result does depend on the charm quark mass which we have taken to be 1.6 GeV and also on $\Lambda^2_{QCD} = 0.04\ GeV^2$ which is the ISAJET value.

function of the $M = (Q^2)^{1/2}$ of the virtual gluon. This prediction is shown in Figure VI-2. The two smooth curves correspond to a quark mass of zero (upper curve) and a more realistic c quark mass of 1.6 GeV (lower curve).

There remains the question of incorporating this physics into an appropriate Monte Carlo program. According to F. Paige (private communication), these results have been included in ISAJET ignoring only the mass dependence of the heavy quark which is (as we shall see) a relatively small effect. We have performed a detailed calculational check which we will now discuss.

For reasonably small Q^2 we can interpret the parameter ρ at a fixed Q^2 as the probability that a starting gluon with $M^2 = Q^2$ will produce a $c\bar{c}$ pair after it has completely fragmented.* Since we can tag the Q^2 of any starting gluon in the ISAJET Monte Carlo program, it is possible to compare the ISAJET program directly with the QCD calculation. Figure VI-2 also shows the ISAJET result for the parameter ρ as the program was received from F. Paige (which ignores the mass of the charmed quark). As one can see the ISAJET result with this approximation is reasonable but not in perfect agreement with the QCD result (M_c = 1.6 GeV). We decided to remove this approximation and Fig. VI-3 shows the improved ISAJET prediction which is now in agreement with the QCD result. This good agreement between ISAJET and the QCD result near threshold where we are obviously going to be most sensitive to it requires that the CUTJET parameter be set to the charm quark mass or 1.6 GeV which is well below the usual value of 6 GeV. The CUTJET parameter is the cut off mass at which the evolution of final state partons stops. It is similar in nature to the factorization scale M in parton model calculations. Setting it to 1.6 GeV brings us into the regime of very low Q^2 values. This means that the program will not generate the right final state hadron multiplicities but it can be used reliably as a means of generating the heavy quark ($c\bar{c}$) content of jets arising from a single gluon.

---

*We are assuming that the probability ρ is small enough that only one $c\bar{c}$ pair is likely to be produced in the course of the fragmentation process.

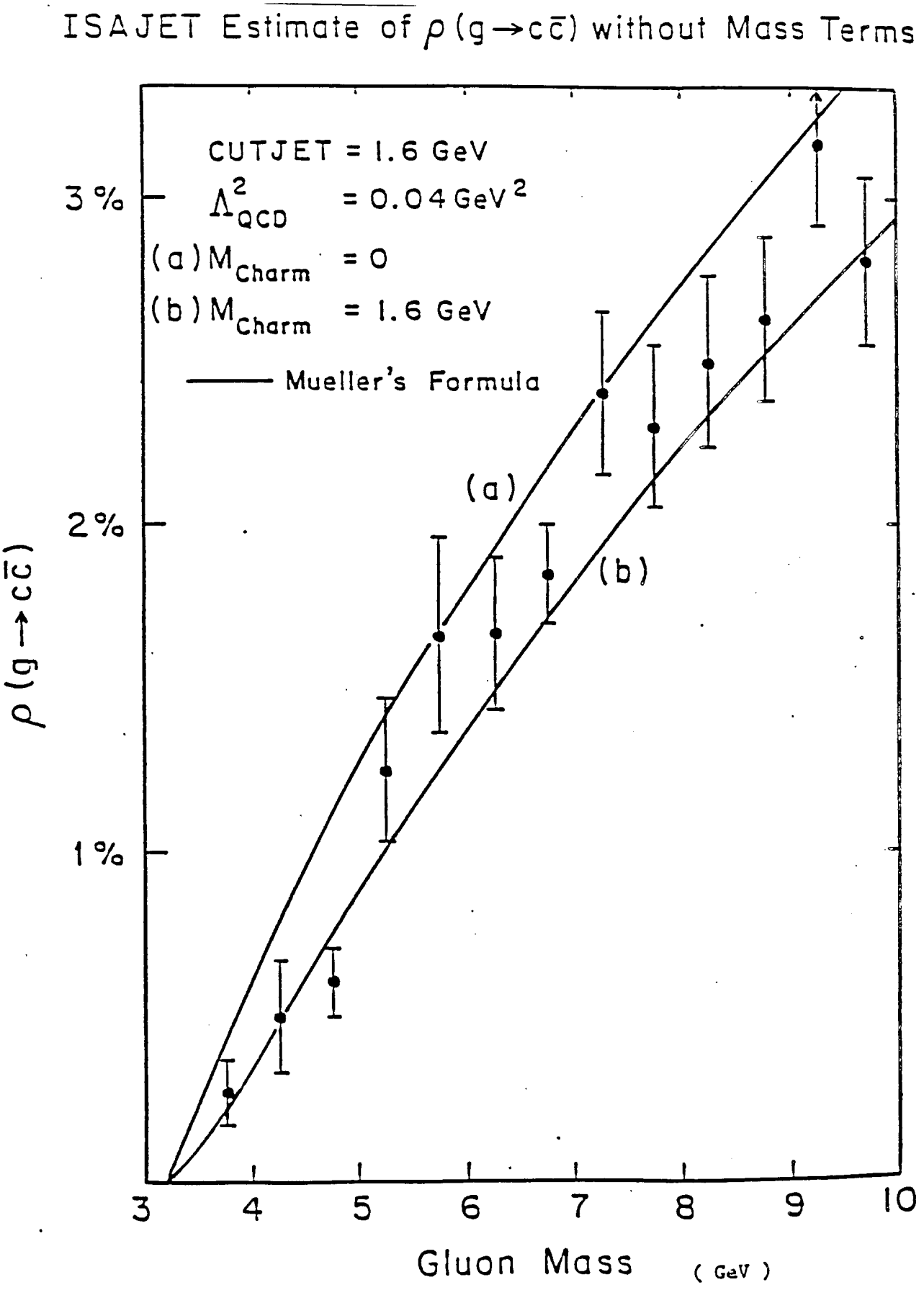
ISAJET Estimate of ρ(g→cc̄) without Mass Terms
CUTJET = 1.6 GeV
Λ²QCD = 0.04 GeV²
(a) M Charm = 0
(b) M Charm = 1.6 GeV
Mueller's Formula
(a)
(b)
3 %
2 %
1 %
ρ(g→cc̄)
3
4
5
6
7
8
9
10
Gluon Mass (GeV)

Figure VI-2:

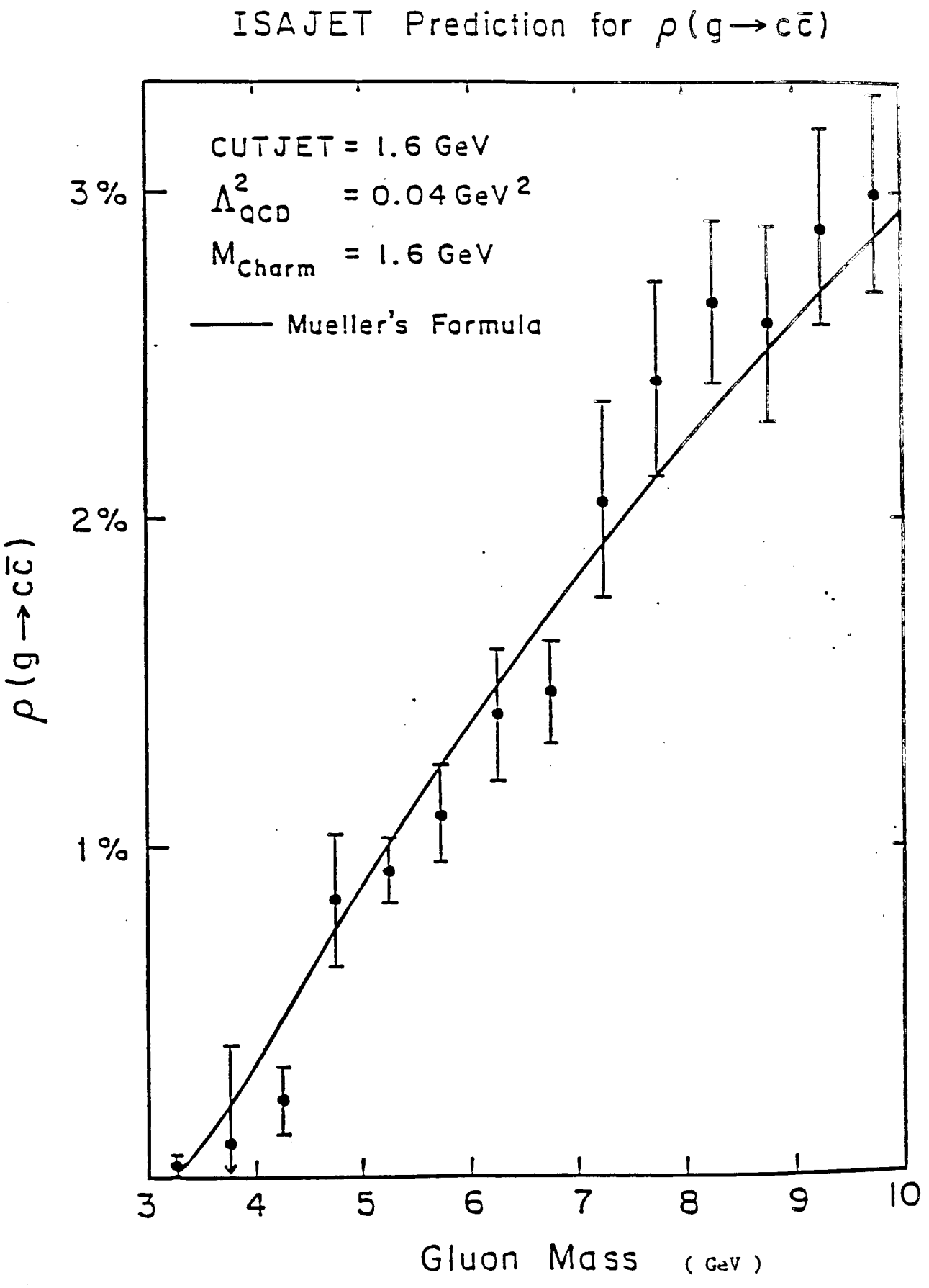
ISAJET Prediction for ρ(g→cc̄)
CUTJET = 1.6 GeV
Λ²QCD = 0.04 GeV²
MCharm = 1.6 GeV
Mueller's Formula
3%
2%
1%
ρ(g→cc̄)
3
4
5
6
7
8
9
10
Gluon Mass (GeV)

Figure VI-3:

C. MONTE CARLO RESULTS

For the annihilation graph, we have calculated the fraction of the events for which the away side gluon jet contains charm. This fraction is plotted as a function of the p_T of the direct photon in Fig. VI-4. These results can be folded with the expected yield of direct photon events in the annihilation channel* to estimate the charm sample in our data. We estimate that for 50,000 direct photon events with p_T above 5 GeV/c in the annihilation channel we can expect 360 events to contain charm.** If about half of the events are in the annihilation channel for $\pi^- C$ running, it would appear that we may have a small but recognizable sample of charm events.

On comparing Figures VI-3 and VI-4 one can notice that the fraction of events containing a $c\bar{c}$ pair is smaller when plotted against the p_T of the real photon than when plotted versus the mass of the virtual gluon. This is a direct consequence of the kinematics involved in the gluon fragmentation and also of the general problem in QCD *** of relating the gluon Q^2 to its p_T. In the absence of a priori knowledge, the usual way is to equate $Q^2 = fp_T^2$, where f is a fraction between one and two. In the program, however, one starts by putting Q^2 = (energy)^2 and then allowing the Q^2 to degrade in the final state evolution. In the fragmentation process, the p_T carried off by the $c\bar{c}$ pair ends up being less than the original value for the gluon because part of the energy is used up in creating the heavy quark masses. This results in the program lowering the photon p_T as well in order to conserve p_T. This lowering implies that any given p_T bin in Figure VI-4 is fed by bins higher in p_T. Since the production cross-section of the photons falls very rapidly with p_T, the charm fraction also falls with it. These questions of slight differences are not too important because our intent was to simply get a rough estimate and none of these details tend to change the numbers drastically.

---

* The fraction of $c\bar{c}$ pairs associated with the Compton graph is approximately 0.2% for p_T between 5 and 10 GeV/c.

** The number of charm events for p_T between 3 and 5 GeV/c is also about 360.

*** A suggested way of reducing the error is to minimize the effect of the free parameters in QCD[45]. It is not clear if such proceedures are valid, especially in the range of Q^2 values we expect in E706.

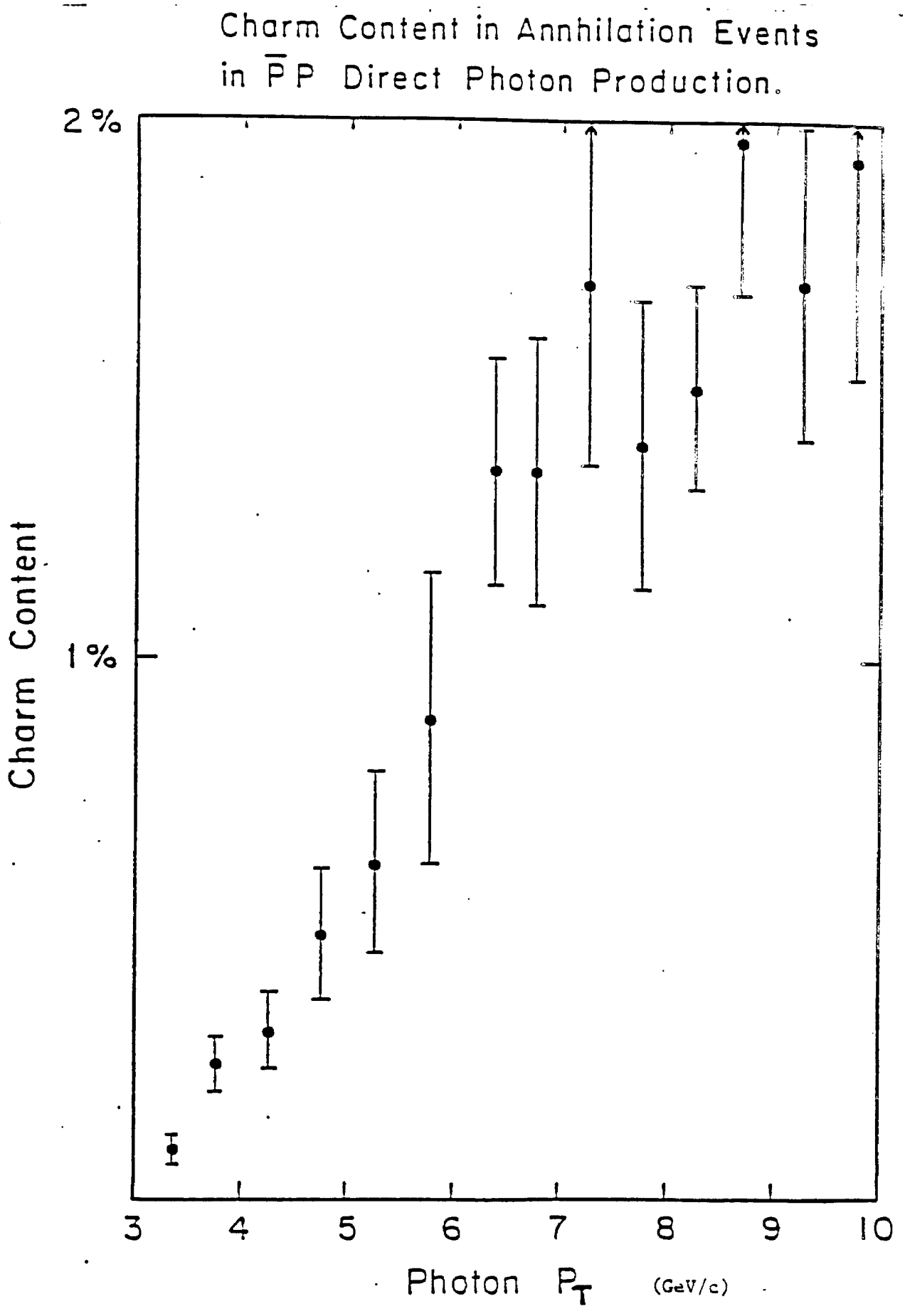
Charm Content in Annhilation Events
in $\bar{P}P$ Direct Photon Production.
2%
1%
Charm Content
3
4
5
6
7
8
9
10
Photon P_T (GeV/c)

Figure VI-4:

D. HIGH P_T JETS

We have also considered the heavy quark content of high p_T jets in the general class of two jet events. The two jet production cross section as a function of jet p_T for $s^{1/2}$ = 40 Gev is shown in Fig. VI-5. We have broken down the contributing processes for $p\bar{p}$ collisions in Fig. VI-6. The diagrams labeled (a) are those which produce a $q\bar{q}$ pair in the final state. The $q\bar{q}$ pair will occasionally be $c\bar{c}$ or $b\bar{b}$ Diagrams labeled (b) correspond to two gluons either of which can make a heavy quark pair ($c\bar{c}$). Diagram (c) is a Compton process where the final gluon can fragment into $c\bar{c}$ and (d) corresponds to qq scattering where one of the quarks can be a heavy quark (c) from the sea. Although all of these processes can make bottom, in practice only those labeled (a) have enough energy to be important. The fraction of the time the processes (a) and (b) have charm (bottom) is shown in Figures VI-7 and VI-8. Again one sees that the the heavy quark content increases as the p_T of the jet increases.

These results may provide some physics basis for developing the triggering in the hadron calorimeter as well as developing a more sophisticated lepton trigger. In any case the yield of heavy quark events is clearly larger than in the direct photon case primarily because the production cross section is larger.

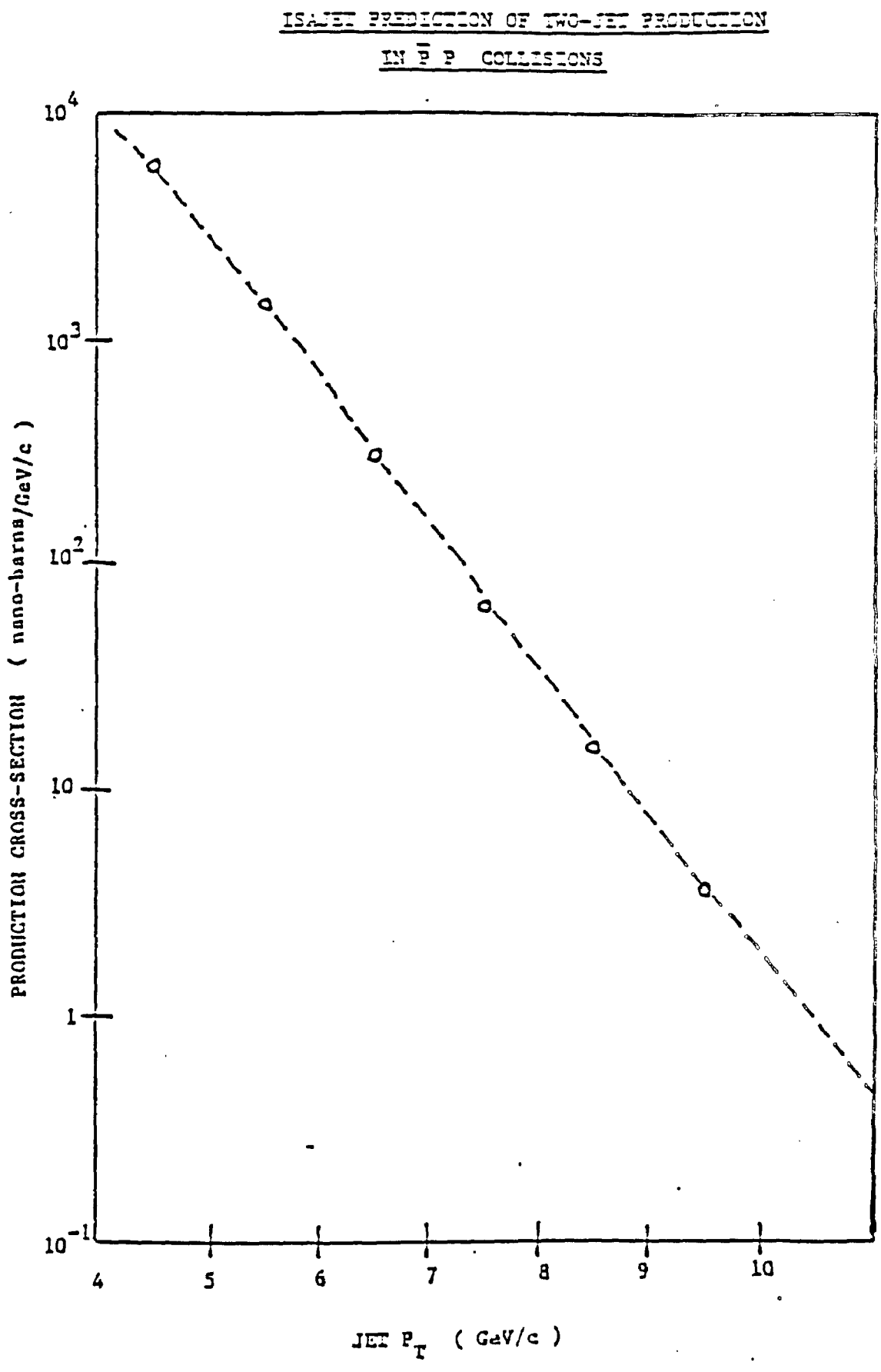
ISAJET PREDICTION OF TWO-JET PRODUCTION
IN $\bar{P}$ P COLLISIONS
PRODUCTION CROSS-SECTION (nano-barns/GeV/c)
10^4
10^3
10^2
10
1
10^{-1}
4
5
6
7
8
9
10
JET P_T (GeV/c)

Figure VI-5:

CONTRIBUTION OF VARIOUS QCD PROCESSES TO TWO-JET PRODUCTION

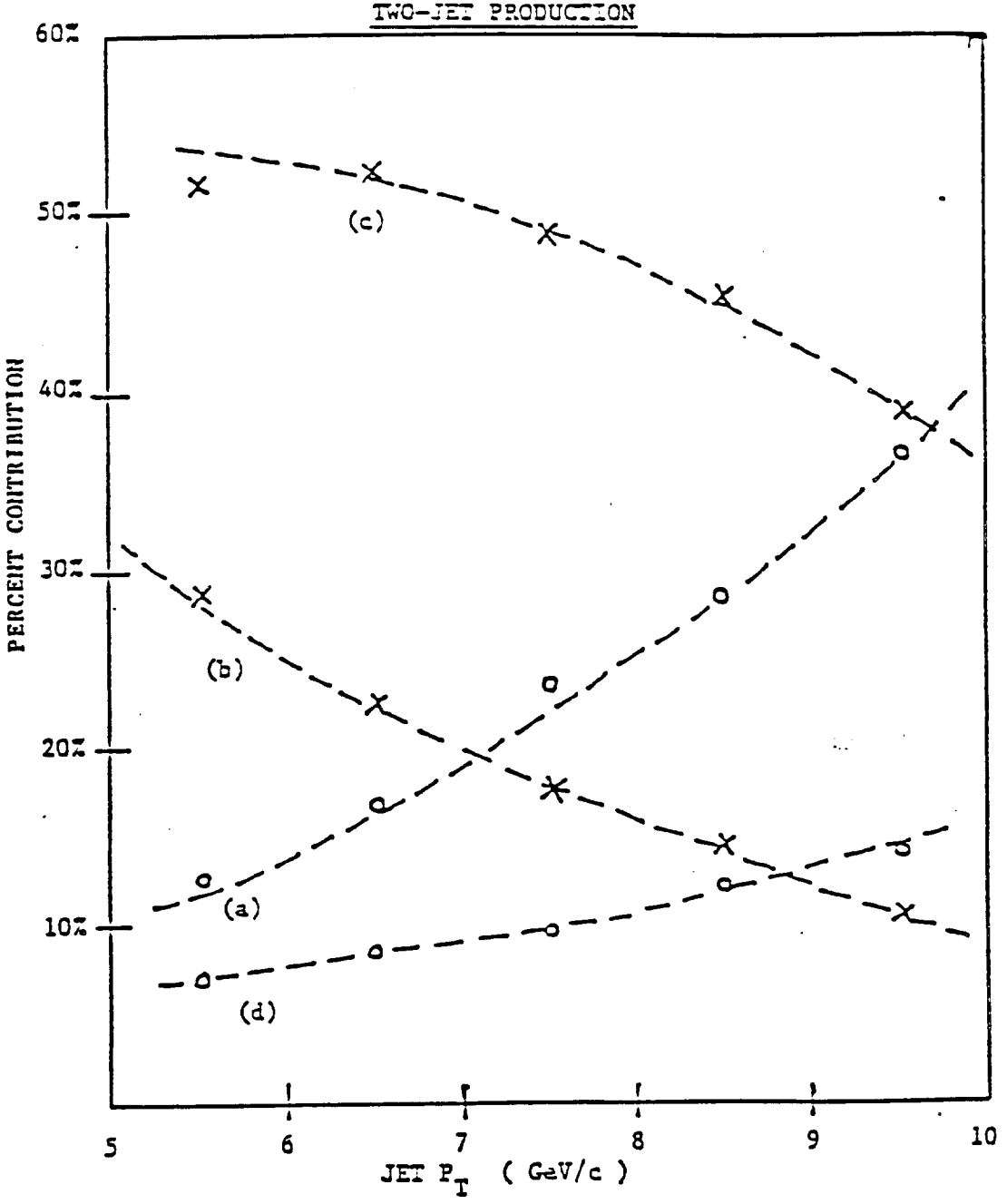

QCD Processes:

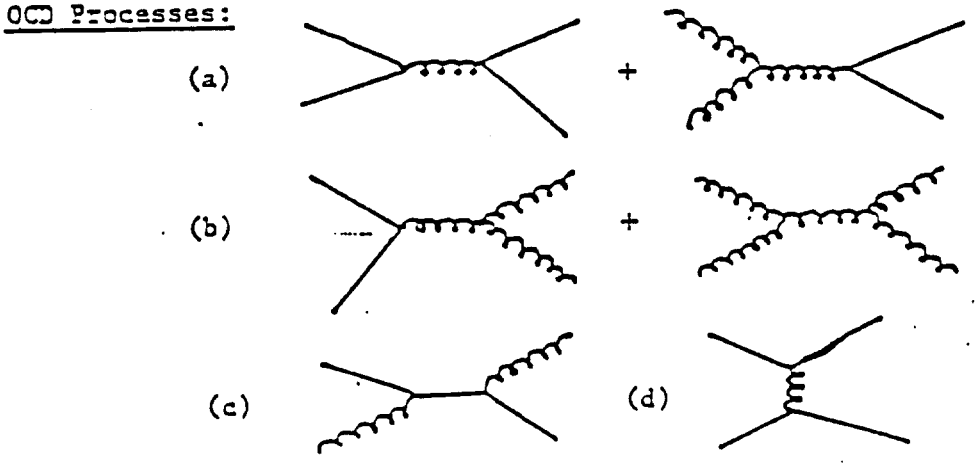

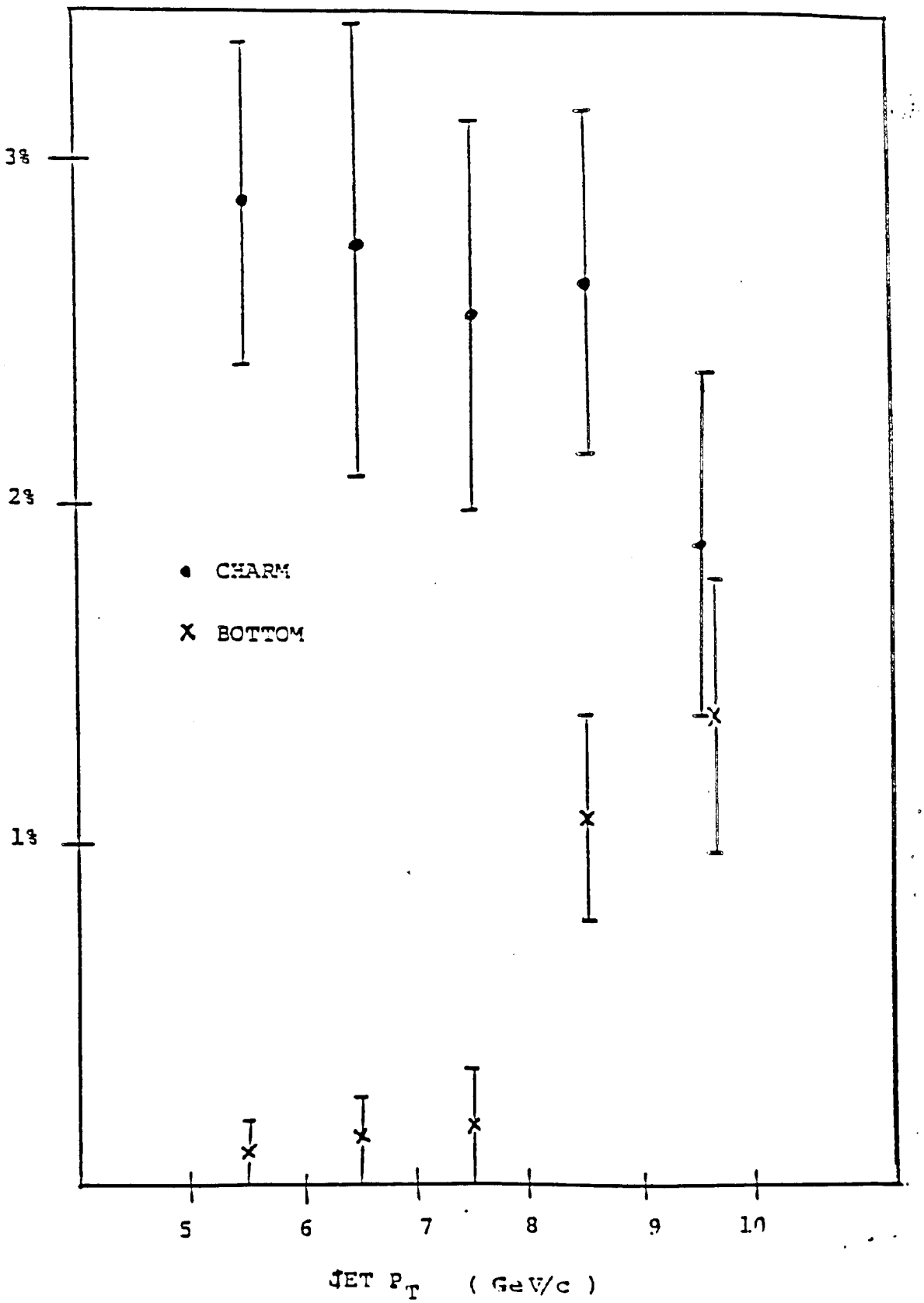

Figure VI-7: The heavy quark content of the process (a) of Figure VI-6.

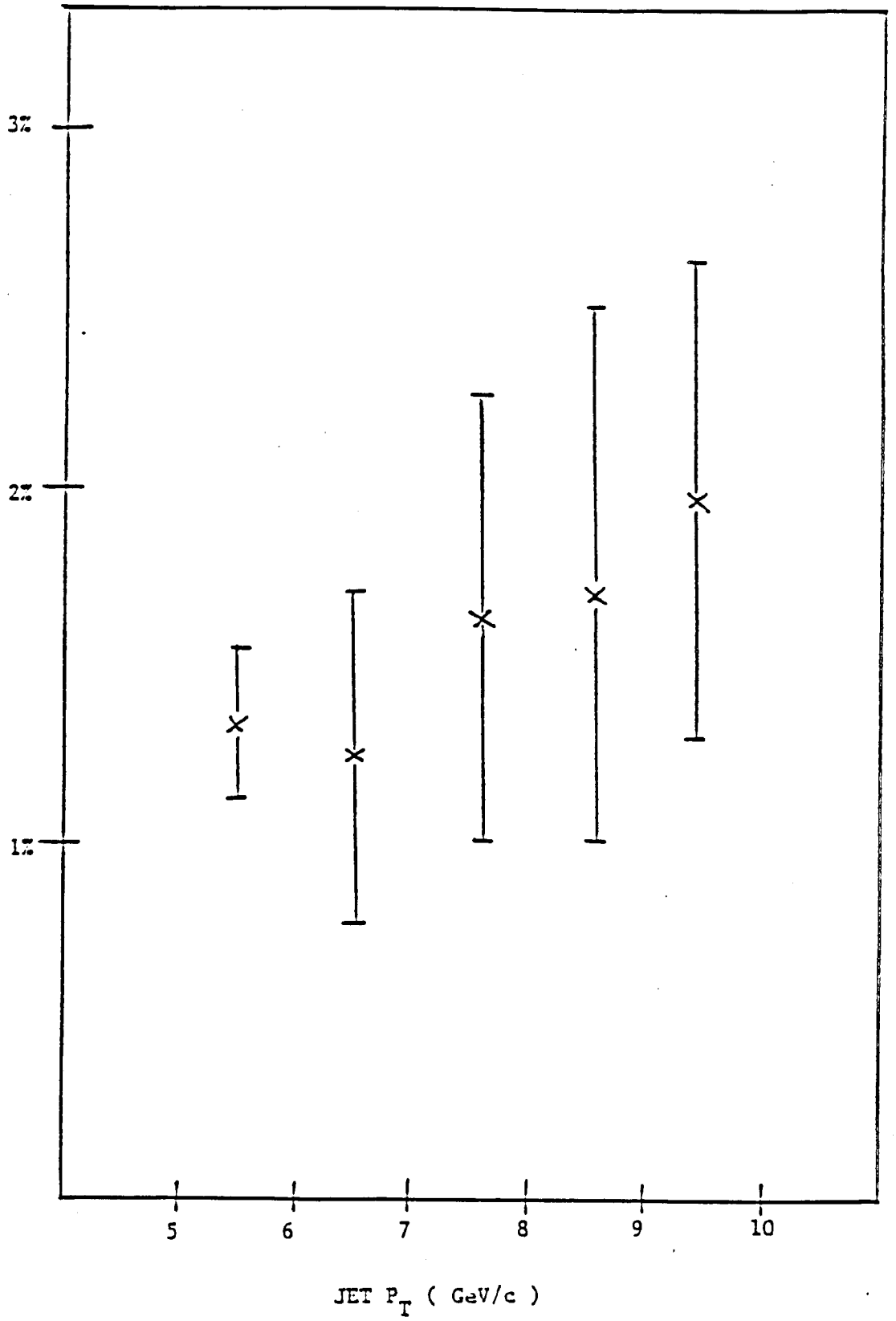

Figure VI-8: The heavy quark content of the process (b) of Figure VI-6.

CHAPTER VII.
CONCLUSION

The main thrust of this thesis has been the instrumentation of a Silicon Strip Microvextex detector system[46]. This system will be used as the front-end in the E706 spectrometer at Tevatron II. The design, construction and testing of the system have been successfully carried out[47].

Direct photons were shown to be a simple and unique test of QCD. The study of the accompanying jets should prove to complement the existing data on QCD jets. It was demonstrated that an SMD system was the ideal choice for the front-end of E706.

The approach that we took was one of developing the techniques, that were necessary for the instrumentation, in our lab at the University of Pittsburgh. A modular design was drafted that was flexible enough to allow for the use of commercial products as well. The final assembled version is a good mix of commercial and home-grown components. We were successful in making fine-line PC boards that were used for the fan-out. This effort included the development of a computer-aided design system for making the masks. The X-Y modules were assembled with the use of interconnection schemes developed by us.

The sources of noise in amplifiers were analyzed. The noise levels in various circuits were evaluated and the preamp most suited for our application was selected. A S/N ratio of > 20 was achieved. These preamps were successfully interfaced to a digital read-out system. An instrumentation scheme for 6,600 channels of these circuits was designed. Special care was taken to achieve immunity from rf interference. Tests with an electron source on an X-Y module showed an efficiency of nearly 100 % and an average background level of the order of 10^{-4}.

The ISAJET program was adapted for simulating direct photon events. Studies

based on these events have predicted a Δz resolution of < 2 mm with a 95 % efficiency for finding the primary vertex. The rate capability of the system was shown to be well above the expected rates in E706. Monte Carlo studies were also made to estimate the production of heavy quarks in the away-side jet. The charm content was shown to be small but not negligible. The overall production of charm should be substantial but it requires the development of a sophisticated trigger. This is an area of Physics that we look forward to studying in the future.

APPENDIX A.

THE E706 LIQUID ARGON CALORIMETER

This appendix consists of a reprint of a paper published in Nuclear Instruments and Methods (NIM). The design of the LAC is described in detail.

Nuclear Instruments and Methods in Physics Research A235 (1985) 332–337
North-Holland, Amsterdam

A LARGE LIQUID ARGON PHOTON/HADRON CALORIMETER FOR FNAL

F. LOBKOWICZ, G. BALLOCCHI, G. CHANDLEE, W. DESOI, G. FANOURAKIS, T. FERBEL, P. GUTIERREZ, J. HUSTON, A. LANARO, J. MANSOUR, N. MATHUR, D. SKOW and P. SLATTERY

University of Rochester, Rochester, USA

C. GUPT, A.N. MITRA and R.K. SHIVPURI

University of Delhi, Delhi, India

W. BAKER, D. BERG, D. CAREY, T. DROEGE, D. EARTLY, H. JOHNSTAD, A. LENNOX and C.A. NELSON Jr

Fermi National Accelerator Laboratory, USA

C. BROMBERG, D. BROWN and R. MILLER

Michigan State University, Michigan, USA

K. HELLER, S. HEPPELMANN, T. JOYCE, M. MARSHAK, E. PETERSON, K. RUDDICK and M. SHUPE

University of Minnesota, Minnesota, USA

G. ALVERSON, W. FAISSLER, D. GARELICK, M. GLAUBMAN, S. HOSSAIN and E. POTHIER

Northeastern University, USA

G. SMITH and J. WHITMORE

Pennsylvania State University, Pennsylvania, USA

W.E. CLELAND, D. COON, E. ENGELS Jr, S. MANI, P.F. SHEPARD and J.A. THOMPSON

University of Pittsburgh, Pittsburgh, USA

This paper describes a new liquid argon photon/hadron detector currently under construction for Experiment E706 at the Fermi National Accelerator Laboratory.

Fermilab experiment E706 has its main thrust as the measurement of direct photon yields in the p_T range of 5–10 GeV/c, with incident π/K/p beams at 500–1000 GeV/c, as well as the study of associated jets produced in such reactions. In addition, the experiment will measure the production of high mass ($m \gtrsim 3$ GeV) e^+e^- and $\gamma\gamma$ states.

Fig. 1 shows the overall layout of the experiment, which is designed to cover as much of the overall solid angle as possible. The target is surrounded by an array of solid state strip detectors of 50 μ pitch. These, together with proportional chambers downstream of the magnet, determine the charged particle momenta; in addition, they are used as a vertex detector, thereby providing a degree of separation between primary and secondary interactions in the segmented target.

A large liquid argon calorimeter (LAC) measures the position and energy of both photons/electrons and hadrons. It has a central hole of 40 cm diameter; this area is covered by a forward steel/plastic scintillator calorimeter. In the ensuing, we discuss only the characteristics of the LAC.

0168-9002/85/$03.30 © Elsevier Science Publishers B.V.
(North-Holland Physics Publishing Division)

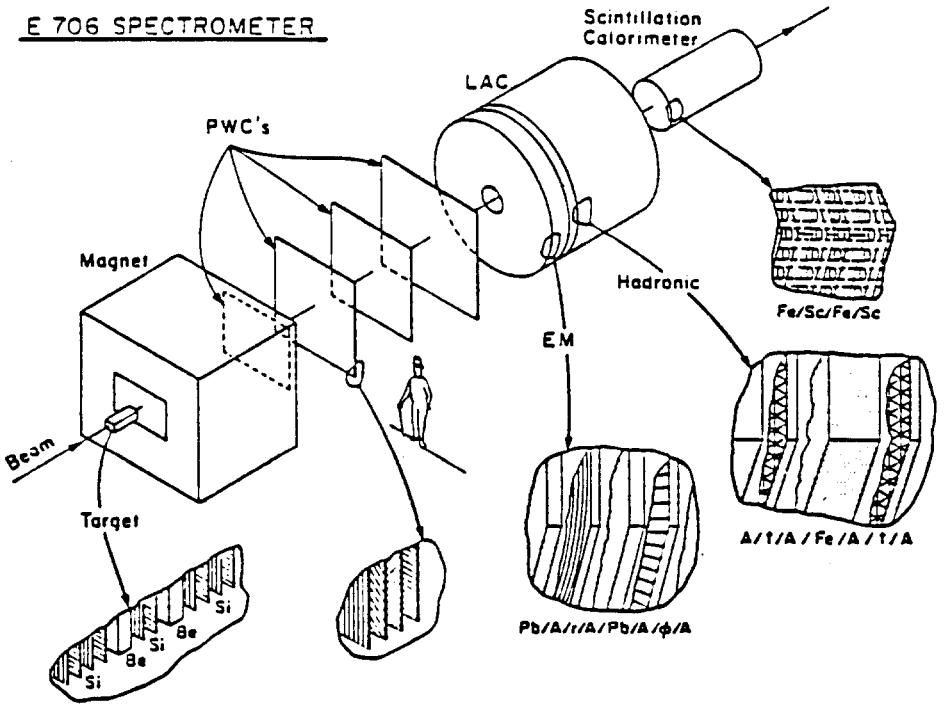

Fig. 1. The layout of the complete E706 spectrometer showing the target surrounded by silicon strip detectors, the PW's following the magnet, the Liquid Argon Calorimeter and the forward scintillation calorimeter.

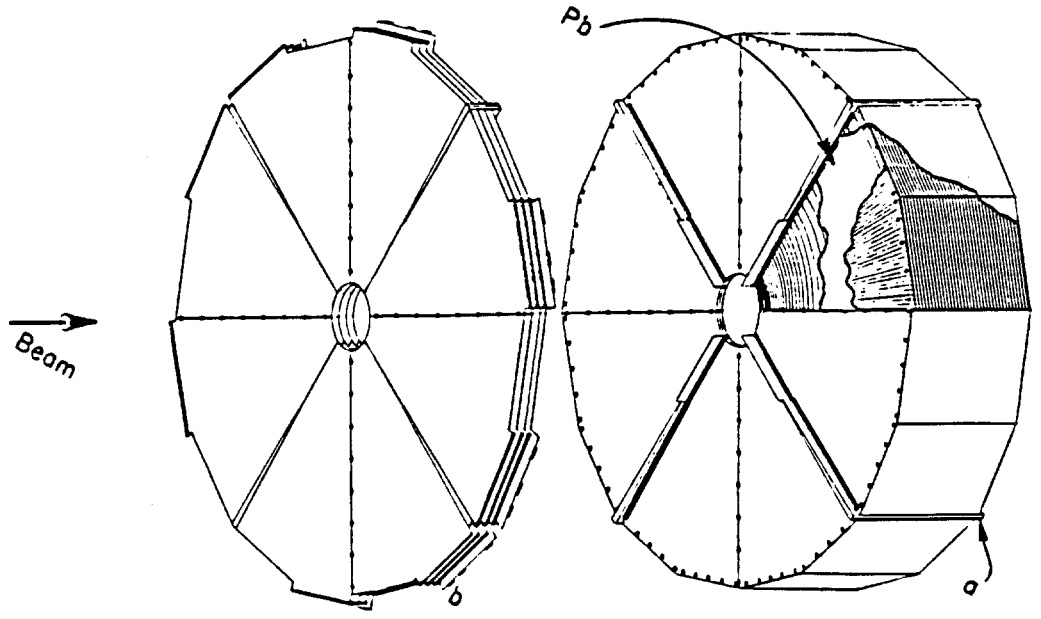

Fig. 2. A blowup of the photon detector. The quadrants are separated by stainless steel plates (a); special boards (b) connect individual readout strips to connectors along the circumference.

In a series of previous Fermilab experiments that concerned radiative decays of mesons and direct photon production, our group used a LAC of 0.9×1.4 m^2 area to measure photon energies and directions [1]. Based on this experience, we are presently constructing a larger LAC for the detection of both photons and hadrons. The specifications are as follows:

(i) Nearly complete coverage at laboratory angles 22 mrad $< \theta <$ 160 mrad for both photons and hadrons. At an incident momentum of 500 GeV/c, this corresponds to an angular range of $40° < \theta_{cm} < 138°$, or $\sim 77\%$ of the total 4π solid angle.

(ii) Energy resolution of $< 15\% E^{1/2}$, and a positional resolution of < 0.1 cm for photons/electrons.

(iii) Good separation of isolated photons from photon pairs from π^0 decay up to energies of ~ 250 GeV.

(iv) Hadron energy resolution of $\lesssim 70\% E^{1/2}$, with a position resolution of a few centimeters.

(v) Electron/hadron separation at the 10^{-4} level.

(vi) Ability to sustain an interaction rate of $\gtrsim 10^6$ Hz.

The LAC has two separate parts: a photon detector and a hadron detector, in a common cryogenic enclosure. The photon detector (fig. 2) is subdivided into four mechanically independent quadrants, held together by the overall support structure. Each quadrant consists of 66 layers in which 2 mm lead plates are separated by 2.5 mm gaps of liquid argon from G-10 readout boards. Alternate boards are used to read out the r coordinate and the ϕ coordinate in a polar coordinate system. The r coordinate readout consists of 256 concentric radial strips in each octant: the strips are focused in tower-like fashion towards a target 9 m in front of the detector. The ϕ coordinate strips are subdivided into inner and outer segments: each inner strip subtends an azimuthal angle of 16.4 mrad, while each of the outer strips covers an angular range of 8.2 mrad. The separation between inner and outer ϕ-strips corresponds to a laboratory angle from the target of 56 mrad, or a c.m. angle of 85° at an incident momentum of 500 GeV/c. Each lead plate is connected to two 100 nF capacitors in parallel [2]; the capacitors have a leakage current of $< 10^{-10}$ A at 9 kV, both at room and at cryogenic temperatures (even after many cooling cycles).

The support structure of each quadrant, as well as the additional space needed for readout connectors and G-10 spacers (to separate the boards from each other and from the lead), produce dead areas both for incident photons and hadrons. We assume that a hadron is "lost" (that is, its energy cannot be measured to any reasonable accuracy) if it hits the stainless steel support plates. A hadron going through the G-10 spacers encounters only ~ 1 absorption length of material and its energy can consequently still be measured downstream, albeit with reduced accuracy. On the other hand, any photon hitting the G-10 spacers (and thus missing the lead plates) will not be detected. Fig. 3 indicates the loss in the fractional azimuthal coverage as a function of c.m. angle for a beam energy of 510 GeV/c.

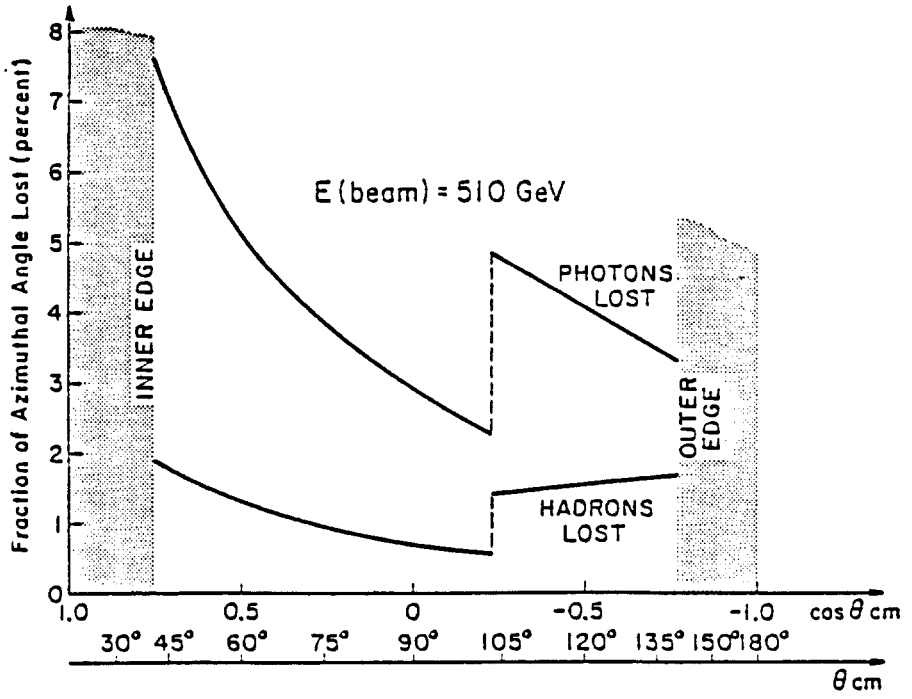

Fig. 3. The azimuthal extent of the dead regions produced by the support structure for photons and hadrons.

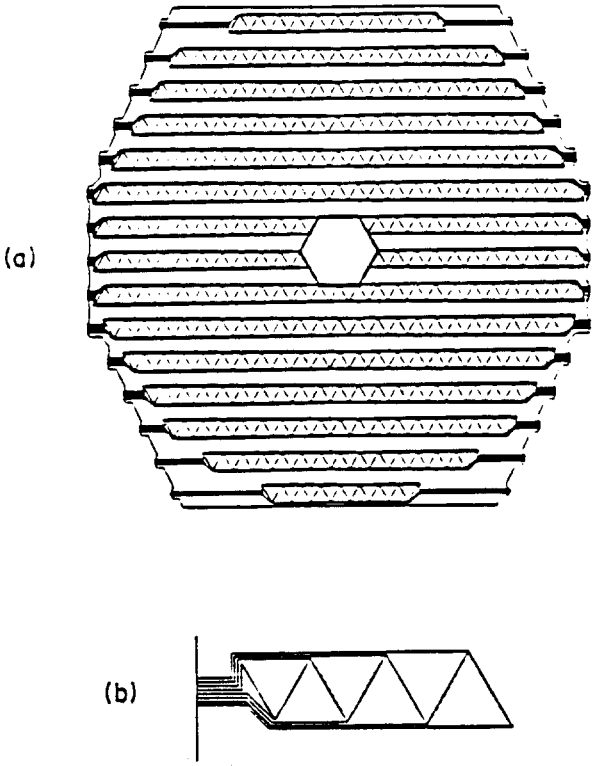

Fig. 4. (a) A single hadron calorimeter readout board: (b) detail of the readout scheme.

There are two sets of three special "readout boards," one in front and one in the back of the photon detector assembly; one of these triplets is shown in the exploded view of fig. 2. These provide leads from the inner ϕ strips as well as from the r strips to the outer edge of the detector where external cables are connected to the detector. The first $\frac{1}{3}$ of the detector (22 layers, 10 radiation lengths) is read out via the front readout boards, the last $\frac{2}{3}$ (44 layers, 20 r.l.) is read out via the back readout planes.

In contrast to the photon detector, the hadron detector has a tower readout structure. Each tower consists of a series of triangular readout pads, as illustrated in fig. 4. The need to have electrical connections from each pad to the edge of the detector necessitates the subdivision of readout planes into pairs, one of which is shown in fig. 4. Each of the readout planes covers one-half of the area with pads, leaving the space between two rows for the readout lines. As illustrated in fig. 5, during assembly, the readout lines are covered with horizontal spacer strips which are glued to the readout boards and provide mechanical stability. Since only 4 ft × 12 ft G-10 boards are available commercially, each plane consists of three such boards. Vertical ribs hold the individual boards together and add to the rigidity of the whole assembly. Each layer (fig. 5b) has in sequence a H.V. board, a layer of horizontal strips that define the 3 mm argon gap and shadow half of the area of the pads,

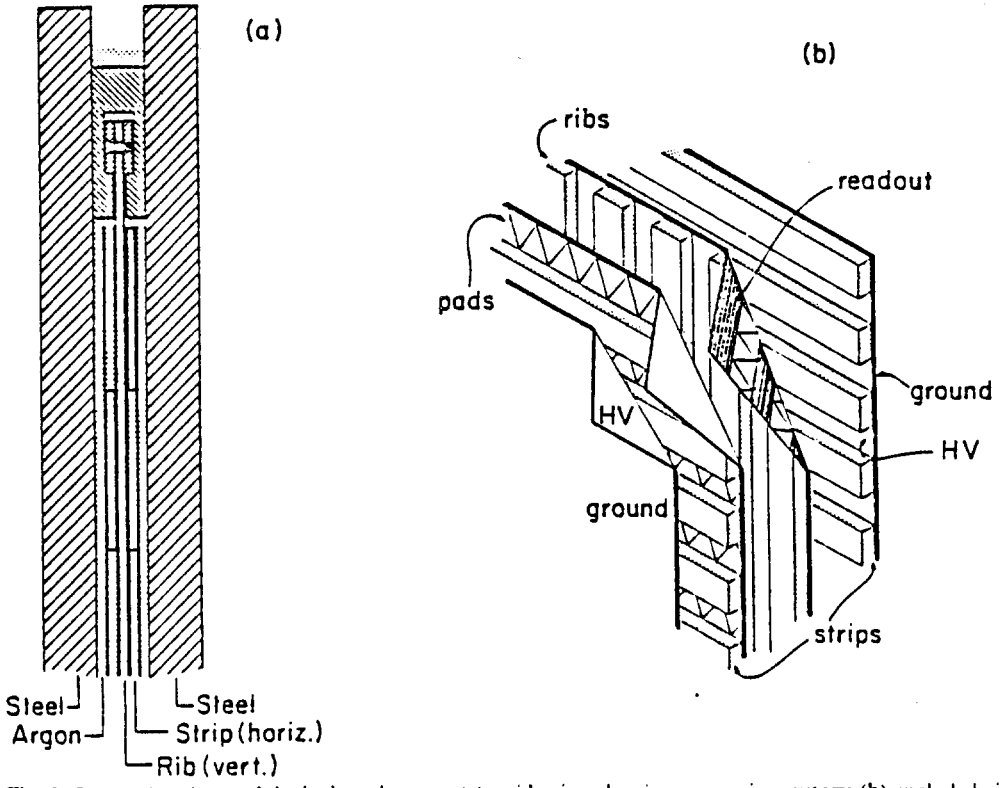

Fig. 5. One readout layer of the hadron detector: (a) a side view showing suspension system; (b) exploded view of one readout layer.

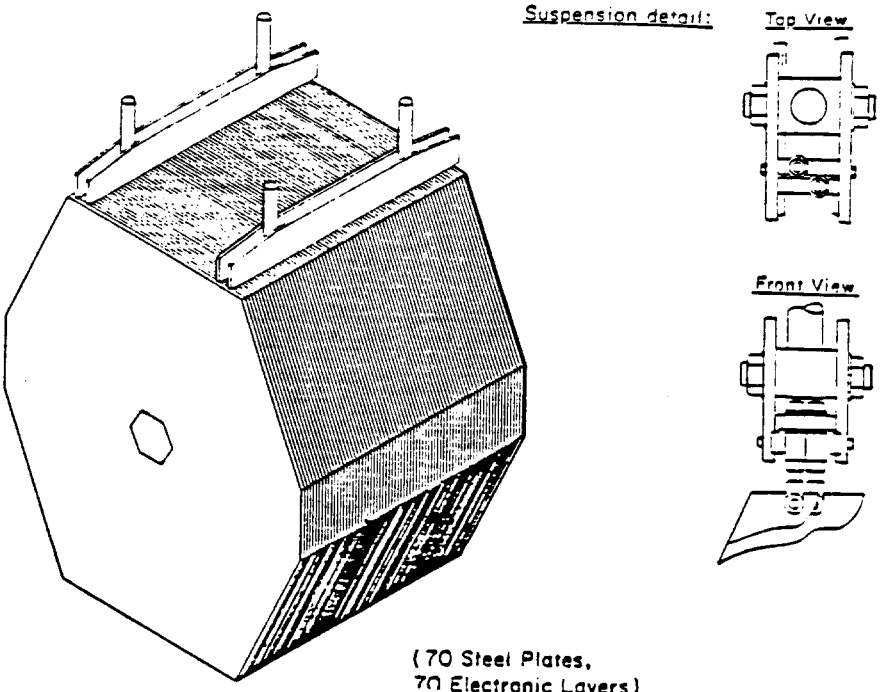

Fig. 6. The assembly of the hadron calorimeter. The detail shows the suspension system for individual steel plates.

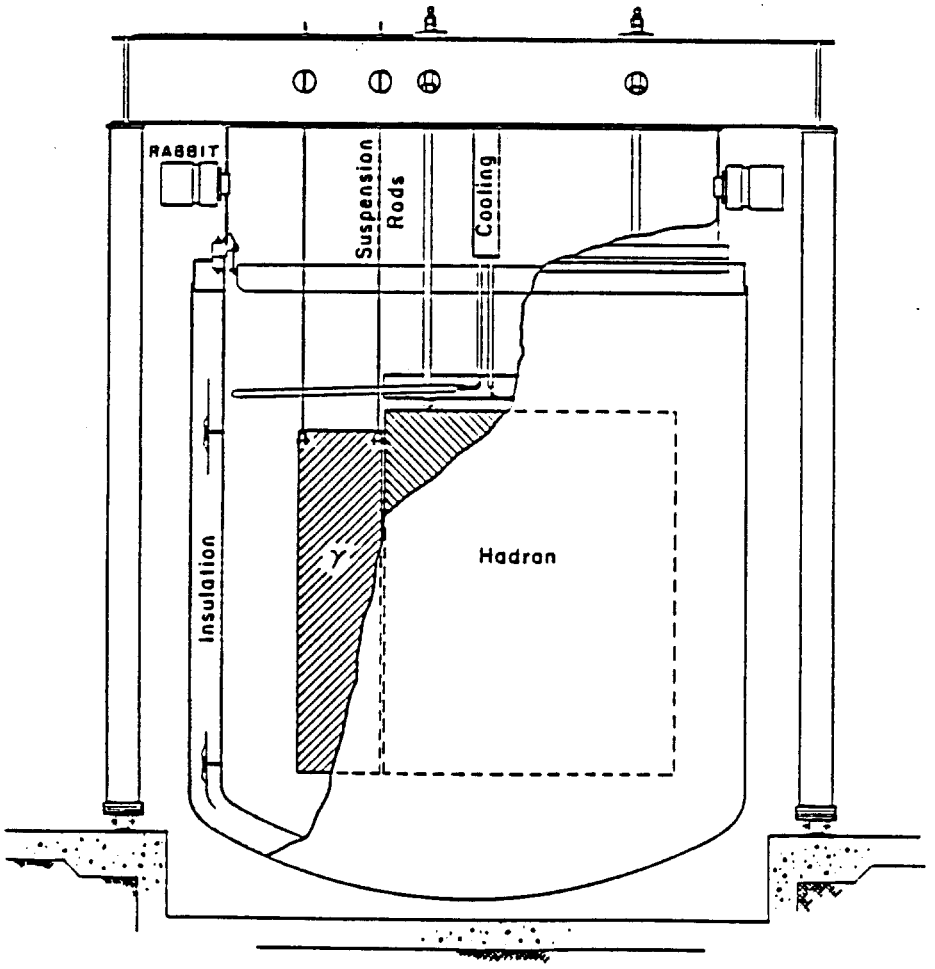

Fig. 7. The overall gantry and cryostat of the LAC. The beam is incident from the left. The region inside the cryostat in front of the photon detector ("γ") is filled with low density material.

one pad board, a layer of vertical ribs, the second shifted pad board, another layer of horizontal strips, and finally a second H.V. board. Each H.V. board consists of three joined double-sided $\frac{1}{32}$" thick copper-clad G-10 boards, with the outer side grounded. This provides a blocking capacitance of 70 nF for each plate, which minimizes crosstalk between pads.

There are 70 layers in the hadron calorimeter, each consisting of a $\frac{1}{4}$" thick steel plate and one readout assembly, for a total of 7 absorption lengths. The readout of each tower is divided once in depth for a total of 2500 readout channels. Both the photon and the hadron detector are suspended from the cover plate of a 17 ft diameter upright cylindrical cryostat as shown in fig. 6. The cover plate with its reinforcing beams forms the top of a gantry which can be moved on rails perpendicularly to the beam direction (fig. 7). This horizontal motion, together with a beam which can be swept vertically, will provide capability for sweeping the beam across any portion of the calorimeter for calibration and testing.

For assembly and for servicing the detectors, the foam insulated cryostat can be lowered into a special pit inside the detector building. The cover plate has a short vertical cylindrical attachment, from which the amplifier crates (RABBIT) are suspended. Each amplifier card has 16 channels; each channel consists of a low noise integrating amplifier, a fast output used for trigger purpose, a 800 ns delay line and a dual ADC sample/hold circuit which samples the pulse train before and after the event of interest (the amplifier and readout system is conceptually identical to the system described in ref. [3]). In addition, four neighboring channels are added and fed into a TDC sample/hold circuit for timing purposes. The readout ssytem follows the RABBIT protocol used for the Fermilab Colliding Detector Facility [4].

The detector is presently under construction and will start operation in the spring of 1986.

References

[1] C.A. Nelson Jr et al., Nucl. Instr. and Meth. 216 (1983) 381.
[2] CER1A4642SP, manufactured by Custom Electronics, Oneonta, NY, USA
[3] T.F. Droege, F. Lobkowicz and Y. Fukushima, IEEE Trans. Nucl. Sci. NS-25 (1978) 687.
[4] T.F. Droege, K.J. Turner and T.K. Ohska, RABBIT System Specifications, Fermilab note PIN521/CDF119 (1982).

APPENDIX B.
MASK MAKING FOR PC BOARDS

In this appendix we describe a software system developed for designing high resolution masks for PC boards. The same system was used to design other masks that had conventional densities but required high precision in alignment. These masks also required a large number of plated-through holes. This in turn needed software to compute the commands for a digitally controlled drilling machine. This was also accomplished using the same system. The programming was done entirely in FORTRAN.

High resolution PC board masks are made on digitally controlled photoplotters. These are commercially available devices that have a movable collimated light source which exposes a photographic film. The movements of the light source are similar to that of an X-Y plotter using a set of stepping motors. The motors have a least movement of typically a fraction of a milli-inch. The digital control is achieved in terms of the number of pulses sent to a particular motor resulting in the same number of steps moved. Hence, each movement of the light source is in terms of incremental X-Y coordinates. In addition to precision in movement, we need high resolution in the pattern definition. The photoplotters support a variety of collimators that are mounted on a rotating wheel. These can be placed under the light source using digital commands also. These collimators allow one to expose the film with thin traces as well as other shapes used in printed circuits. In order to obtain sharp edges on the pattern, the intensity of the light source is controlled and a number of filters are used. The movement of the source involves accelerations and deccelerations resulting in areas that receive longer exposures. This is compensated for by dimming the intensity at a proportional rate. A certain amount of expertise is required in achieving the desired performance from these machines and we were fortunate in locating an industrial house that had it.

Figure B-1:

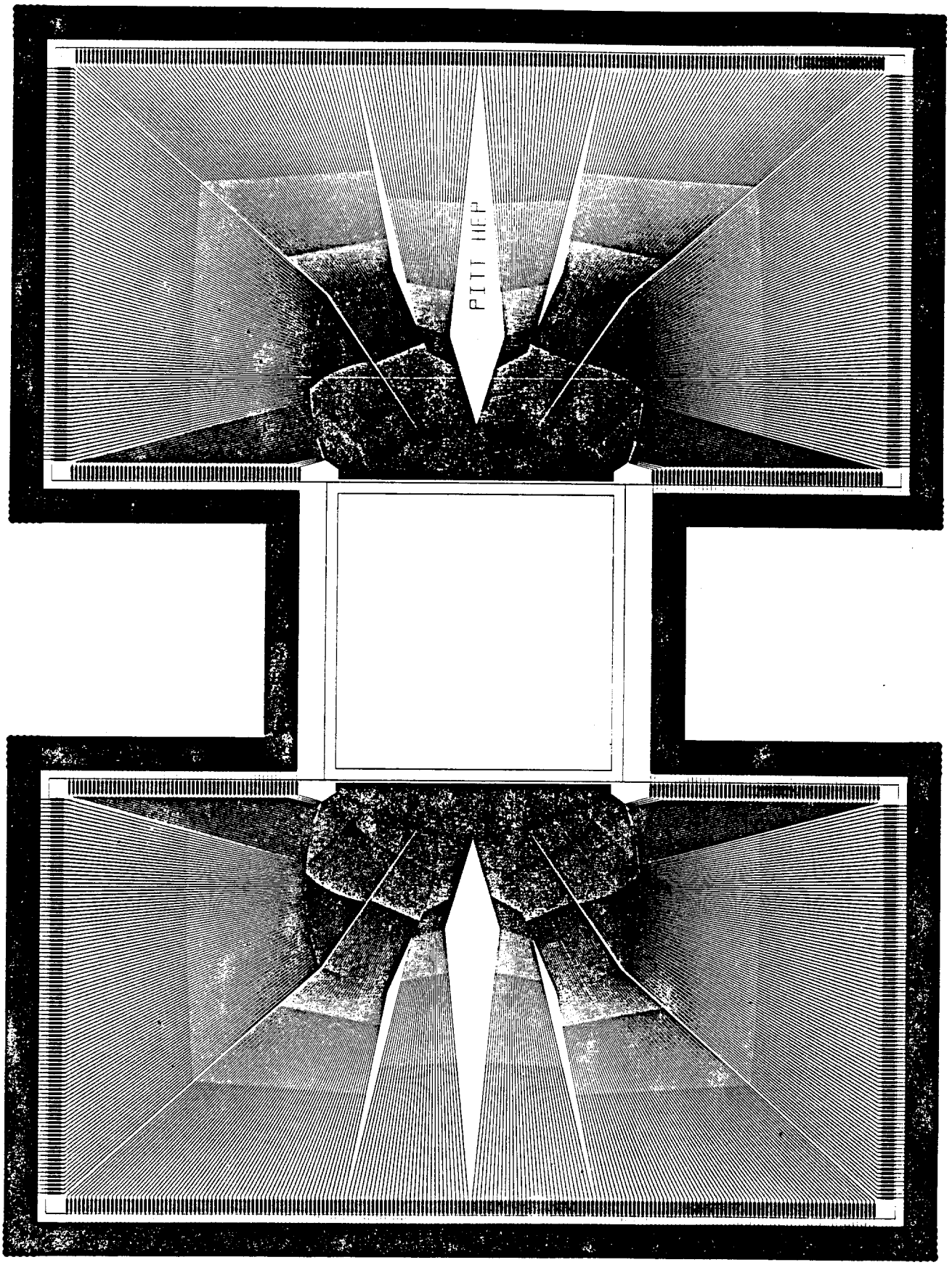

Figure B-2:

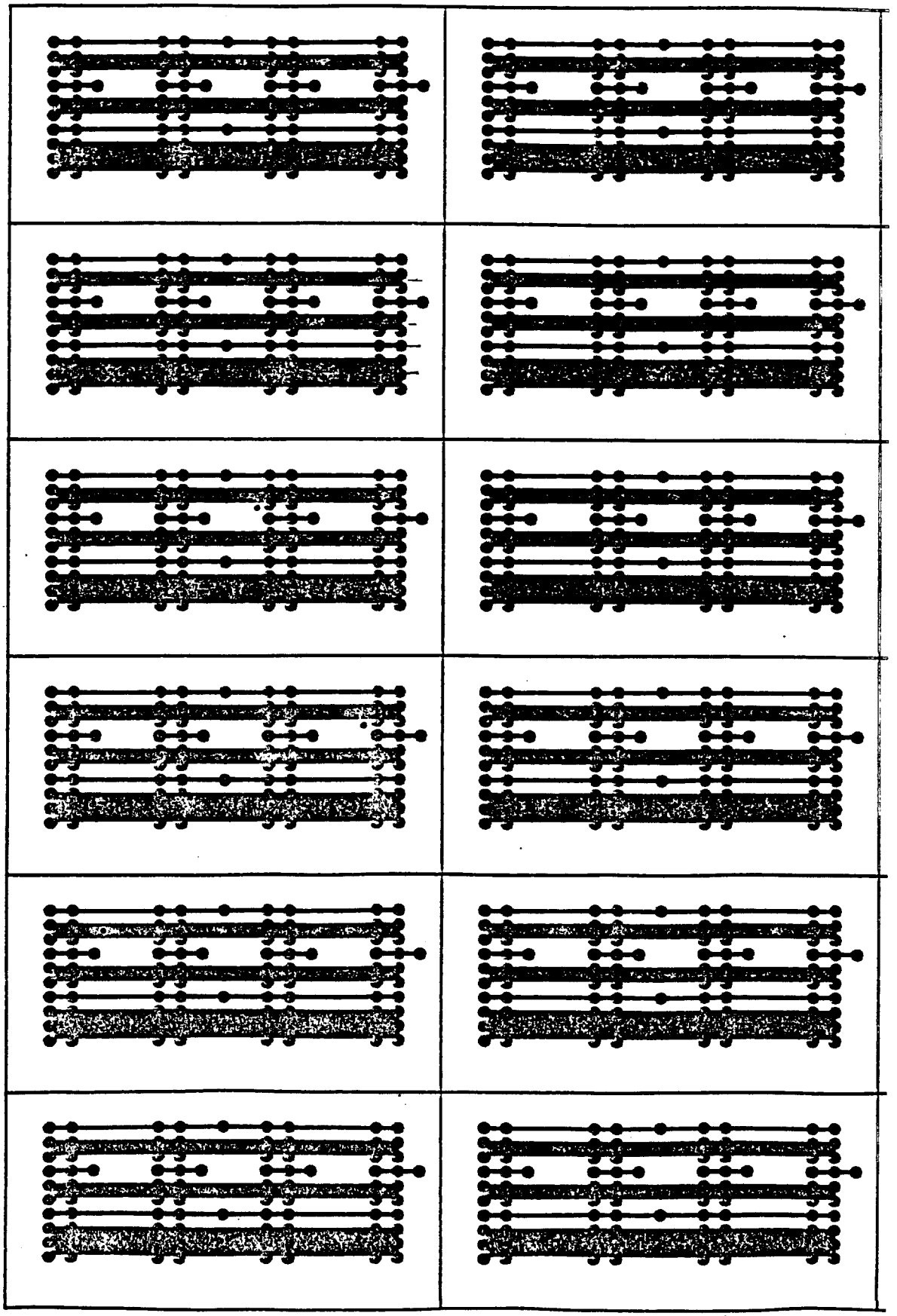

As far as programming is concerned the task that it has to accomplish is putting the commands on a tape that can be read into the computer operating the photoplotter. This is rather simple using software packages that can convert data from one format to another. We wrote FORTRAN programs that computed the required movements and wrote out the data in ASCII formats. A plotting package was used along with the program to obtain ink plots of the design that was being worked upon. In Figures B-1 and B-2 we show some examples of masks designed in this fashion. As can be seen, the mask in Figure B-2 has a large number of holes and hence requires precision drilling. A digitally controlled drilling machine is very similar to a photoplotter if we replace the light source with drill-bits and hence the commands used to run it have a similar format. This allowed for a simple change in program to accomplish this function as well.

References

1. C. Quigg, Gauge Theories of the Strong, Weak, and Electromagnetic Interactions, The Benjamin/Cummings Publishing Company, Inc., Reading, Ma., 1983.
2. NATO ASI Series, Techniques and Concepts of High-Energy Physics III, edited by T. Ferbel, Plenum Press, New York, 1984.
3. M. Gell-Mann and Y. Ne'eman, The Eightfold Way, Benjamin, New York, 1964.
4. Gross et al, Phys. Rev. Lett. 30, 1343 (1973).
5. Politzer, H.D., Phys. Rev. Lett. 30, 1346 (1973).
6. F.E. Close, An Introduction to Quarks and Partons, Academic Press, 1979.
7. E. Leader and E. Predazzi, An Introduction to Gauge Theories and the 'New Physics', Cambridge University Press, Cambridge, U.K., 1985, Chapter 12.
8. D.H. Perkins, Introduction to High Energy Physics, The Benjamin/Cummings Publishing Company, Inc., Reading, Ma., 1982, Chapter 7.
9. E. Leader and E. Predazzi, An Introduction to Gauge Theories and the 'New Physics', Cambridge University Press, Cambridge, U.K., 1985, Chapter 5, Section 2.
10. CERN experiments CDHS and CHARM, .
11. R.D. Field and R.P. Feynman, Nucl. Phys. B136, 1 (1978).
12. Andersson et al, Comp. Phys. Comm. 27, 243 (1982).
13. T. Ferbel and W.R. Molzon, Revs. of Mod. Phys. 56, 181 (1984).
14. Aurenche et al, Phys. Lett. 140B, 87 (1984).
15. J. Kemmer, NIM 169, 499 (1980).
16. C. Damerell, Rutherford Appleton Labratory, "Applications of Silicon Detectors in High Energy Physics and Astrophysics," .
17. Hyams et al, NIM 1983, 99 (1983).
18. Hughes Aircraft Co., Carlsbad, Ca. 92008.
19. Micron Semiconductor, Inc., Longwood, Florida 32750.

20. Cad Services, Inc., Townsend, Ma 01469.

21. Compunetics, Inc., Monroeville, Pa 15146.

22. Kepro Circuit Systems, Fenton, Mo. 63026.

23. Shulek et al, Soviet Jou. of Nuc. Phys. 4, 400 (1967).

24. Bailey et al, NIM 213, 201 (1983).

25. R.W. Harris and T.J. Ledwidge, **Introduction to Noise Analysis**, Pion Limited, London, 1984.

26. R.L. Stratonovich, Translated by R.A. Silverman, **Topics in the Theory of Random Noise**, Gordon and Breach, New York, 1963.

27. C.D. Motchenbacher and F.C. Fitchen, **Low Noise Electronic Design**, Wiley, New York, 1973.

28. R.d. Thorton, D. DeWitt, P.E. Gray and E.R. Chenette, **Charecteristics and Limitations of Transistors**, Wiley, New York, 1967, Chapter 5.

29. S.T. Hsu, Solid-State Electronics 13, 843 (1970).

30. R.d. Thorton, D. DeWitt, P.E. Gray and E.R. Chenette, **Charecteristics and Limitations of Transistors**, Wiley, New York, 1967, pp 152-153.

31. R.d. Thorton, D. DeWitt, P.E. Gray and E.R. Chenette, **Charecteristics and Limitations of Transistors**, Wiley, New York, 1967, page 163.

32. V. Radeka, IEEE Trans. Nucl. Sci. NS-21, 51 (1974).

33. V. Radeka, IEEE Trans. Nucl. Sci. NS-15, 455 (1968).

34. Nanometrics Systems, Inc., Oak Park, Ill. 60302.

35. F.E.Paige and S.D.Protopopescu, BNL-31987.

36. F.E. Paige and S.D. Protopopescu, "ISAJET 5.02: A Monte Carlo event generator for pp and $\bar{p}p$ interactions," **Supercollider Physics**, World Scientific, 1986, pp. .

37. G.Altarelli and G. Parisi, Nucl. Phys. B126, 298 (1977).

38. T.D. Gottschalk, CALT-68-1241(1985).

39. Andersson et al, Comp. Phys. Comm. 28, 229 (1983).

40. Witherell et al, Fermilab E691.

41. Bellini et al, CERN NA1.

42. Reay et al, Fermilab E653.

43. CERN experiments NA11/32, .

44. Mueller et al, Phys. Lett. 157B, 226 (1985).

45. F. Halzen, **The Status of Perturbative QCD,** edited by R.C. HWA, World Scientific, Singapore, 1986.

46. Engels et al, NIM A226, 59 (1984).

47. Engels et al, to be published in NIM.